2D Effects of Anisotropy on the Ductile Fracture of Titanium

By
Mishaal Azhar, B.A.Sc.

Submitted to the Faculty of Graduate and Postdoctoral Studies
In partial fulfillment of the M.A.Sc program in
Mechanical Engineering

Ottawa-Carleton Institute for
Mechanical and Aerospace Engineering

University of Ottawa

Mishaal Azhar
University of Ottawa

Master of Applied Science (Submitted in August 2013; defended in October 2013)

The Ottawa-Carleton Institute for Mechanical and Aerospace Engineering
Ottawa, Ontario

Title: 2D Effects of Anisotropy on the Ductile Fracture of Titanium

Author: Mishaal Azhar
Supervisor: Dr. Arnaud G. Weck

Number of pages: xvi + 156 = 172

Mishaal Azhar
University of Ottawa

Abstract

Titanium is a widely used metal in industrial and commercial applications. It retains anisotropic mechanical properties at room temperature due to its HCP crystal structure. The effects of crystal orientation have been studied theoretically and through modeling though there is a lack of empirical data available on the topic.

The work presented here uses laser-machined voids along with EBSD analysis to study the ductility of grains in different orientations to better understand the microscale fracture process in α-titanium.

Experimental results show that hard grains with their *c*-axis parallel to the tensile direction behave in a less ductile manner than grains with their *c*-axis oriented away from the tensile direction. This is due to the basal slip systems activating in the former case and prismatic slip systems in the latter. Models utilized include the McClintock model for void growth, Brown-Embury model for void coalescence and FEM crystal plasticity simulations

Acknowledgements

First and foremost I would like to thank my supervisor Dr. Arnaud Weck for his valuable advice and guidance throughout the course of this project. Without his involvement and invaluable suggestions this project would have not been as successful.

Dr. Mohammed Yandouzi provided EBSD analysis for all test specimens in this project, a key and critical step without which such research would not have been possible. I would like to thank Dr. Javier Segurado (Polytechnic University of Madrid) for his support regarding the finite element simulations and the use of his crystal plasticity subroutine.

I would also like to thank my colleagues Elisa Cantergiani, Marina Pushkareva, Yusha Lan, Yaser Alinaghian, Mahyar Asadi, Amirhossein Ketabchi, Stephen Knapp and Trevor Meunier in the Fracture Ottawa Group for their insightful advice and companionship.

Finally I would like to thank my family for their unwavering support through thick and thin.

Table of Contents

List of Figures

List of Tables

Chapter 1: Introduction

Titanium is one of the most widely used metals in the world today, particularly in the industry. Its excellent properties make it a valuable and useful material. Titanium has the best strength-to-weight ratio of all metals. Additionally it forms a very strong oxide layer that is extremely adept at preventing corrosion. Titanium alloys are commonly used in the high temperature regions of turbine engines (particularly in turbine blades) and airframes. It can also be used as condenser tubing liner in power generation due to the corrosive environment. Several chemical processing operations utilize titanium to increase equipment lifespan, providing a cost advantage over the use of other metals such as nickel or zirconium. The automotive and racing industries are seeing more parts being manufactured out of titanium due to its durability, lightweight and heat resistance. Due to its chemical inertness and propensity towards osseointegration, titanium is very regularly used in biological implants (e.g. dental, knee or hip implants). The golfing industry also commonly uses titanium in golf clubs due to its stiffness properties.

An interesting aspect of titanium is its inherent anisotropy, i.e. the directional dependence of its properties. This arises due to its crystal structure being hexagonal close packed (HCP), while most metals it has replaced are of the body centered cubic (BCC) or face centered cubic (FCC) crystal configurations. However the effect of this anisotropy on its mechanical and failure properties has not been studied extensively, with the bulk of research being in the modeling and simulation categories.

The reason for this is the relative difficulty in studying the fracture process of materials. Fracture is a process that occurs over a fraction of a second at typical strain rates and over very small deformations, making it difficult to suspend a test just prior to fracture. Additionally damage to a material begins within the bulk of the material, raising the question of how one would visualize this damage in order to study it.

Studying the effects of anisotropy requires one to utilize characterization techniques to determine the orientations of the different grains within the metal (such as electron backscatter diffraction, or EBSD). Preparation of materials for such analysis is typically an

arduous process, and even more so with titanium due to its sensitivity to plastic deformation (which would interfere with such characterization techniques).

The goal of this project is to procure experimental data on the effect of anisotropy on the fracture of titanium. This will be carried out by carrying out EBSD analysis on titanium tensile coupons. Using the grain orientation maps produced, microvoids will be machined on grains of various orientations on the surface of the coupons through the use of a femtosecond laser. The microvoids are designed to mimic the voids found in real materials that are a product of the fracture process. Surface strain maps of the tensile coupons will then be developed through digital image correlation (DIC). Analysis will include the morphological evolution of the voids and their growth rates. Finally, a crystal plasticity model will be used to simulate void growth in titanium.

With regards to the structure of this report, the next chapter will consist of a literature review containing information on relevant properties of titanium and any related research completed. Chapter 3 will detail the experimental, modeling and analysis procedures utilized. Chapter 4 showcases the results of the experiments, while the fifth chapter focuses on the finite element modeling. The sixth chapter will discuss the results with respect to the literature and assesses the validity of certain ductile fracture models. The seventh and final section will consist of concluding remarks and avenues for future research. The appendices contain supplementary pictures of void growth/coalescence across a number of tests.

Chapter 2: Literature Review

2.1 Titanium: Fracture and Mechanical Properties Characterization

Titanium has a number of very beneficial properties that lends itself to a lot of applications. The next subsection section will look at the general properties of titanium, followed by the analysis of its microstructure. The section will finish with an in-depth look at the fracture properties of titanium, and different methods used to study such properties.

2.1.1 Fundamental Properties

Some of the more basic properties of titanium are shown in Table 1 [1]. The same information is presented for iron and aluminum as a comparison. Titanium has a very high melting temperature making it suitable for more thermally intense applications. However above a temperature of 882°C its crystal structure shifts from hexagonal close-packed (HCP) to a body-centered cubic (BCC) system, bringing along with it a change in behavior. Pure titanium is considered to be an anisotropic ductile material, with the highest strength-to-weight ratio of all metals. Titanium is very reactive with air and upon atmospheric contact forms a very strong layer of TiO_2. This layer of TiO_2 is usually around 1 – 2 nm thick and provides corrosion resistance to most oxidizing acidic environments [2], one of the primary reasons for using the metal. Titanium's high reactivity with oxygen is one of the main reasons for its high price, since its processing requires an inert atmosphere.

Table 1: Basic properties for titanium, along with the same properties for iron and aluminum **[1]**

	Titanium	**Iron**	**Aluminum**
Melting temperature (^oC)	1670	1538	660
Transformation temperature (^oC)	882	912	N/A
Crystal structure at 25 ^oC	HCP	BCC	FCC
Young's Modulus at 25 ^oC (GPa)	115	215	72
Density (g/cm^3)	4.5	7.9	2.7
Corrosion resistance	Very high	Low	High
Reactivity with O_2	Very high	Low	High
Price	Very high	Low	Medium

As with most metals, titanium is not often used in applications as a pure metal. Instead it is more commonly used in the form of an alloy. Table 2 displays a few different titanium grades and alloys. It is very evident from the table that alloying additions have a very large effect on titanium properties.

Table 2: Various titanium grades and alloys; CP stands for commercially pure **[1]**

Grade/alloy	**O (%, max)**	**Fe (%, max)**	**Other additions (%)**	**Minimum yield stress (MPa)**
CP Ti (Grade 1)	0.18	0.20	N/A	170
CP Ti (Grade 2)	0.25	0.30	N/A	275
CP Ti (Grade 3)	0.35	0.30	N/A	380
CP Ti (Grade 4)	0.40	0.50	N/A	480
Ti - 5Al - 2.5Sn (Grade 6)	0.20	0.50	4.0 – 6.0 Al; 2.0 – 3.0 Sn	795
Ti - 0.2Pd (Grade 7)	0.25	0.30	0.12 – 0.25 Pd	275
Ti - 3Al - 2.5V (Grade 9)	0.15	0.25	2.5 – 3.5 Al; 2.0 – 3.0 V	485

2.1.2 Microstructural Evolution of Titanium

This subsection is concerned with discussing the evolution of titanium's microstructure under different conditions. Initially we will be concerned with analyzing the titanium phase diagram, which will then be followed by an analysis of grain growth and texture. Finally the effects of heat treatments on mechanical properties will be examined.

2.1.2.1 Phase Diagram Analysis

The titanium/aluminum phase diagram is shown in Figure 1. The two phases of titanium that we would be concerned with are the α-phase (HCP; the active phase at room temperature) and the β-phase (BCC), although the former is of more importance with regards to this project.

The α/β allotropic transition temperature for pure titanium is 882°C. As we heat up a pure titanium sample, the α-phase is present up until the transition temperature after which

titanium atoms have enough thermal energy to begin forming the β-phase. The β-phase nucleates at the grain boundaries between two adjacent grains with HCP structure (also called an α-α boundary) [3]. Over time the β-phase becomes the dominant phase (i.e. has a higher volume fraction) and eventually, will encompass the whole material.

One process used to measure the amounts of α- and β-phases present during transformations was developed by Kim and Park [4]. Since the β-phase is more electrically conductive than the α-phase, measuring the electrical resistivity across a sample of titanium would help in determining the amount of each phase present and subsequently various data such as the rate of transformation and the amount of time required for complete transformation.

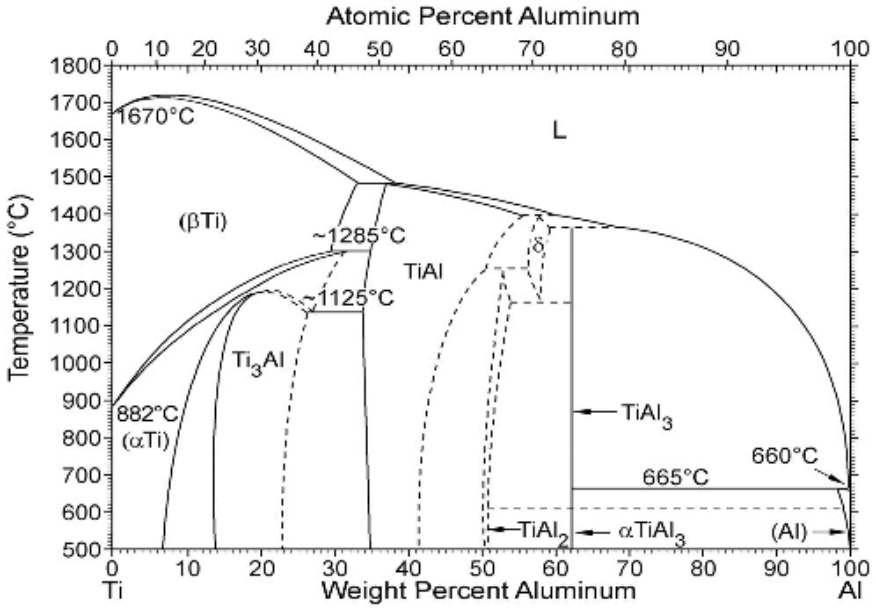

Figure 1: Phase diagram of titanium **[1]**

Alloying elements in titanium alloys are typically called α or β stabilizers depending on the effect they have on the α/β transition temperature [1]. Alloying elements such as aluminum, nitrogen or carbon are α-phase stabilizers; they increase the transition temperature making the α-phase stable over a larger range of temperatures. The oxide layer that forms on titanium is considered to be an α-stabilizer [5]. During oxidation, the oxide layer prevents the α-phase from transforming into the β-phase. Similarly, β-phase stabilizers like molybdenum, vanadium and niobium decrease the transition temperature.

2.1.2.2 Grain Growth and Texture Evolution

When a sample of titanium is provided with thermal energy, its atoms are provided with a driving force for grain growth. A larger increase in temperature means a larger driving force is applied leading to faster grain growth. Grain growth rates are more pronounced at the beginning of the process and exponentially decrease over time as the grain boundary surface area decreases (see Figure 2) [6]. Additionally, grain growth rates in the β-phase are at least ten times faster than in the α-phase [3].

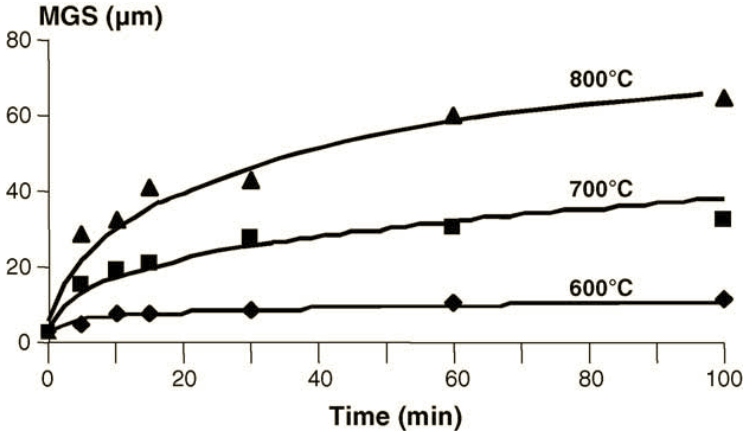

Figure 2: Mean grain size versus time for a cold-rolled sample of titanium at various annealing temperatures **[6]**

Changes in the evolution of microstructure are usually measured using Euler angles. Euler angles use three angle measurements to determine the amount of rotation a grain experiences with relative to two sets of axes: the rolling/normal/transverse directions of a cold-rolled sheet of titanium (*ABC*) and the unit cell axis (*XYZ*). Figure 3 shows a schematic of these two sets of axes.

Euler angles are measured using three coordinates which are representative of the magnitude of angular rotations required to align the unit cell axis (*XYZ*) with the rolling axis (*ABC*): $\{\phi_1, \Phi, \phi_2\}$ [7]. In order to determine the first angle ϕ_1 the unit cell needs to be rotated by an angle such that the *X*-axis is parallel to the plane *AB* (i.e. rotation around the *Z*-axis). The second angle Φ is the subsequent rotation of the unit cell around the *X*-axis such that the *Z*- and *C*-axes are aligned. The third and last angle ϕ_2 is determined by final rotation of the unit cell so that both sets of axes are aligned (i.e. another rotation around the *Z*-axis).

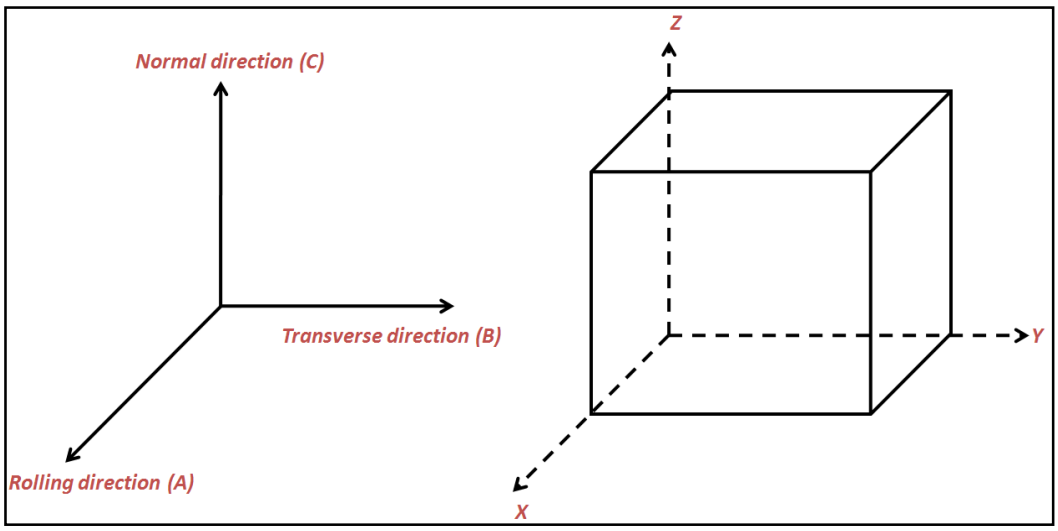

Figure 3: The two reference axis for determining Euler angles

A study conducted by Bozzolo *et al.* [6] noted that the majority of grain orientations post-recrystallization (conducted at 540°C for 24 minutes) had the Euler orientation of {0°, 35°, 0°}. After annealing at temperature ranges between 600°C to 800°C for a range of times, the orientations evolved to {0°, 35°, 35°} with the initial orientation becoming a minority due to orientation pinning. Throughout the heat treatment process the majority of grain orientations that disappeared had a grain boundary misorientation angle greater than 30°; these grains have fast moving grain boundaries leading to them being annihilated rather quickly.

With respect to pole figures there are two expected textures for rolled sheets of titanium in the [0002] and [10$\underline{1}$0] directions respectively [8]. This is shown in Figure 4 for a titanium sheet prior to annealing and in Figure 5 for a titanium sheet after annealing. These textures are typical of cold-rolled sheets of metal. Prior to annealing one can see the [10$\underline{1}$0] pole lies along the rolling direction. After annealing this pole rotates about 30° to the c-axis to bring about the new pole figure.

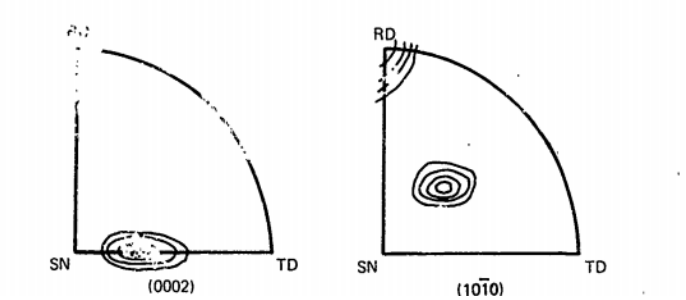

Figure 4: Pole figure of α-Ti rolled sheets in the [0002] and [10$\underline{1}$0] directions, prior to annealing **[8]**

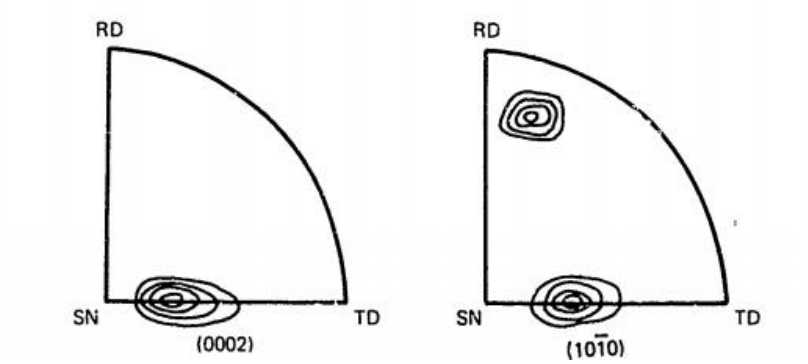

Figure 5: Pole figure of α-Ti rolled sheets in the [0002] and [10$\underline{1}$0] directions, after annealing **[8]**

2.1.2.3 Heat Treatment Effects on Mechanical Properties

The primary effect of heat treating titanium would be a change in its mechanical properties. The change in grain size would prominently factor into this and is governed by the Hall-Petch equation [9] [10]:

$$\sigma_y = \sigma_o + \frac{k_y}{\sqrt{d}} \qquad \text{Eq. \{1\}}$$

where σ_y is the yield strength of the material, σ_o is a material constant related to the stress required to move a dislocation, k_y is the material strengthening coefficient and d is the average grain diameter. The values of σ_o and k_y for titanium are 80 MPa and 0.40 MPa $m^{-1/2}$, respectively (these are average values taken from tests on polycrystalline titanium) [11]. As evidenced by this formula, we can see that as the mean grain size of a material increases, its yield strength decreases (illustrated in Figure 6 for titanium). What occurs is that a large grain size corresponds with a low grain boundary surface area. Since grain boundaries impede dislocation movement, a lower grain boundary surface area means dislocations can travel more easily within the lattice leading to a weaker, but more ductile material. Heat

treatments are generally utilized to obtain larger and uniform grain size distributions, leading to materials with lower yield strength values.

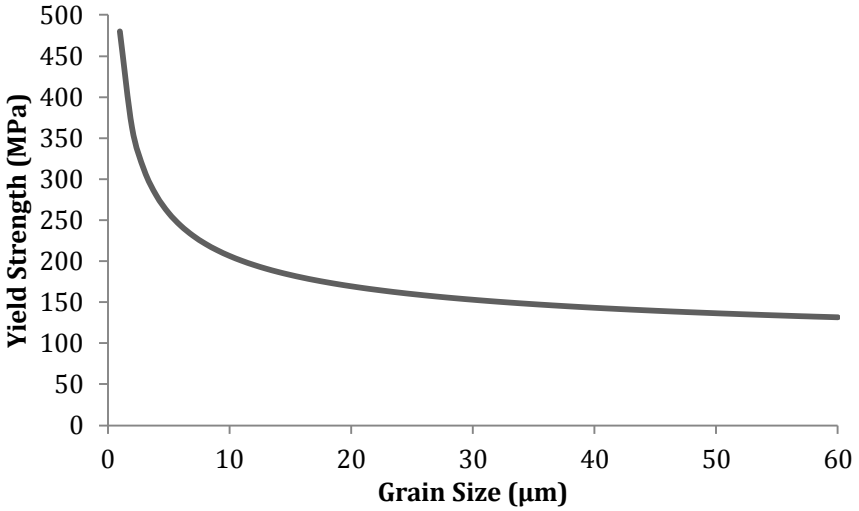

Figure 6: Yield strength trend as grain size increases for titanium, via the Hall-Petch equation

Since titanium is an anisotropic material, its yield strength varies depending on the direction of the tensile axis relative to the unit cell axis. The volume fraction of hard and soft grains in the material cross-section perpendicular to the tensile axis will be the main determining factor in this regard. This is primarily due to prismatic slip being easier to activate in soft grains (this is touched upon further in Chapter 2.1.3.3, page 17) [12].

A study looked at the effect of heat treatments on stress-strain behavior of titanium [13]. The research group took samples cut along the rolling and transverse directions (RD and TD respectively); heat treated them at 1000°C (past the α-β transformation temperature) for 30 minutes and quenched them in water. They conducted tensile tests on these samples and compared them to the stress-strain results retrieved from tests on as-received samples. The results in Figure 7 showed that TD samples were more ductile (lower ultimate tensile strength, but larger failure strain) prior to the heat treatment compared to RD, yet more brittle after the heat treatment.

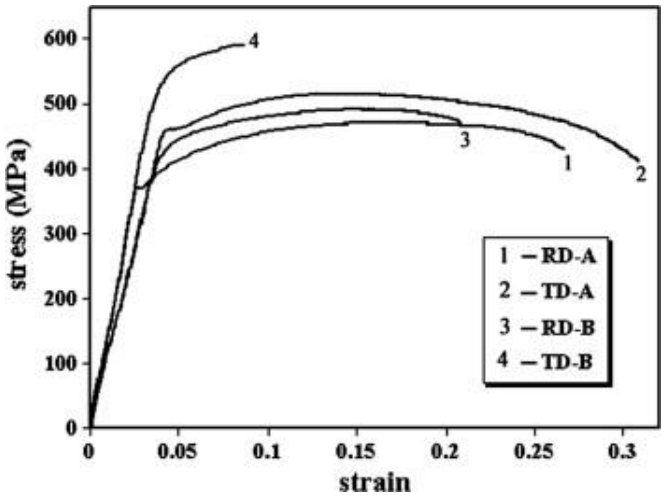

Figure 7: Stress-strain data for RD and TD samples tested as received (batch A) and after a heat treatment of 1000°C (batch B) for 30 minutes **[13]**

2.1.3 Deformation and Fracture of Titanium

This section will focus on the microstructural processes that activate during the deformation and fracture of titanium. First the reasoning and methodology behind ductile and brittle fracture in HCP materials is put forth, followed by how these processes occur in titanium.

2.1.3.1 Ductile Behavior versus Brittle Behavior

There is a large number of ways in which materials can fracture, with ductile and brittle fracture inhabiting the polar opposite ends of this spectrum. Ductile fracture is caused by the occurrence of plastic deformation within the material [14]. By applying stresses onto a material, dislocations propagate through the crystal lattice and build up at various lattice imperfections (such as grain boundaries or interstitial impurities). This dislocation pile-up will cause local lattice decohesion, which in turn leads to micro-void nucleation (the first stage of plastic deformation). As stress application continues, the voids grow in size (the second stage of plastic deformation). Once voids are large enough to interact and coalesce with each other we see the final stage of plastic deformation occur. This last stage leads to the fracture of the material. The whole process is illustrated in Figure 8. Ductile fracture is a diffusion-based process since it requires the movement of atoms and voids (also making it a temperature based process) [14]. Additionally since grain boundaries are usually the most common lattice imperfection, voids nucleate, grow and coalesce mostly at these locations. Macroscopically this is evident via the presence of intergranular fracture.

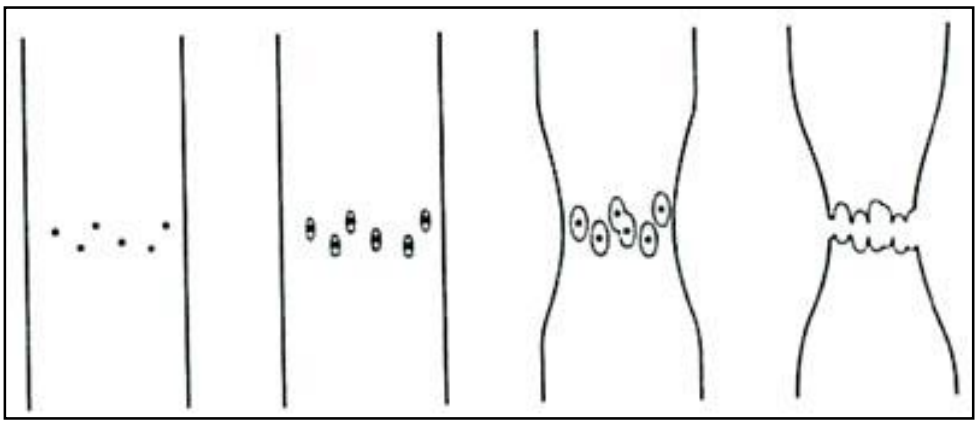

Figure 8: Schematic of ductile fracture occurring, beginning with (from left to right) void nucleation, followed by void growth, coalescence and finally fracture **[15]**

Brittle fracture occurs through cleavage [16]. Cleavage is the tendency for a crystal to split along specific crystallographic planes and primarily occurs to keep two surfaces electrically neutral [17]. Assuming a hypothetical and homogeneous material, all bonds between atoms would have the same strength causing cleavage to occur between planes that are connected by the fewest bonds. If a material were not homogeneous then there would be some atoms in the crystal lattice that would exhibit weaker bonding properties. In this case cleavage would occur across planes where these atoms are located. By studying the cleavage patterns in a material it is possible to determine certain information such as crystal structure and orientation. A schematic showcasing three types of cleavage is shown in [18].

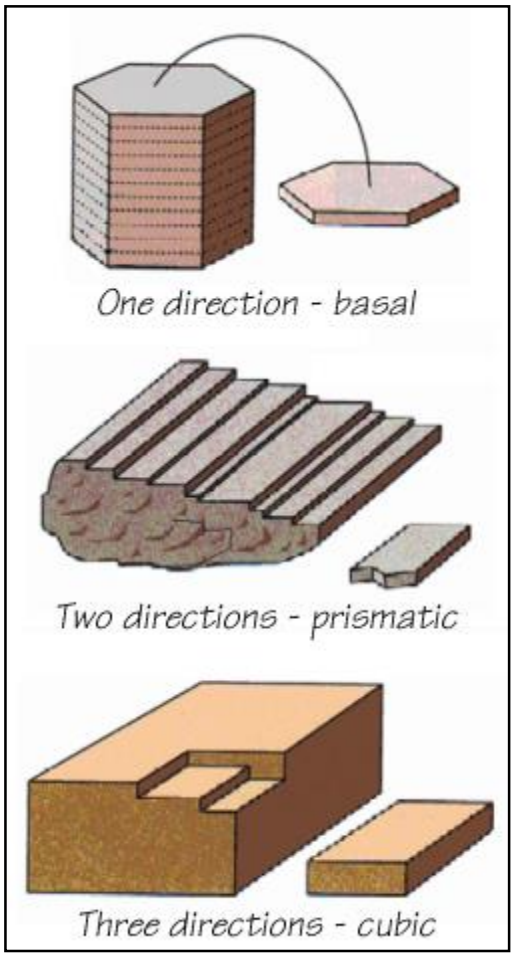

Figure 9: A schematic of three types of cleavage mechanisms **[17]**

An interesting microscopic effect in materials is twinning, since there is a lot of debate as to whether it promotes plastic flow [19] or brittle cleavage [16]. If the atoms in a material do not have enough energy to allow for dislocation movement via slip, externally applied stresses may sometimes cause atoms to displace via a shear of lattice points called deformation twinning

(see Figure 10) [20]. The presence of twinning enables a crystal to witness a plastic change of shape with a miniscule change in volume [21]. It is evident under a microscope via the presence of thin, dark and straight bands within grains (see Figure 11). The volume fraction of twins in a material tends to grow as the applied strain increases and temperature decreases [22]. Additionally compression forces produce a lower volume fraction of twins [23] than tensile forces, which promote a higher volume fraction of deformation twinning within the material [24]. Finally, increasing concentrations of solute atoms will work to suppress the occurrence of twinning [16].

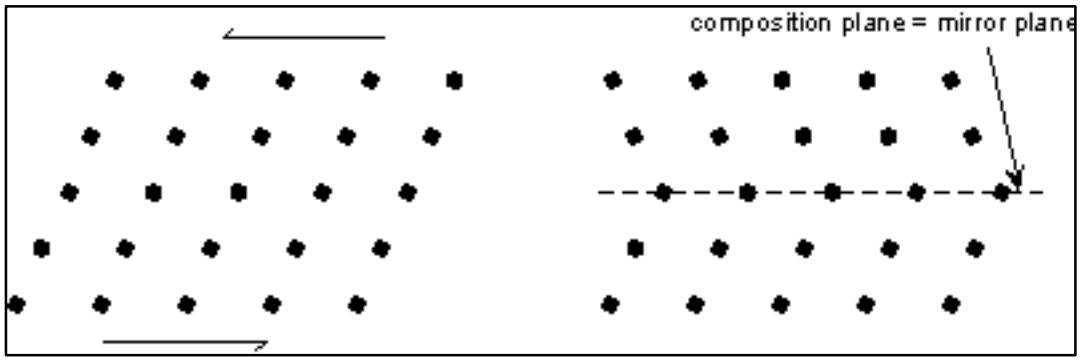

Figure 10: Schematic of a material being stressed with a shear force (left) causing it to twin and form a mirror plane (right) **[25]**

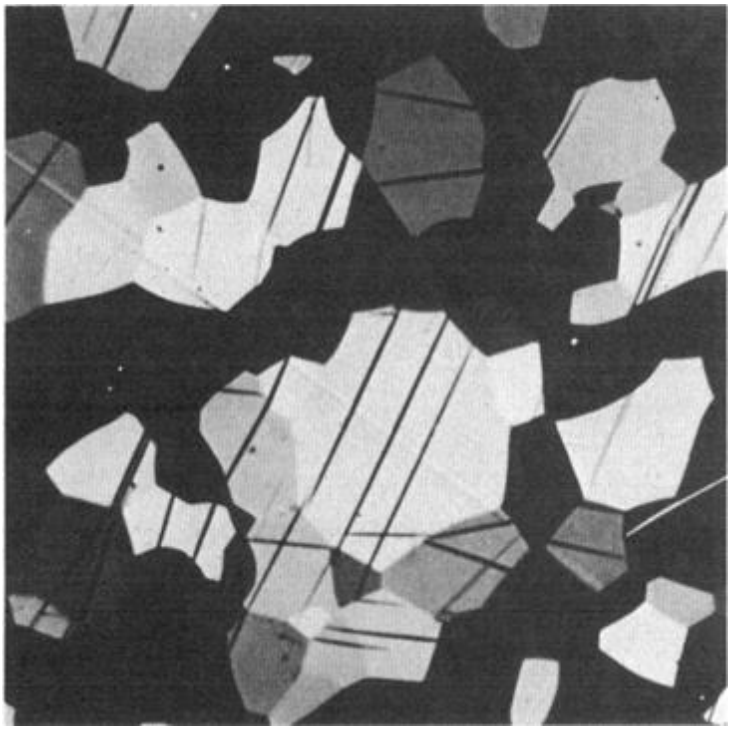

Figure 11: Twinning in titanium at a strain of 2%, showcased by the thin dark bands within the grains **[24]**

2.1.3.2 Ductile and Brittle Behavior in HCP Metals

It is interesting to note that different materials with the same crystal structure can exhibit different types of fracture behavior. For example both titanium and zinc retain the HCP structure at room temperature, however the former is ductile while the latter is brittle [19]. Plastic deformation is a result of dislocation movement, which in turn is caused by atomic diffusion.. It would follow that ductility is temperature dependent via the activation energy for atomic diffusion. This is clearly evident in Figure 12, which details the evolution of different fracture mechanisms in titanium as temperature changes. Since pure titanium is a ductile material, cleavage (brittle fracture) only occurs at very low temperatures, with ductile fracture and creep (a diffusion based process that could be categorized as a ductile event) kicking in at higher temperatures.

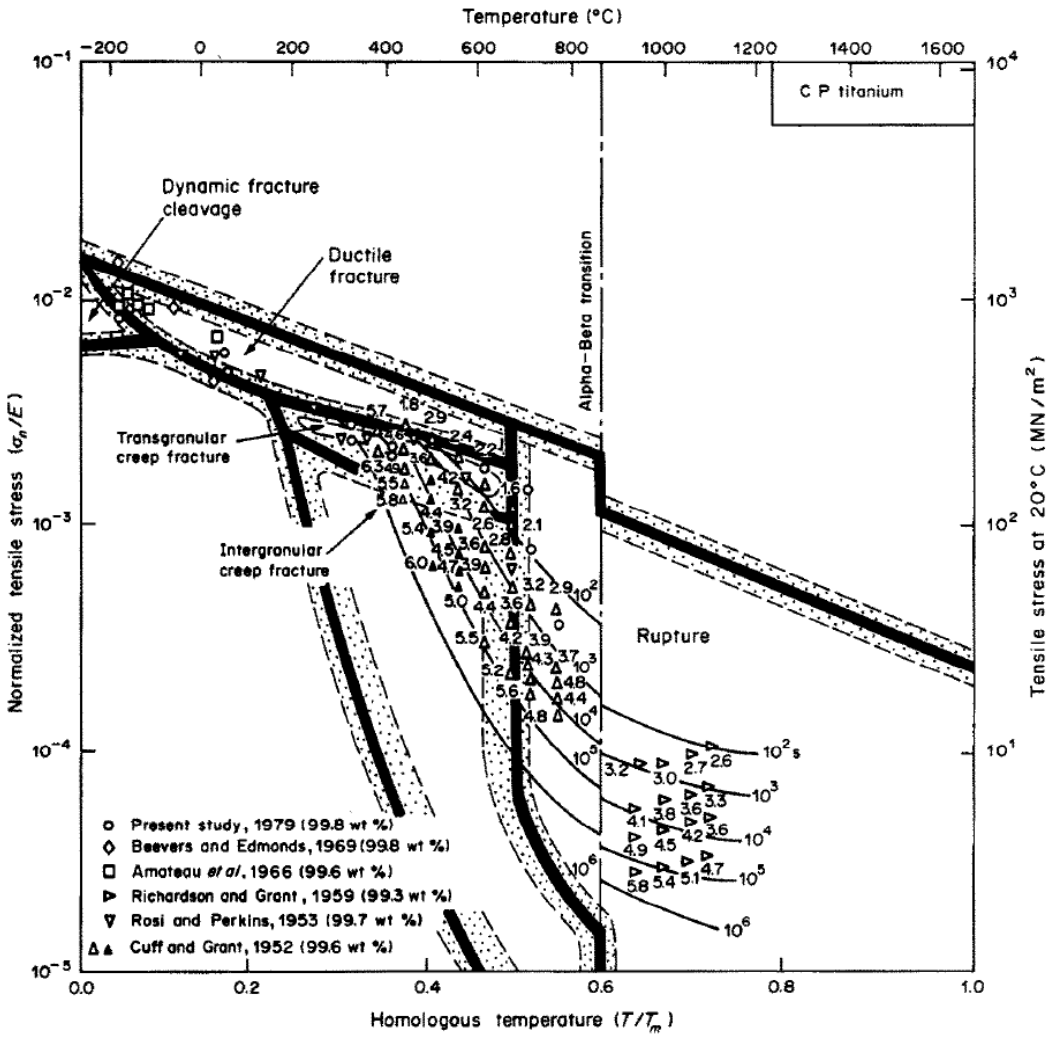

Figure 12: Fracture mechanism map for pure titanium, showing the evolution of fracture processes with changes in temperature **[26]**

However what causes certain HCP metals to be brittle (such as zinc or beryllium) while others are ductile (titanium or zirconium)? One such way of determining this was proposed by Pugh [27], who analyzed the ratio between a material's elastic bulk modulus K and its shear modulus G. K is a measure of a material's response to uniform pressure, while G describes a material's response to shearing strains. The equation Pugh put forth was:

$$Pugh\ criterion = \frac{K}{G} \qquad \text{Eq. } \{2\}$$

If this ratio were high for a material, then it would be ductile. If the value of Equation 2 was low then the material will be brittle. It could be said that the ratio analyzes the limiting factor

when applying stresses to a material, so a high ratio would mean that the value of *G* is much lower than the value of *K*. This means that the material would respond to shear strains much earlier than it would to bulk strains, allowing dislocation movement and twinning to occur.

A second ductile-brittle behavior study was conducted by Rice and Thomson [28]. They put forth the following equation:

$$Rice - Thomson\ criterion = \frac{G \times a}{\Gamma_{sv}} \qquad \text{Eq. \{3\}}$$

Where *G* is the shear modulus, *a* is the material's lattice constant and Γ_{sv} is surface energy. It was proposed that ductile materials would have a low value of the parameter in Equation 3 (less than 7.50 – 10) along with a wide core of dislocations, while the opposite would be said for brittle materials. The dislocation core is the area surrounding the center of the dislocation where the linear elastic relation (Hooke's Law) breaks down, allowing for plastic deformation [29].

Table 3 displays the values retrieved using Equations 2 and 3 for various HCP metals, along with experimental analysis of ductile behavior. It is evident from this data that the Pugh and Rice-Thomson criteria do not provide perfect results, but they both do correctly rank zirconium and titanium as the most ductile HCP materials and beryllium as the most brittle HCP material. It should also be noted that the Pugh criterion seems to be more accurate than the Rice-Thomson criterion in predicting ductility, even if it is not perfect.

Combining the two criteria seems to be a rather functional method to determine ductility. Figure 13 plots the Rice-Thomson criterion against the Pugh criterion using the data in Table 3. It is evident from this graph that brittle and ductile HCP materials inhabit the top-left and bottom-right areas of the plot, respectively. The materials with intermediate ductility spill over into both these regions following no apparent pattern.

Table 3: Various metals and their measure of ductility according to Equation 2, Equation 3 and experimental results, from left to right respectively (ordered according to decreasing Pugh criterion values) **[19]**

Metal	$\frac{K}{G}$	$\frac{G \times a}{\Gamma_{sv}}$	**Ductility**

Zirconium	2.65	6.90	Good
Titanium	2.47	7.31	Good
Cobalt	2.31	9.27	Fair
Cadmium	2.21	10.24	Fair
Rhenium	2.05	15.73	Fair
Magnesium	2.03	8.10	Fair
Hafnium	1.95	9.16	Good
Zinc	1.73	11.73	Poor
Yttrium	1.63	11.59	Fair
Ruthenium	1.63	19.45	Poor
Beryllium	0.74	26.12	Poor

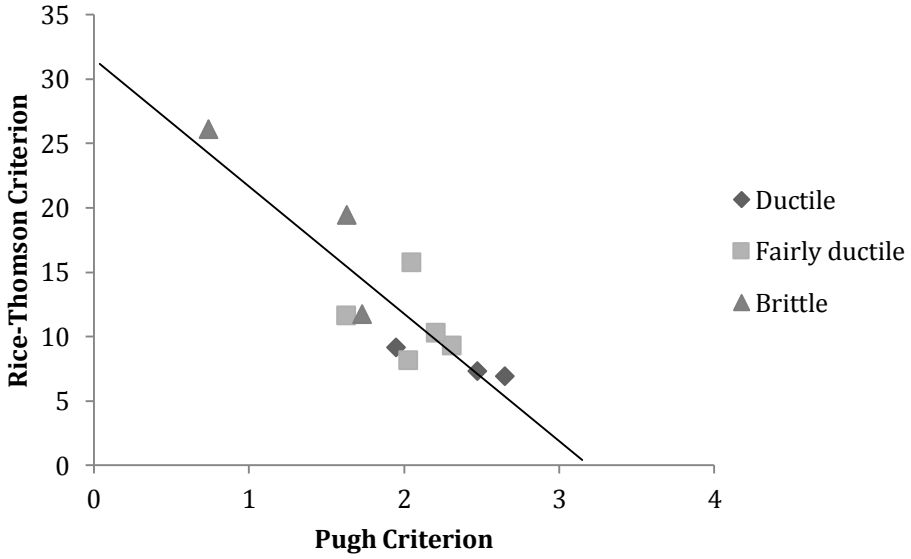

Figure 13: Graph showcasing the Rice-Thomson and Pugh criteria for the materials shown in Table 3, with a trendline through the data points, adapted from **[19]**

One study [30] noted that externally applied stresses might cause the misorientation between grains to increase or decrease. Additionally dislocation arrays or clusters can link together to form a dense dislocation wall which - given enough energy – can form a low angle grain boundary. These low angle boundaries can interact with neighboring high angle

boundaries to cause a change in orientation between grains. This continues on as a domino effect.

2.1.3.3 Slip Directions & Planes in Titanium

Table 4: Slip systems in a HCP crystal **[1]**

Slip system type	**Burgers vector type**	**Slip direction**	**Slip plane**	**Number of slip systems**	
				Total	**Independent**
1	**a**	<11$\underline{2}$0>	(0002)	3	2
2	**a**	<11$\underline{2}$0>	{10$\underline{1}$0}	3	2
3	**a**	<11$\underline{2}$0>	{10$\underline{1}$1}	6	4
4	**c + a**	<11$\underline{2}$3>	{11$\underline{2}$2}	6	5

Slip systems are defined as the directions and planes within a crystal lattice in which a dislocation is most likely to move along. Dislocations usually travel on planes with the highest planar density within the structure (e.g. the {111} family of planes in a FCC crystal), and in directions with the highest linear density (e.g. the <110> family of directions in a FCC crystal). The inter-planar and inter-atomic spacings are lowest in these directions; hence atoms and dislocations require less energy to jump between lattice points. The slip systems for an HCP crystal system (and by extension titanium) are given in Table 4 and are illustrated in Figure 14.

Both Von Mises [31] and Taylor [32] put forth the idea that a polycrystalline material needs at least five independent slip systems in order to undergo plastic deformation without producing cracks. The most common slip systems in an HCP material are types 1, 2 and 3 (respectively basal, prismatic and pyramidal slip; of which prismatic is the most common) This makes a total of 12 slip systems in titanium. This value can be reduced to an 8 since some of the systems are dependent on each other. This value can be further reduced to 4 since the combined actions of slip types 1 and 2 result in slip system 3. This goes against the ideas that Von Mises and Taylor put forth.

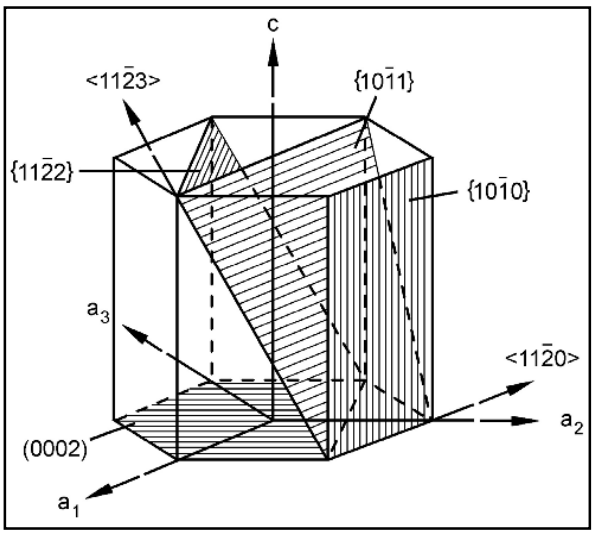

Figure 14: Illustration of the various slip systems in a HCP crystal **[1]**

There are two proposed ways in which this could be resolved. One such way is through a cross-slip system that has a prismatic system has the burgers vector **c** and a pyramidal system with vector **a** [33]. This would have the burgers vector **c+a** (slip system type 4 in Table 4), which has been observed via transmission electron microscopy (TEM) imaging in titanium [1].

The other possible method in which the Von Mises criterion can be satisfied was proposed by Kocks and Westlake [34]. They argued that HCP crystals need only 4 independent slip systems since the internal stresses at grain boundaries during deformation may be relieved by localized twinning. This idea is discussed more in the next section.

2.1.3.4 Deformation Twinning in Titanium

There are three twin modes that occur in titanium, which are detailed in Table 5. While twins in HCP materials are generally debated as to whether they promote ductile or brittle behavior, in titanium they are known to contribute to plastic deformation [1]. The type of twin produced is highly dependent on the direction of applied stress and the initial texture of the material. If a tensile stress were applied perpendicular to the [0001] direction in a grain then a compression twin would form either on the {10$\underline{1}$2} plane or the {11$\underline{2}$2} plane (example shown in Figure 15). The former is the most frequently observed twin system with the magnitude of its twin shear is lowest (it can even be said that it is the most common twin system due to this property [1]). If tension is applied parallel to the [0001] axis then a tension

twin forms on the {11$\underline{2}$1} plane (shown in Figure 16). This tension twin produces the largest twin deformation possible in a titanium grain.

Table 5: Twinning elements in HCP titanium **[1] [19]**

Twinning type	Compression	Compression	Tension
Twinning plane [1st undeformed plane] (K_1)	{10$\underline{1}$2}	{11$\underline{2}$2}	{11$\underline{2}$1}
Twinning shear direction (η_1)	<10$\underline{1}$1>	<11$\underline{2}$3>	<11$\underline{2}$6>
Second undeformed plane (K_2)	{$\underline{1}$012}	{11$\underline{2}$4}	(0002)
Direction of intersection of plane of shear with K_2 (η_2)	<10$\underline{1}$1>	<22$\underline{4}$3>	<11$\underline{2}$0>
Plane of shear perpendicular to K_1 and K_2	{1$\underline{2}$10}	{$\underline{1}$100}	{$\underline{1}$100}
Magnitude of twinning shear	0.167	0.225	0.638

Twins may also nucleate via slip transfer propagated through a grain boundary [12]. A soft grain is defined as a grain that has its c-axis perpendicular to the tensile stress direction (similar to the requirements for a compression twin to form). A hard grain is defined as a grain with its c-axis parallel to the tensile stress application (similar to the requirement for tension twins to form). If a soft and a hard grain were to be located adjacent to each other (effectively forming a pair), it was witnessed that prismatic slip in the soft grain may cause a {10$\underline{1}$2} twin to form in the neighboring hard grain. Depending on the texture of the sample, slip-activated twin nucleation may account for as much as a third of all twins that form within the sample.

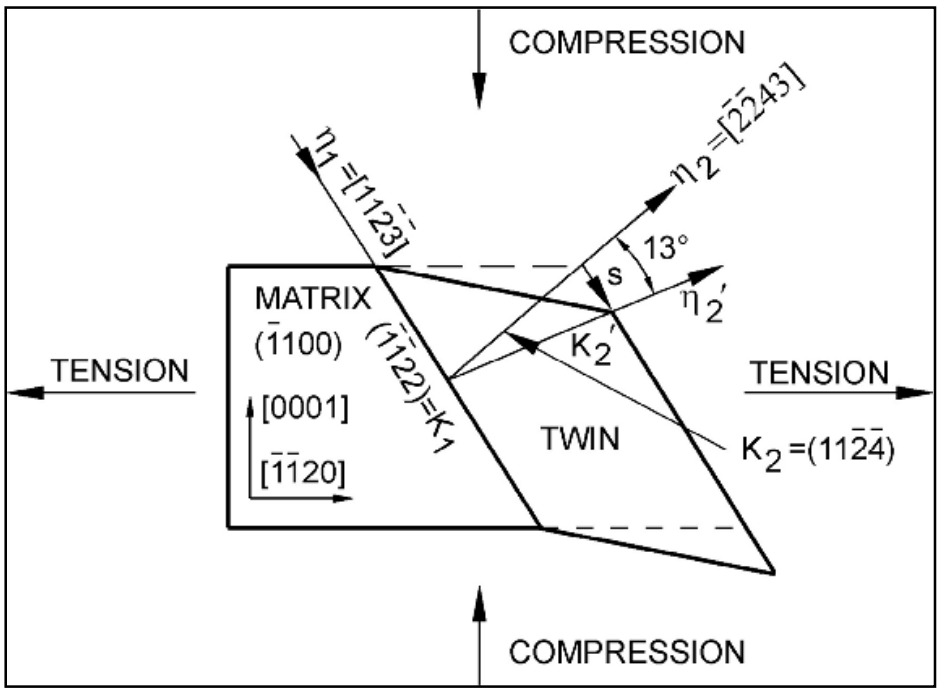

Figure 15: Illustration of a compression twin shape change by {11$\underline{2}$2} **[1]**

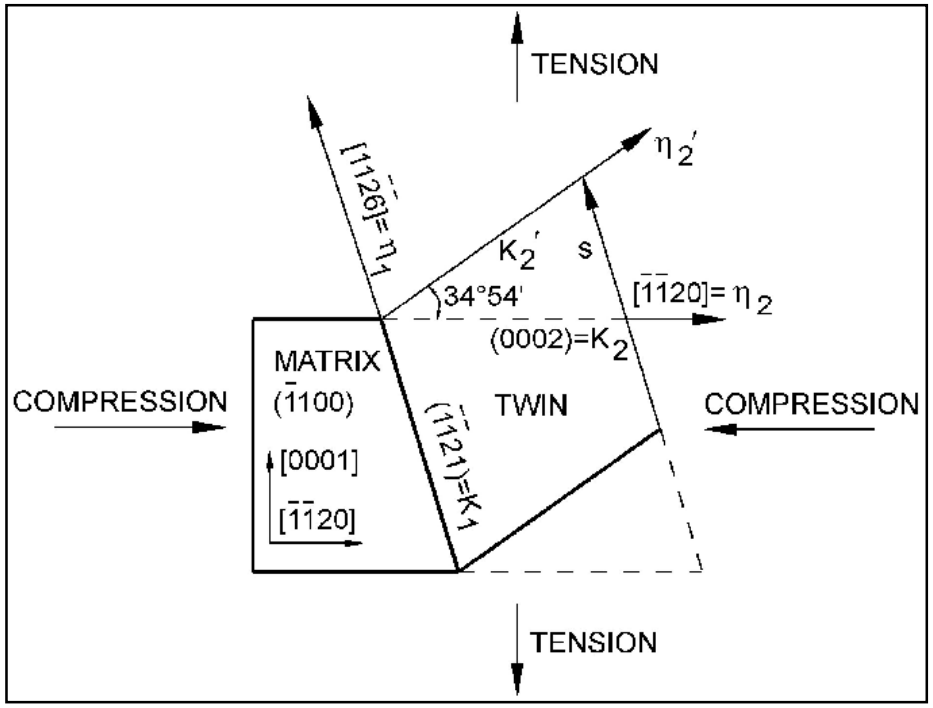

Figure 16: Illustration of a tension twin shape change by {11$\underline{2}$1} **[1]**

An interesting point to note is that, since the orientation of the grain and type of stress applied onto a lattice are rather important in determining the type of twin, grains oriented in the same direction will produce the same types of twins. This is evident in Figure 11 (page

12), where the grains with the same orientation (i.e. the grains with the same shade of grey) contain twins that are almost parallel to each other. Hence via the analysis of twins in optical and electron micrographs, it would be possible to determine the crystal characteristics of a lattice.

Once twins have nucleated in titanium, they tend to extend across a whole grain, have a flat-sided characteristic and do not grow appreciably in thickness as stress application continues [24]. Additionally it was determined that heavy twin formation at high strains is evidence of a constant work hardening rate. However this is not always the case as twinning may lead to a lattice that is oriented either more or less favorably for slip, leading to work softening or hardening respectively (although the latter case is more probable) [24]. In a smaller scale it was observed that stacking faults were observed within twins in cylindrical titanium rods tested in compression [23].

An interesting study of note was conducted by Meyers *et al.* [35] that attempted to develop models to predict the critical stress for twinning as a function of various parameters (temperature, strain rate and stacking fault energy). The model that they derived stated that the activation stress for twinning is:

$$\sigma_T = K\dot{\varepsilon}^{(m+1)^{-1}}\left(e^{\frac{Q}{(m+1)RT}}\right) \quad \text{Eq. \{4\}}$$

where σ_T is the twinning stress, $\dot{\varepsilon}$ is the strain rate, m is a constant, Q is the activation energy, R is the gas constant and T is the temperature. Note that this equation follows the Arrhenius equation structure. K is given by the following formula:

$$K = M_T\left(\frac{nlE}{MA_o}\right)^{1/m+1} \quad \text{Eq. \{5\}}$$

where M_T is the orientation factor (essentially the Schmidt factor equivalent for twins), n is the number of dislocations at the pile-up zone, l is the mean distance that dislocations travel from source to barrier, E is the elastic modulus of the material and A_0 is a constant.

A recent study on titanium looked at the effect of grain size on deformation twinning [36]. An inverse sensitivity between the two was found, meaning larger grains had a lower propensity to exhibit twinning. It was suggested that this is due to larger grains having larger internal volume allowing for easier dislocation movement.

2.1.3.5 Stress and Strain Dependent Properties

Plane-strain and plane-stress are two types of stress states that can develop in materials. Plane-strain defines a state where strain is applied onto a material in 2 directions, and is 0 in the third direction. This is commonly seen in materials where one dimension of the structure is much larger than the other two dimensions. The strains in this direction will be constrained by the surrounding material making it zero, or small enough to be negligible. The strain tensor of a sample under plane-strain is:

$$\varepsilon = \begin{bmatrix} \varepsilon_{11} & \varepsilon_{12} & 0 \\ \varepsilon_{21} & \varepsilon_{22} & 0 \\ 0 & 0 & 0 \end{bmatrix} \quad \text{Eq. \{6\}}$$

The stress tensor of a sample in plane-strain has the respective stress elements to the ones above with the addition of the stress acting in the 3rd dimension (σ_{33}), making the stress state triaxial.

Plane-stress is usually seen in samples where one of the dimensions is much smaller than the other two dimensions (e.g. thin foils). Stresses in the small dimension will not be able to develop and will be miniscule compared to the stresses acting within the plane. The stress tensor for a sample in plane-stress is:

$$\sigma = \begin{bmatrix} \sigma_{11} & \sigma_{12} & 0 \\ \sigma_{21} & \sigma_{22} & 0 \\ 0 & 0 & 0 \end{bmatrix} \quad \text{Eq. \{7\}}$$

The corresponding strain tensor would have the additional ε_{33} term.

It was found in a study that increasing the thickness of a titanium specimen increases the dominance of plane-strain over plane-stress, but also decreases the energy release rate [37]. The fracture process occurs at the lowest value of the critical energy release rate [38],

meaning thicker samples will see the 3-stage fracture process beginning earlier. This indicates that samples loaded in plane-stress will retain a better overall ductility [39].

However energy release rates are also determined by the direction the tensile test is conducted in, for rolled sheets of titanium [37]. High energy release rates were observed in thin samples tested along the rolling direction (RD), and thick samples tested along the transverse direction (TD). The fracture surface of such samples displayed elongated dimples. Low energy release rates were exhibited in thick RD tensile specimens and thin TD specimens, along with more equiaxed dimples on the fracture surface. Crack initiation and propagation energy for titanium samples are shown in Figure 17. The dip in the TD curve in Figure 17(a) was not explained.

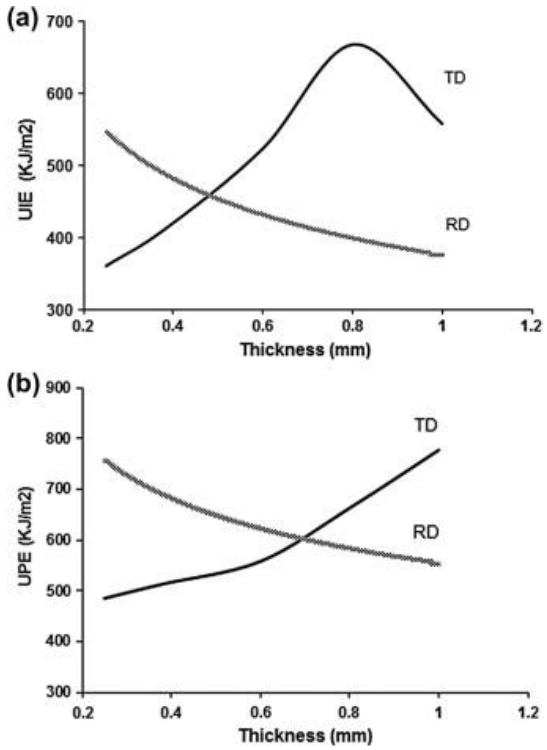

Figure 17: Crack initiation energy (a) and crack propagation energy (b) versus titanium tensile coupon thickness for samples cut along the rolling (RD) and transverse (TD) directions **[37]**

For the samples tested along the rolling direction, deformation was accommodated by the easier prismatic slip, i.e. these slip systems have a low critically resolved shear stress (CRSS) or activation energy at room temperature. The TD samples deformed through the more difficult basal and pyramidal slip systems (i.e. they have higher CRSS values than prismatic

slip systems at room temperature) [40]. The fewer active slip systems a specimen has, the higher its hydrostatic means stress and triaxiality at the crack tip.

2.1.4 Mechanical Properties Characterization Methods

This section will look at different ways one can study the mechanical properties of a material. There are three methods pertinent to this research project: tensile tests, compression tests and indentation tests.

2.1.4.1 Tensile Tests

Possibly the most common type of test conducted to study mechanical properties. A sample of the material to be tested (cut in the shape of a "dog bone") is loaded uniaxially in tension. A load cell takes note of the load required to deform the sample incrementally, which is (typically) correlated and plotted against the displacement of grips. The stress and strain data can be calculated from this information in order to retrieve a stress-strain curve.

The advantage of the stress-strain curve is being able to obtain a number of properties of the material, including ultimate tensile strength, maximum elongation (or failure strain), Young's modulus, Poisson's ratio, yield strength and strain-hardening characteristics. However these properties typically hold for macroscale analysis, and not for microstructural material behavior. An example of stress-strain data for titanium can be found in Figure 7 (page 10).

2.1.4.2 Compression Tests

Compression tests involve taking a bar of the material to be studied and loading compressive forces on it. It studies the response of material to crushing loads. The compressive stress-strain data can provide one with the elastic limit, yield point, yield strength and compressive strength of the material. Compression tests are generally perceived as more appropriate than tensile tests with regards to brittle or low-ductility materials.

Some materials behave differently under compression and tension. As mentioned previously, titanium is more susceptible to deformation twinning under tensile loads than compressive loads [22].

2.1.4.3 Indentation Hardness

The indentation hardness test measures a materials resistance to deformation. The test is conducted by forming an indent on the surface of the specimen with a variable load. Different types of indenters can be used, though the most common test is the Vickers hardness test. The Vickers hardness test is done with an indenter of an angle 22^{o} with the horizontal, typically made of diamond.

An issue that may crop up when measuring the hardness of a specimen is locating an ideal spot for indentation. Indents placed too close to each other or on microstructure artifacts (like grain boundaries or second phase particles) will provide false readings. Additionally samples tested for hardness need to be very well polished for good results. This should be done with care since grinding and polishing procedures can introduce a surface layer of plastic deformation that may look like polished material, but in reality will skew results. An example of the hardness value of thin foil titanium is shown in Figure 18, with respect to grain size.

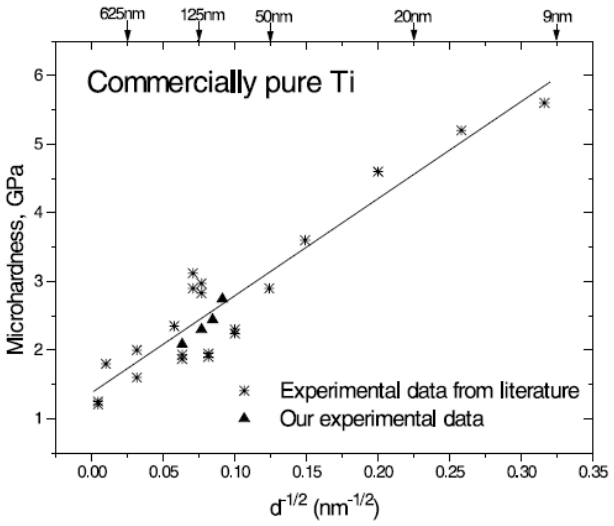

Figure 18: Microhardness values for thin-foil titanium with respect to grain size

Some studies have been conducted on the effects of grain orientation on the hardness of that grain. Britton *et al.* [41] carried out nanoindentation arrays on samples then conducted EBSD on the area of analysis to get the orientations of the grains within. By plotting the hardness values against the declination angle (angle between the grain's *c*-axis and the loading axis) a trend was seen, as shown in Figure 19.

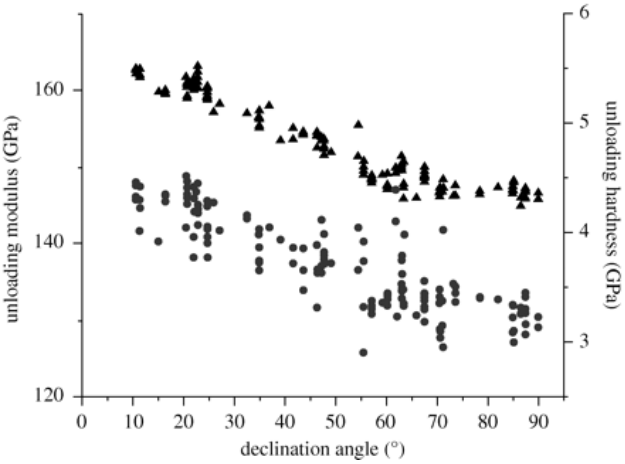

Figure 19: Hardness versus declination angle for various crystal orientations in titanium **[41]**

A declination angle of 0° means that the indentation is done on the basal plane (*c*-axis parallel to the loading direction). A declination angle of 90° means that the indentation is done on the prismatic plane (*c*-axis perpendicular to loading direction). The hardness values are highest in the former case. The reason for this is better explained in a paper by Viswanathan *et al*. [42]. As mentioned earlier **c+a** slip (pyramidal) is much harder to activate than **a** slip (basal) due to a higher critically resolved shear stress. However as **a** slip can only deform parallel to the basal plane, as the crystal is rotated the need for **c+a** slip to accommodate the indentation grows. This makes the material tougher when the declination angle is 0° as dislocations will need to move normal to the basal plane. The inverse pole figure shown in Figure 20 illustrates this, by numbering grains in different orientations in terms of the highest to lowest hardness values. The crystals closest to the basal plane orientation are stiffer than crystals in other orientations.

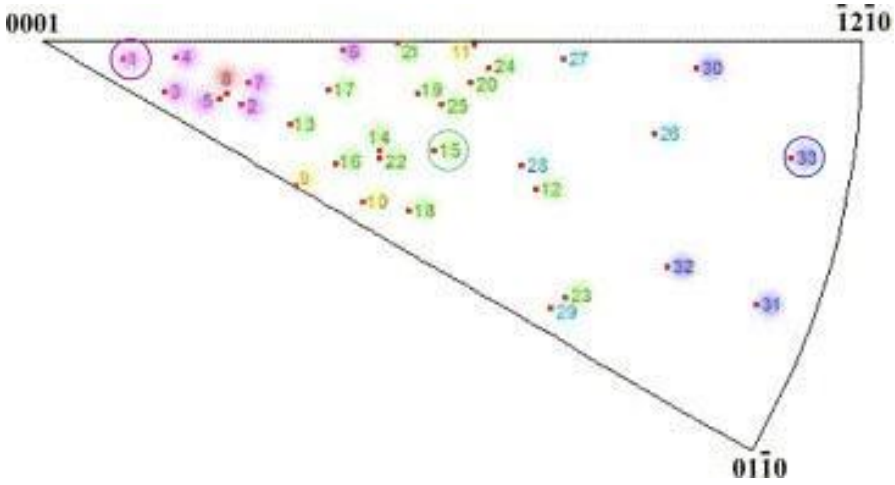

Figure 20: Inverse pole figure showing numbering various grains in order of highest to lowest hardness values **[42]**

An older study [43] had similar results, but tied this information to the activated slip systems at various orientations. They determined that should the tensile load be applied within an angle of 30° of the *c*-axis, the first slip system would activate (basal). In all other orientations they saw that the second prismatic slip system would be most active. This is illustrated in Figure 21. Going back to the above Figure 20, points 1 to 8 would be indents that formed through basal slip (the orientations labeled in pink).

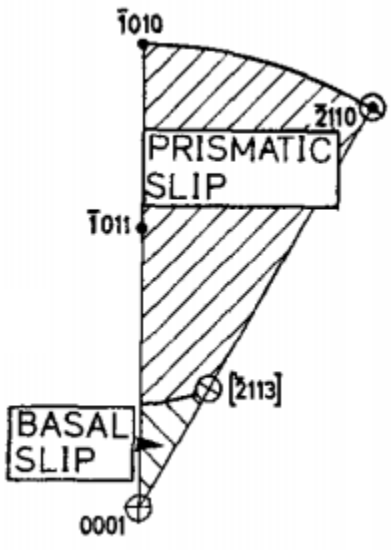

Figure 21: Inverse pole figure showing which slip systems will activate depending on crystal orientation with respect to the loading direction **[43]**

2.2 Microstructural Characterization and Experimental Techniques

There are a large number of analyses and experimental techniques available if one needed to have a closer look at a material. These techniques range from basic (optical microscopy) to complex (electron microscopy), and usually go hand in hand in hand with various fractography experimental techniques. Additionally there are also a handful of quantitative techniques available used to predict microstructural changes upon stress application. This section will be concerned with learning how these various systems operate and how they may be employed in order to study fracture.

2.2.1 Optical Microscopy

This commonly used technique can only study the surface of a material so the sample under observation needs to be polished and possibly etched prior to examination. Additionally optical microscopy (OM) is not very adept at demonstrating surfaces that are not perfectly horizontal (i.e. surface imperfections such as valley and pits would not demonstrate any perceived depth). Certain components of the microscope have been developed in order to counteract this issue, but they are of limited ability.

In studying the facture of materials, OM has been mostly utilized to study the effect of applied stresses/strains on microstructure. For example Figure 22 shows the development of twins in titanium as a response to tensile strains. Other similar studies are possible under an OM, such as analyzing surface void growth or slip band evolution. Additionally developments in testing technology has allowed for smaller tensile machines to be produced, so that they may fit within an optical microscope set-up. This allows for the real time observation of a materials surface microstructure as the tensile or compression tests are being conducted.

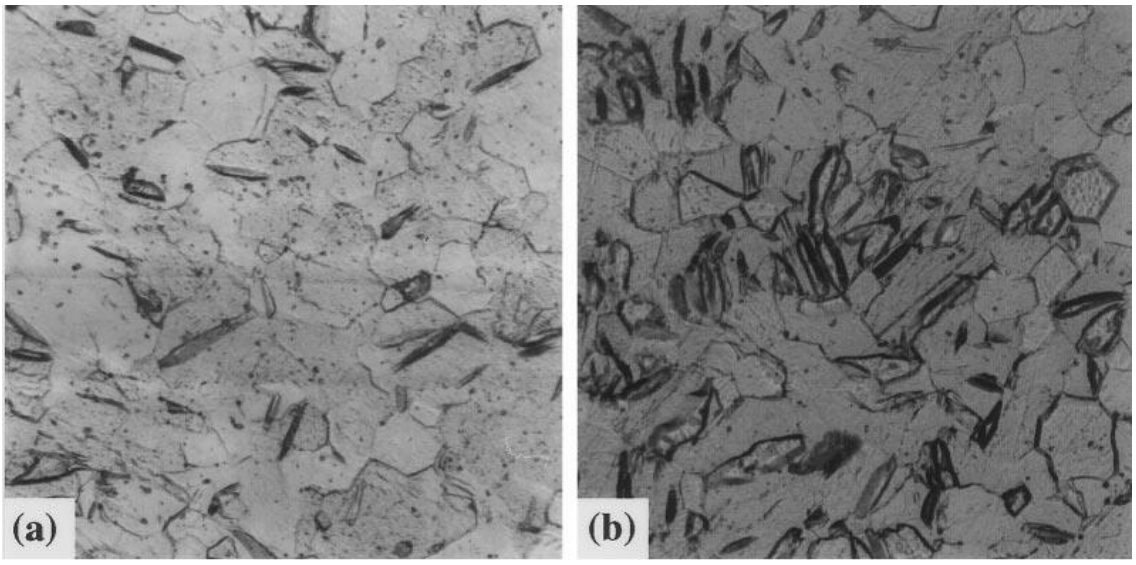

Figure 22: Optical micrographs of twins forming in titanium under a strain of (a) 6.5% and (b) 12% at 500x magnification **[23]**

2.2.1.1 Digital Image Correlation

Digital image correlation (DIC) is a process that could be used to analyze the localized strain evolution in tensile samples. The tensile sample in question would have one of its surfaces sparsely coated with tiny particles or speckles. Using optical microscopy and appropriate computer software, one could apply a tensile load on the sample while the camera records the movements of the particles [44]. The software records the random pattern twice: once in the reference undeformed state, and once after loading and deformation. This first picture is divided into small windows of a certain pixel width. The discrete matrix of grey level values of each window is recorded and forms a unique landmark or fingerprint within the image. Using a cross-correlation function the software can determine the correlation or displacement of each window between pictures, producing a displacement vector that represents the deformation. This is illustrated in Figure 23. Achieving the correct window size is important, since a finer mesh would result in better results but would also require a finer pattern, which may be hard to do depending on the length scale of analysis.

Typically the random pattern is added via aerosol paint but for finer strain analysis (i.e. when using higher resolution optical microscopes) or smaller tensile samples this may not be feasible; hence other methods were developed. One such process was put forward by Berfield *et al.* [45]. In order to achieve nano-sized speckles on polydimethylsiloxane (PDMS),

the polymer samples were exposed to ultraviolet light for 30 minutes in order to appropriate its surface chemistry for nanoparticle adhesion. A colloidal suspension of nanoparticles was prepared by dispersing silica nanoparticles (with a mean particle diameter of 140 – 180 nm) in ethyl alcohol, after treating the silica nanoparticles with rhodamine B isothiocyanate (a fluorescent dye). The nanoparticles were then applied onto the PDMS sample surface through a spin coating process that operated at 1,250 RPM. The final result is shown Figure 24. Such a process could potentially be applied onto metals.

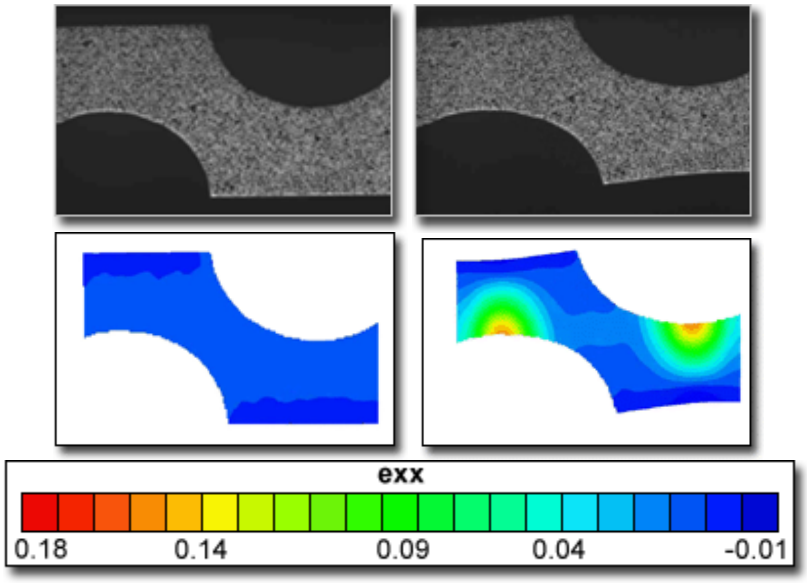

Figure 23: Before and after images of DIC performed on an aluminum sample with a speckle pattern added via spray paint **[46]**

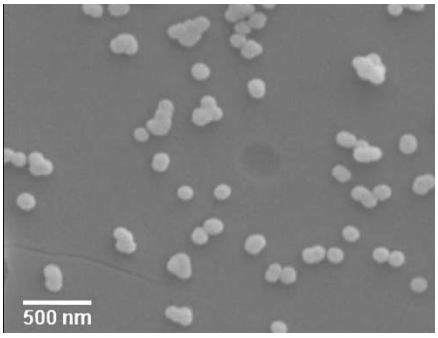

Figure 24: Transmission electron microscope image of silica nanoparticles on the surface of the PDMS polymer **[45]**

Digital image correlation has been successfully applied onto titanium alloys for microscale analysis [47] [48] [49]. In one of them they achieved a random speckle pattern through the

application of a fine powder (average particle size of 100 nm). By applying a load and studying a very small area (approximately 80x65 μm, with a resolution of 2400x2000 pixels) they produced a localized strain map. The ε_{xx} and ε_{yy} values along the length of the image are shown in Figure 25 at an applied stress of 500 MPa along the x-direction.

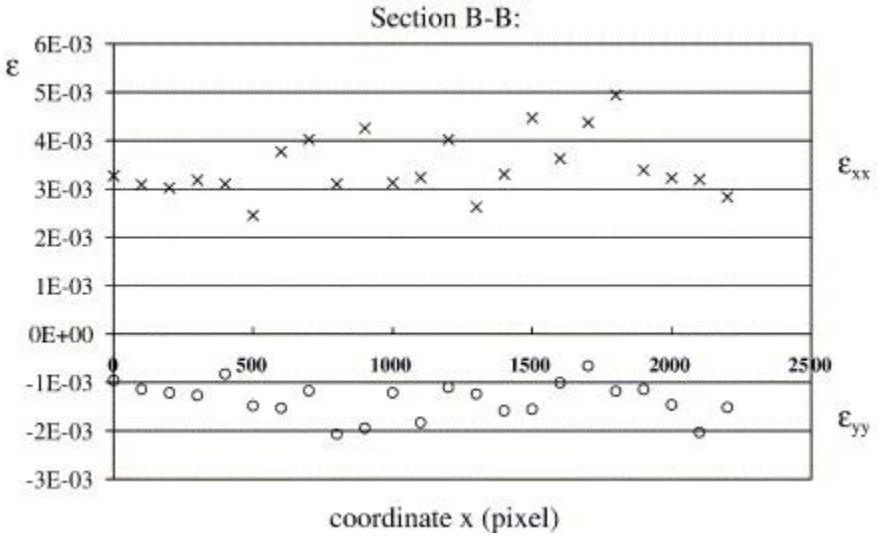

Figure 25: Strain values along a line of approximately 80 **μ**m length for a Ti-6Al-4V tensile sample; each pixel corresponds to approximately 32 nm **[47]**.

2.2.2 Electron Microscopy

An electron microscope can be considered to be a substantial upgrade to optical microscopy. These types of microscopes are in high demand particularly due to their extremely high resolving power. Normal optical microscopes utilize diffraction processes for illumination, which limit their resolution to about 200 nm (or 2,000 x); whereas electron microscopes can achieve resolutions up to 0.2 nm (or 2,000,000 x) [50]. While all electron microscopes work on the same basic principle, there are a number of different processes that may be used to resolve the "data" released when utilizing the electron beam.

2.2.2.1 Scanning Electron Microscopy

SEMs are one of the most utilized analysis processes in field of fractography. For example, Figure 26 shows an image of the fracture surface of a titanium plate used for osteosynthesis. One can clearly see the direction of fatigue propagation by analyzing the path of striation development, along with the presence of intergranular failure. SEMs can also be utilized to study basic surface structure such as oxide films or inclusions (see Figure 27). Similarly to

optical microscopy, it is now also possible to conduct real time SEM analysis of a material during a tensile or compression test.

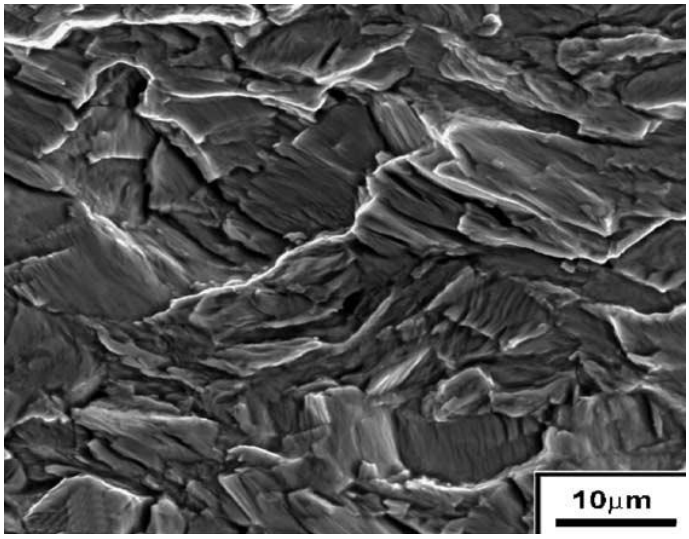

Figure 26: SEM image of fatigue failure in a titanium biological implant, where it is possible to view striation marks and intergranular cracking **[51]**

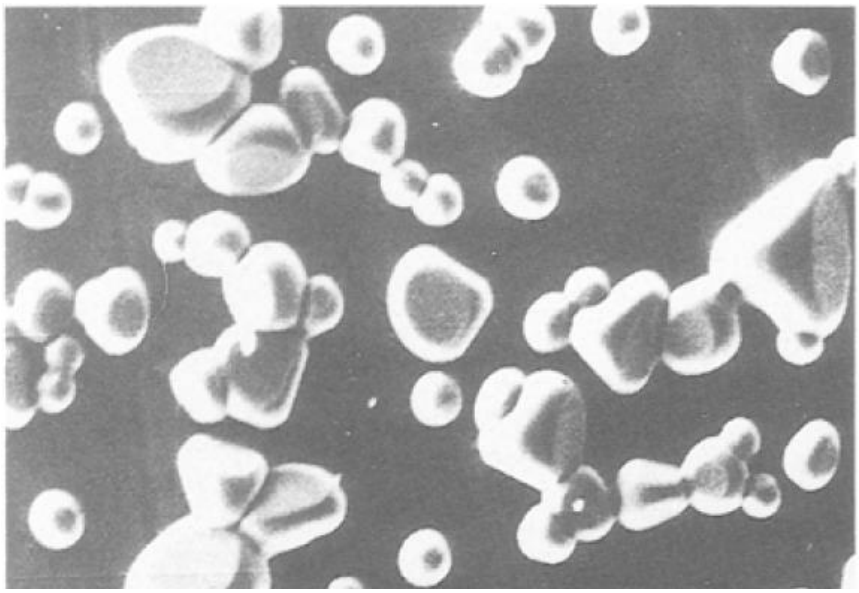

Figure 27: SEM image of copper oxide particles deposited on a hole surface **[52]**

2.2.2.1.1 Electron Backscatter Diffraction

When the electron beam in an SEM hits the specimen, the electrons can be diffracted by the different atomic layers in the material's crystal structure. By positioning a phosphor screen

so that it is in the diffracted electrons path, impingement of electrons occurs causing the formation of visible lines and patterns to develop on the screen [53]. This process is called Electron Backscatter Diffraction (EBSD) and the patterns developed are called Kikuchi bands or Electron Backscatter Patterns (EBSPs), and are effectively projections of the various planes in the material's crystal structure. By studying and processing these patterns it is possible to determine important texture information regarding the material crystal structure and orientations. Figure 28 shows an example of a Kikuchi band pattern.

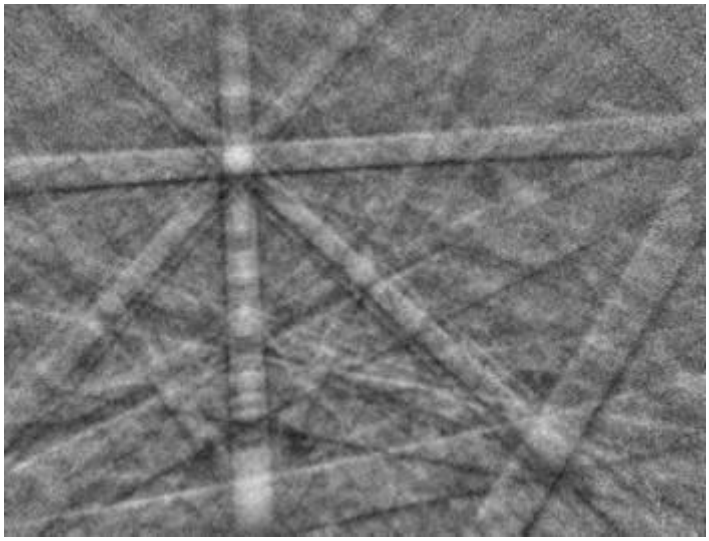

Figure 28: Kikuchi band for a material created via EBSD **[53]**

Using software analysis it is possible to process Kikuchi band patterns to examine the texture within regions of the material's microstructure in order to procure a large amount of valuable data regarding texture (see Figure 29). Most of this data is developed via the creation of the pole figure for the specimen in question (see Figure 30 and Figure 31). This process involves taking a grain in the microstructure and placing it at the center of an imaginary sphere with an axis oriented according to the sample's rolling, transverse and normal directions. The reference axis is chosen arbitrarily and, should it be required, could be modified to suit whatever analysis the experiment requires. The electron diffraction path for a certain crystal direction is projected outwards from the crystal and will intersect the sphere at various points (points 1, 2 and 3 in Figure 31). Lines are drawn from the intersection points to the sphere's south pole, which intersect the XY plane of the sphere (the plane formed by the rolling and transverse axis) at certain unique points (1', 2' and 3' in

Figure 31). This process is conducted on all the grains within the region of study in the specimen. The image produced on the XY plane of the sphere with the cumulative projections of all diffracted beams is called a pole figure.

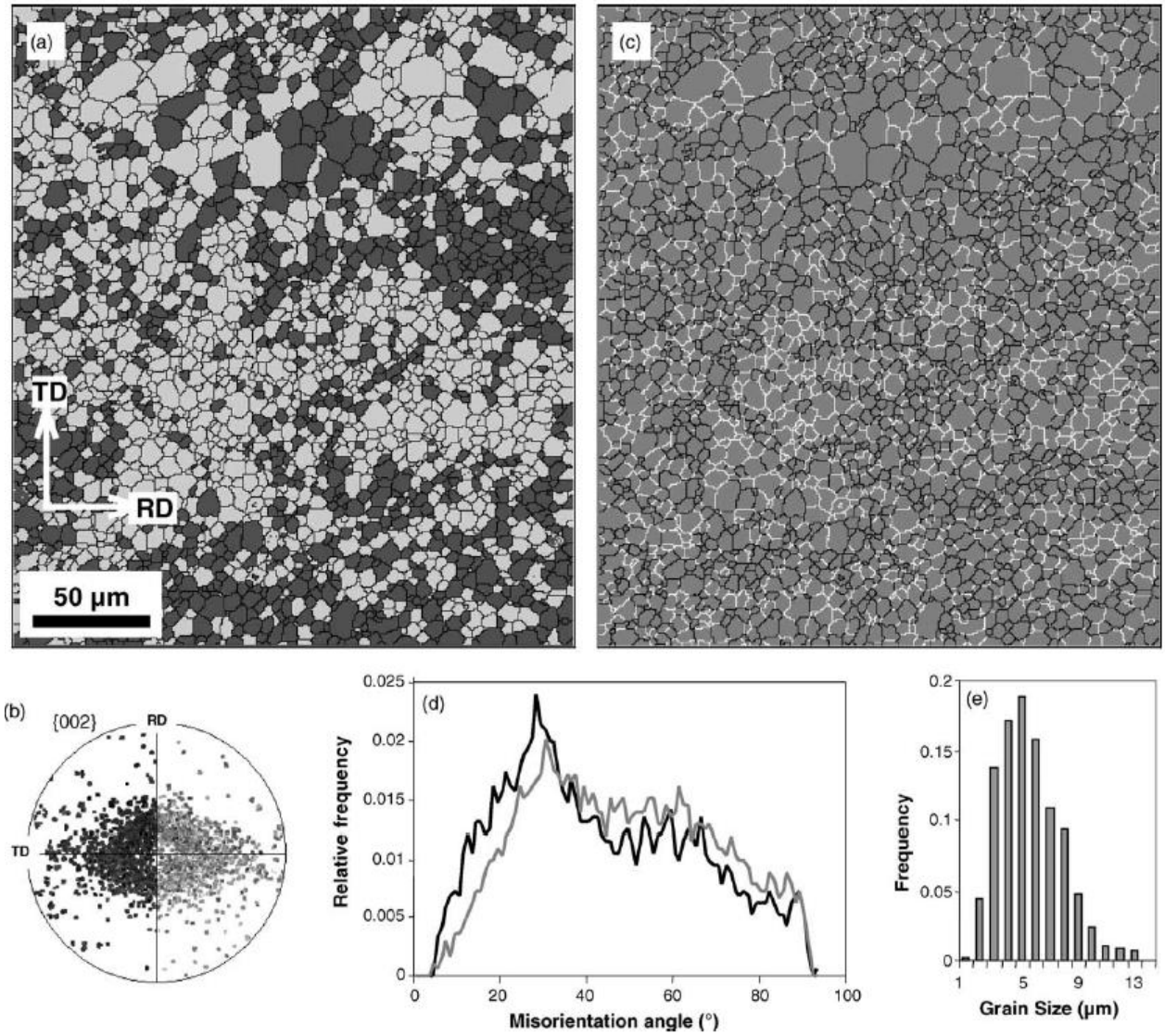

Figure 29: Examples of the data procured through EBSD analysis for a titanium specimen; (a) shows an EBSD map with the black lines corresponding to a grain boundary misorientation greater then 3°; the two different shades of grey marking the grains correspond to the two regions in the pole figure shown in (b); (c) shows the spatial distribution of the low (white) and high (black) angle misorientations; (d) shows the misorientation angle distribution and (e) shows the grain size distribution in this sample **[6]**

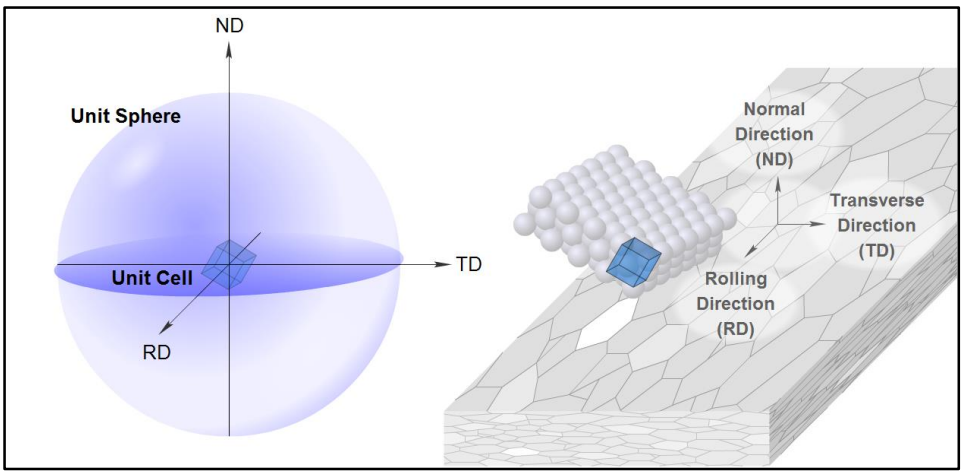

Figure 30: Illustration of how a crystal in a material is aligned with the pole figure sphere and axis **[7]**

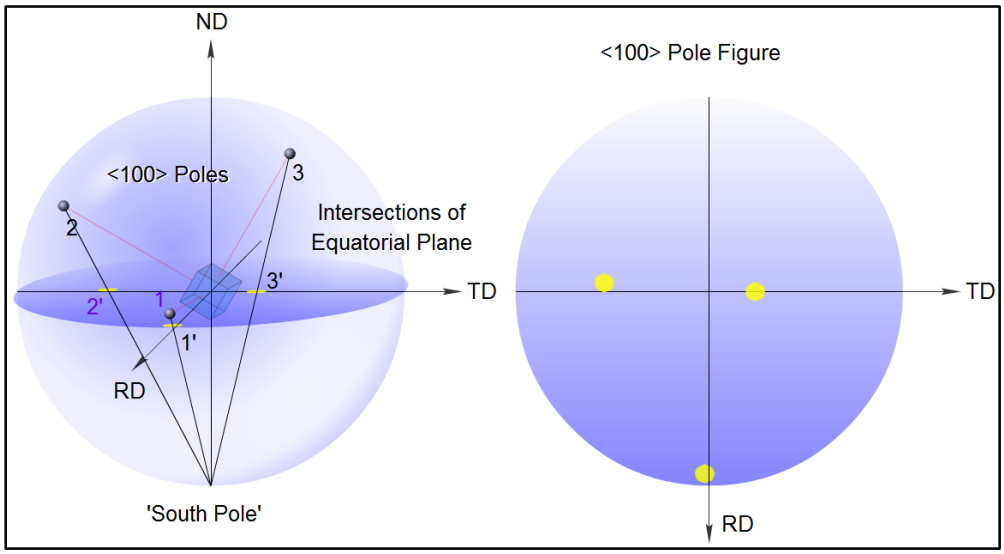

Figure 31: Creation of the pole figure by the diffraction pattern of the crystal at the center of the sphere **[7]**

Studying the EBSD data evolution of a metal sample under stress can result in an in-depth analysis of the texture evolution and microstructural behavior of the material.

2.2.3 X-Ray Tomography

X-ray tomography (XRT) is a non-destructive analysis technique that can visualize the interior geometry of solid objects [54]. This process works by beaming X-rays through a sample along several beam paths. A series of detectors measure the decrease in intensity of the exiting X-ray beams along a slice of the material in order to receive a tomography image of the cross-section. Collecting tomography images for cross-sections throughout the whole material and compiling them will produce a 3D image of the materials interior. This process

works similar to magnetic resonance imaging (MRI) process that is used in the medical industry. Figure 32 shows an example of a tomography scan produced via XRT.

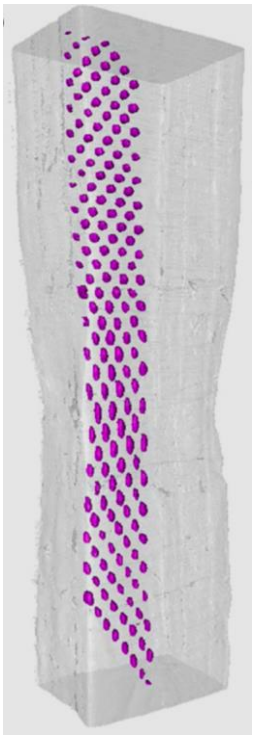

Figure 32: XRT image of a sample of copper under tensile stress with an array of voids in its interior **[55]**

The foremost advantage of utilizing this process is the ability to view the interior of a material in a non-destructive matter. XRT has already been utilized in studying the effect of void growth and coalescence in materials, providing valuable insight into how the process works in bulk materials (overcoming the limitations of 2D modeling of such behavior). A disadvantage of this process is that the smallest achievable resolution is between 1000 to 2000 times the object's cross sectional diameter [54]. This means that a larger test specimen would not be able to produce the same scale imaging as a smaller specimen due to the bulk material interfering with the x-ray path. Additionally of all the analysis and microscopy methods so far, XRT is the hardest to conduct due to limited availability and high cost of such machines.

2.2.4 Experimental Techniques

This section is concerned with the various experimental techniques that could be applied in conjunction with the microscopy and observational techniques mentioned over the past few

sections. While there are a much larger quantity of available techniques that could be used to study the fracture process, the processes discussed are some of the more common and feasible techniques available.

2.2.4.1 Fractography

Studying the fracture surface of a material is the most common and easiest method used to understand its fracture process. Depending on the available analysis techniques (e.g. optical microscopy versus scanning electron microscopy), the level of detail and type of surface features seen may vary. Typically fractography is focused on determining the site of crack or void nucleation and propagation on the fracture surface, which will in turn help determine the cause of failure and provide insight into how such a failure mode may be avoided or, at the very least, delayed. Typical fracture surfaces include phenomena such as beach marks and striations (in the case of fatigue failure), voids, inclusions, dimples and cleavage [56]. By examining the relative positioning of such phenomena and their interactions with each other, the cause of failure may be determined.

While such a method can be carried out very easily due to the presence of very little sample preparation, information on subsurface activities or deformation history can be hard to procure. Additionally this is a destructive experimental process and would not be able to be applied in cases where a material or system component would need to return to service post-inspection. While most fractography techniques result in a 2D image produced for analysis, it is possible (yet also more difficult) to conduct 3D analysis using stereoscopic processes or atomic force microscopy techniques.

2.2.4.2 Polishing

Polishing a specimen entails grinding and etching away the top layer of material in order to study its subsurface. Grinding is done typically using papers of various roughness made of silicon carbide. The grinding typically begins with using a silicon carbide sheet with a high coarseness, with subsequent passes involving increasingly smooth silicon carbide sheets. Eventually the silicon carbide sheets are replaced by cloth sheets coupled with diamond pastes. The last step of the polishing process involved etching the material surface using an

etchant chemical that depends on the type of material under examination (e.g. titanium requires the use of a colloidal silica and hydrogen peroxide solution).

Polishing a material prior to examination is required in order to see grains at the surface of a material, and is a critical step in sample preparation for various microscopy methods (e.g. EBSD or OM). Polishing can be a very time consuming effort and could mechanically alter the material's microstructure (however the latter does not happen to a large extent and only affects microstructural effects such as voids). There is also a limited polishing resolution possible due to manufacturing limitations for the polishing sheets and chemicals.

2.2.4.3 Etching

Etching is a process where a sample is exposed to a certain chemical (typically an acid, called an etchant) in order to expose the microstructure of its surface. The etchant attacks the surface and removes material. Certain microstructural aspects will be more prone to attack than others, such as grain boundaries or second phase particles, strengthening the visual texture of the material.

An advantage of using etching is that it can be time efficient for most metals (ranging from 15 seconds to a few minutes). However it typically requires the use and mixture of strong acids (such as hydrofluoric acid and hydrogen peroxide, a common titanium etchant combination). Certain etchants can even produce color tints, showcasing varying grain orientations with different colors. This occurs due to changes in thickness of the oxide film formed on the specimen surface. Kroll's reagent (100ml H_2O, 2ml HF, 5ml HNO_3) can be used to accomplish this in titanium [57]. An example of titanium etched with Kroll's reagent is shown in Figure 33.

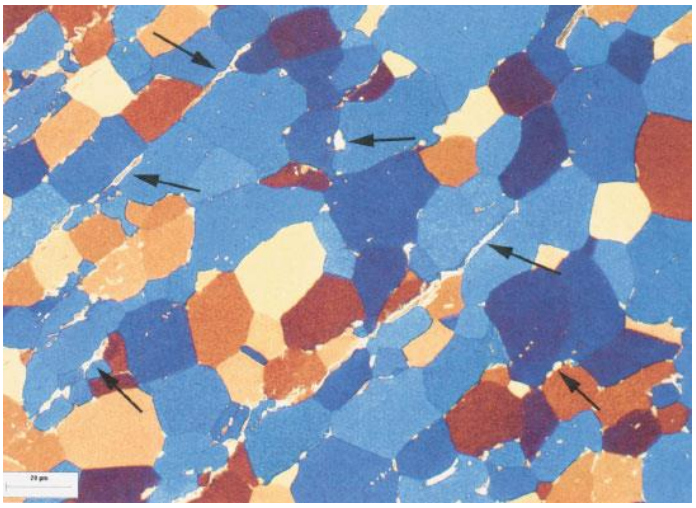

Figure 33: Microstructure of commercially pure titanium etched with Kroll's reagent showing equiaxed grains; the arrows point to the remnants of beta phase grain boundaries **[57]**

2.3 Fracture Modeling

2.3.1 Ductile Fracture modeling

Research on the ductile fracture process has determined a number of ways one can measure and predict plasticity phenomena occurring in a material. This section will first study various empirical and analytical models pertaining to the three stages of ductile fracture (void nucleation, growth and coalescence) along with relevant experimental details. Following that, previous finite element method (FEM) research into material plasticity will be discussed.

2.3.1.1 Void Nucleation

Previously it was mentioned that void nucleation occurs due to localized lattice decohesion in a material under stress. Decohesion occurs due to dislocation pile-ups at lattice inconsistencies such as grain boundaries, inclusions or twins. The energy provided by the applied stress is partially directed towards creating a new surface at the lattice imperfection in question. Once the critical energy state is achieved then atomic bonds are broken and voids are formed. It should be noted that decohesion is most common at the interface between a particle and the lattice matrix [14]. In a tensile test, voids tend to nucleate at the particle-matrix interface along the tensile axis and at the larger particles within the particle size distribution [58].

As the particle size increases, a transition occurs from void nucleation at the particle-matrix interface to nucleation due to particle fracture [59]. This transition point shifts according to a large number of variables (e.g. bond strength between particle and matrix, and ratio of the particle/matrix atomic radii). A paper published by Gurland *et al.* [60] puts forward the idea that particle fracture occurs when the strain energy released by the particle is larger than the crack surface energy. They approximated this using the following equation:

$$\sigma = \frac{1}{q}\left(\frac{E\gamma}{a}\right)^{1/2} \qquad \text{Eq. \{8\}}$$

where σ is the fracture stress, q is the stress concentration factor, E is the material's Young's modulus, γ is the specific crack surface energy and a is the particle diameter. Equation 8

assumes that the stress field of the particle and the crack have dimensions of the same magnitude. Using this approach Gurland demonstrated that the stress required for particle fracture increases with decreasing particle size and increasing bulk fracture toughness of the particle.

A study by Ashby took the other route and was the first to propose a model for void nucleation by particle-matrix decohesion [61]. He suggested that decohesion occurs when a critical stress value was achieved, via tensile stresses brought about by slip bands and vacancy loops surrounding a particle. This critical stress value can be approximated by:

$$\sigma_T \sim \frac{\varepsilon R}{lb} \qquad \text{Eq. \{9\}}$$

where σ_T is the critical tensile stress at decohesion, ε is plastic strain, R is the radius of the particle, b is the Burger's vector and l is the length of the array of prismatic loops. The value of l can be substituted for half the particle spacing in the case of an array of particles or, in the case of widely spaced particles, the spacing of active slip bands. The critical stress is achieved at lower strains for larger particles and vice versa.

Brown *et al.* proposed another way in which to predict particle-matrix decohesion [62]. They suggested that void nucleation would not occur until the elastic energy stored in the particle was greater than the nucleated void surface energy. This condition can be represented by the following (simplified) equation:

$$\frac{1}{3}\,\mu^*\, r_o\, \epsilon_p^{*2} \;>\; \gamma \qquad \text{Eq. \{10\}}$$

where μ^* is the shear modulus of the particle, r_o is the particle radius, ϵ_p^* is a measure of the incompatibility between the matrix and particle deformation and γ is the surface energy of the void. γ may be substituted by $\gamma_M + \gamma_P - \gamma_{PM}$ (the surface energies of the matrix, the particle and the particle-matrix interface respectively). Equation 10 demonstrates that voids nucleate at small particles expressing large strain incompatibilities with the matrix, or vice versa.

Goods *et al.* expanded on Equation 10 by including factors such as hydrostatic pressure, flow stress and interfacial stress [63]. They put forward the following expression for void nucleation strain:

$$\varepsilon_c \geq 1.7 \frac{r}{b}\left(\frac{\sigma_I - \sigma_H - 3\sigma_O}{\mu}\right)^2 \left(1 + 3f_v + \frac{f_v^{1/2}}{1.8}\right)^{-2} \quad \text{Eq. \{11\}}$$

where ε_c is the nucleation strain, r is the particle radius, b is the Burger's vector, σ_I is the stress at the particle-matrix interface, σ_H is the hydrostatic pressure, σ_o is the Orowan stress, μ is the shear modulus of the matrix and f_v is the volume fraction of the particles throughout the matrix. Equation 11 predicts the strain required for void nucleation increases with particle size. However this increase in particle size leads to a decrease in yield strength of the material, which is also followed by higher nucleation strains.

Experimental evidences for void nucleation in titanium have been shown to agree with the above statements. Particularly in equiaxed α-titanium alloys, it has been demonstrated that voids nucleate primarily at the interface between the matrix and inhomogeneities (particles) and, to a lesser extent, within the particle (particle fracture) [64]. The same study also found that ageing and subsequent quenching was not a factor in determining void formation if the microstructure of the alloy was similar to that of martensite. Similar experiments on α+β titanium alloys show that voids will nucleate along the interfaces between the two phases (see Figure 34) and also at twin boundaries.

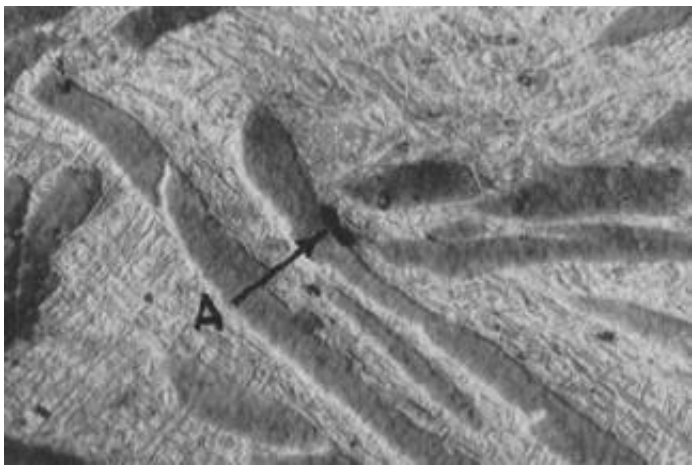

Figure 34: Void formation at the α/β boundary in a Ti-5 Al-5 V alloy **[64]**

One study on the titanium alloy Ti-6Al-4V showed that shear bands are also potential sites of void nucleation [65]. The high stresses within the band nucleate voids which grow initially up to the edges of the band, and then elongate in the direction of the band. Further growth is supplemented by rotation along the direction of the band. Eventually the voids coalesce to form a crack. This process is shown in Figure 35.

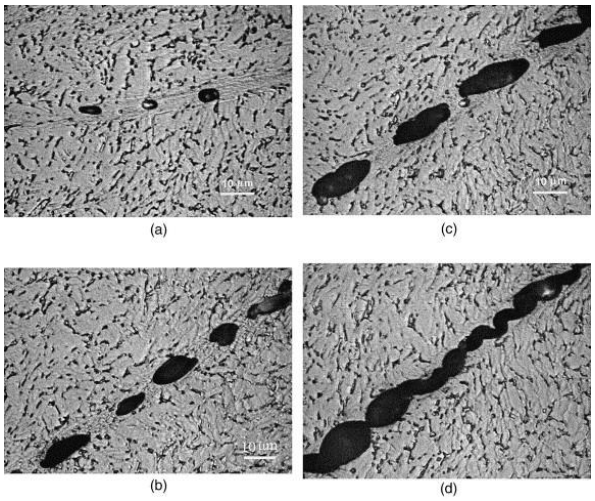

Figure 35: Void nucleation, growth and coalescence within a shear band in Ti-6Al-4V **[65]**

The shear bands themselves nucleate at "internal boundaries" of the specimen (meaning at particle, grain boundaries, dislocation pile-ups or other microstructural artifacts). In terms of material properties, it has been shown that the materials thermal conductivity can also affect the formation of shear bands [66]. Materials with a high thermal conductivity will witness thermal softening while under deformation. The softened areas will be preferred areas of shear band and void nucleation. In materials with a low thermal conductivity like pure titanium and low-carbon steel, geometrical imperfections will play a larger role in determining the sites of void nucleation.

2.3.1.2 Void Growth

Once a void has been nucleated within a reasonably ductile material, it will subsequently grow in size, with the resulting shape and volume of the void being dictated by material properties and testing conditions. Brittle materials do not exhibit void growth. Void growth occurs due to dislocation motion towards the void surface, with slip bands being evident on the void surface area.

Ashby proposed a model for void growth based on dislocation movement which is as follows [61]:

$$\frac{\Delta V}{V} \sim \frac{a}{2} \qquad \text{Eq. \{12\}}$$

where ΔV is the increase in volume of void, V is the volume of the particle at which the void is nucleating and a is the localized shear strain acting on the primary slip band. However it has been demonstrated by Rosenfeld that this model underestimates the growth rates of voids, primarily since it only takes into account the localized high stresses dislocations apply on particles and not how they may affect void growth [67].

Although void growth is a dislocation based process, very few dislocation based models have been developed, possibly since continuum mechanics models of this process have proved to be rather reliable. The first such model presented was by McClintock [68]. He provided 2 equations that can be used to predict the growth of circular and elliptical voids for materials with various work hardening properties. The model for elliptical voids is as follows:

$$\ln\frac{R}{R_o} = \frac{\varepsilon\sqrt{3}}{2(1-n)}\sinh\left[\frac{\sqrt{3}(1-n)(\sigma_1 + \sigma_2)}{2Y}\right] + \left(\frac{\varepsilon_1 + \varepsilon_2}{2}\right) \qquad \text{Eq. \{13\}}$$

where R is the instantaneous mean radius of the elliptical void, R_o is the original mean radius of the void, ε is the far field true strain in the sample, n is the work hardening factor, σ_1 and σ_2 are the applied stresses in the two principal directions (tensile and transverse directions), ε_1 and ε_2 are the strains in the principal directions, and Y is the mean stress acting on the material. The value of n is 0 for a non-hardening material, 1 for a linear hardening material and between 0 and 1 for an intermediate hardening material. Note that in the case of a linear hardening material, it is mandatory to use the sine-limit law to retrieve a result:

$$\lim_{x\to 0}\left(\sin\frac{xa}{x}\right) = a \qquad \text{Eq. \{14\}}$$

Equation 13 above simply shows a correlation between applied stresses/strains and the mean radius of the void. As the applied stresses and strain increase, the mean radius of the void would increase. For the case of uniaxial loads (which results in elliptical voids) the radius of the void along the tensile axis will increase, while the radius of the void in the transverse direction will decrease. However the rate at which the tensile radius grows is larger than the rate at which the transverse radius shrinks, leading to an increasing mean radius value.

Similarly to Ashby's model, Equation 13 has been shown previously to underestimate the extent of void growth [14]. In a study studying ductile fracture in Al-Mg alloys, it was experimentally demonstrated that McClintock's model is accurate at low values of the far field true strain (see Figure 36) [69]. As the far field strain value increases, McClintock's predictions are contain larger error margins. Previous studies have shown that the growing discrepancy is due to McClintock not taking into account the stress-triaxiality (the ratio of mean applied stress to yield stress) within the sample [70].

Rice *et al*. derived models that overcome this issue [71], which were modified into integrated forms by Thomason [72]. The Rice-Tracey model demonstrates the growth of a spherical void in a rigid and perfectly plastic material and is represented by the following integrated equations:

$$R_1 = R_o \left[e^{D\varepsilon_1} + \frac{1+E}{D}\left(e^{D\varepsilon_1} - 1\right) \right] \quad \text{Eq. \{15\}}$$

$$R_2 = R_o \left[e^{D\varepsilon_1} - \frac{1+E}{D}\left(e^{D\varepsilon_1} - 1\right) \right] \quad \text{Eq. \{16\}}$$

where R_1 and R_2 are the radii of the elliptical void in the tensile and transverse directions respectively, R_o is the initial spherical void radius and ε_1 is the logarithmic strain over the whole strain path. D and E are parameters used to take into account the effect of volume and shape changes of the void. The value of $(1+E)$ is $5/3$ in the case of strongly hardening material and is 2 when the material is non-hardening.

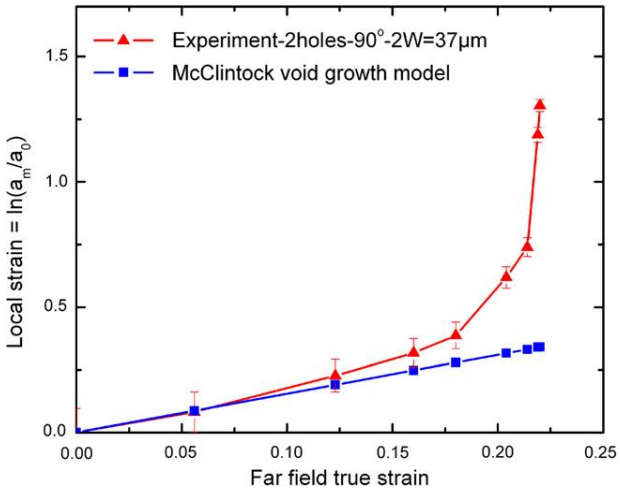

Figure 36: Experimental data versus McClintock predictions for void growth in an Al-Mg alloy tensile sample **[73]**

The parameter D in Equations 15 and 16 can be calculated using the following formula:

$$D = 0.558 \sinh \frac{3\sigma_m}{2\sigma_Y} + 0.008 \cosh \frac{3\sigma_m}{2\sigma_Y} \qquad \text{Eq. \{17\}}$$

where σ_m is the mean applied stress (the Von Mises stress) and σ_Y is the yield stress of the material. The ratio of these two terms is defined as the stress triaxiality. These three equations dictate that the void length in the tensile direction will grow with increasing applied stress and strain, while the void length in the transverse direction will decrease with increasing applied stresses and strain. This leads to the evolution of the initially spherically void into an elliptical void.

Another study into ductile processes in α+β titanium alloys demonstrated the effects of lattice texture and geometries on void growth [74]. It was experimentally shown that void growth is linear with strain (see Figure 37) and, as mentioned previously occurs along the interfaces between two phases or boundaries. Additionally it was shown that the void growth rates in these titanium alloys increase with β-particle size, mean free path between particles and grain boundary thickness with certain limitations (see Figure 38).

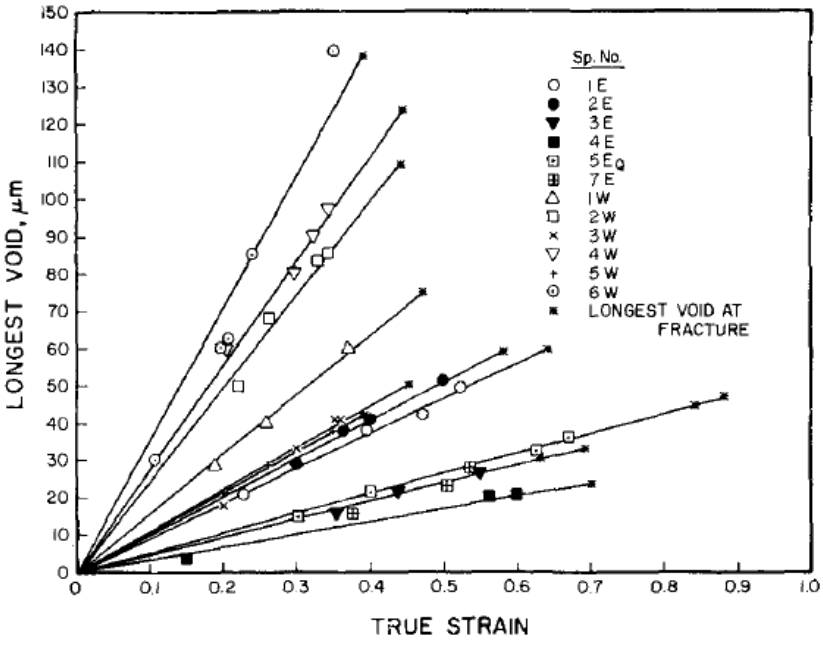

Figure 37: Experimentally derived values of the length of the longest void in a number of titanium alloy samples as a function of true strain **[74]**

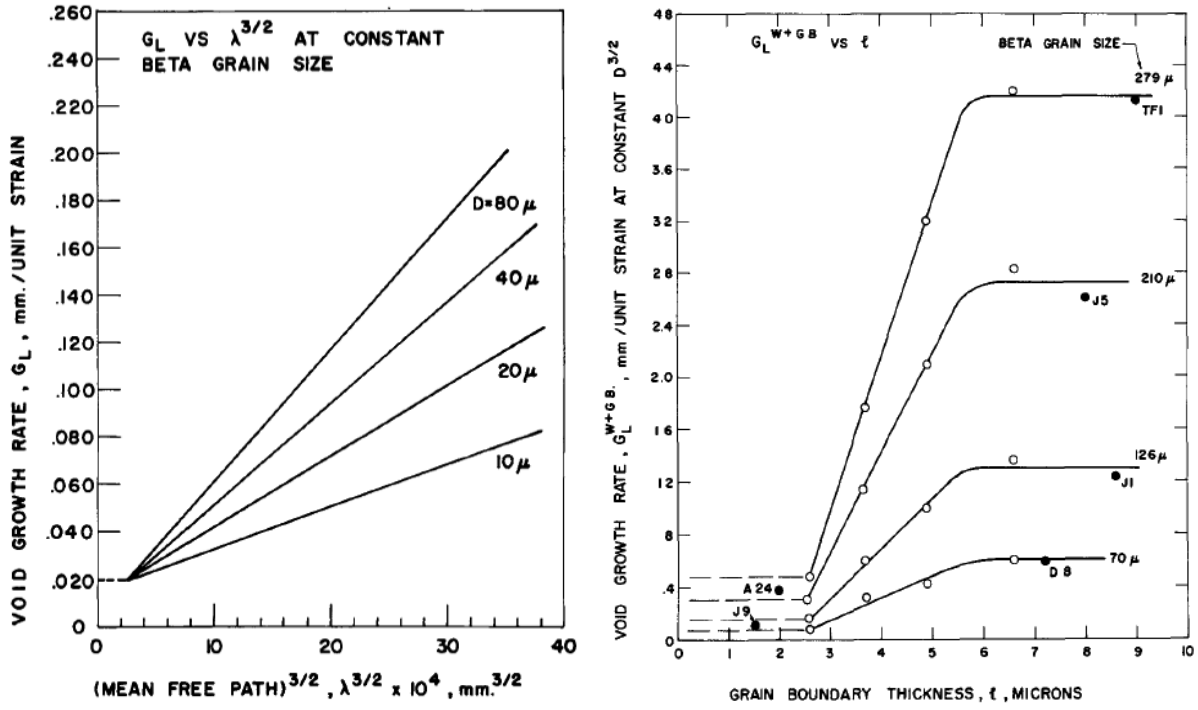

Figure 38: The effect of mean free path (left) and grain boundary thickness (right) on void growth rates in titanium alloys **[74]**

The initial plateau region in the growth rate-grain boundary graph is assumed from similar tests on equiaxed α-titanium alloys to be the base void growth rate. The second plateau region occurring at larger grain boundary thicknesses is due to the grain boundary being

large enough for dislocations to move unimpeded past them. This is primarily since the pile-up of dislocations at the interface is strong enough to overcome any restrictions the interface may present.

2.3.1.3 Void Coalescence

Void coalescence is the last stage in the ductile fracture process. As strain on a specimen increases, voids grow in volume. If voids are sufficiently close to each other they will link at a certain point to form a larger void. The effect of this process occurring repeatedly in a tensile specimen is either stable or unstable fracture.

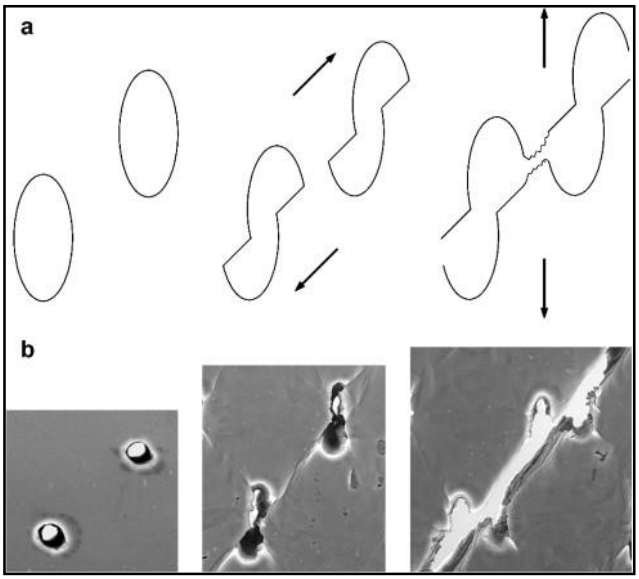

Figure 39: Schematic of the void growth and coalescence by shear (a) and the same process occurring in an Al-Mg alloy (b) **[69]**

McClintock *et al*. was one of the first research groups to develop a model for void coalescence, however in this case it was a model for coalescence by shear [75] (see Figure 39). They stated that the plane strain condition for coalescence in the shearing direction is as follows:

$$\frac{2W}{2c} = e^{\left[\frac{\bar{\varepsilon}\sqrt{3}}{2(1-n)}\sinh\frac{2(1-n)}{2} + \ln\sqrt{1+3\bar{\varepsilon}}\right]} \qquad \text{Eq. \{18\}}$$

where *2W* is the distance between the centers of the two voids, *2c* is the intervoid spacing between the two voids, $\bar{\varepsilon}$ is the far field true strain and *n* is the strain hardening exponent. McClintock *et al*. state that shear coalescence occurs once this condition is met. This model

is more accurate when considering an array of voids, as opposed to studying only two voids within a sample [69]. This is a result of the constraining effect of the material surrounding the void preventing the voids from easily achieving shear coalescence.

Brown and Embury stated that void coalescence occurs when shear bands can be drawn at a 45° angle between the growing voids [76]. This is the geometrical equivalent to the point where the void length in the tensile direction is equal to the intervoid spacing. While not an empirical model for describing void coalescence, the application of this idea can be easily carried out by plotting the variations of void major diameter (tensile length) and intervoid spacing versus strain. The intersection of the two curves would then be considered the point of void linkage. This model has been shown to be accurate in titanium based ceramic metal matrix composites [77] and Al-Mg alloys [69], with the exception being when the voids are at 45° angles with the tensile axis or when the intervoid spacing is relatively low.

Thomason defined the onset of void coalescence as the point where one of the following two conditions is met [72]:

2D model

$$\frac{\sigma_m}{\sigma_y} + \frac{1}{2} = \left[\frac{0.3A_{n-2D}}{(a/c)(1 - A_{n-2D})} + 0.6\right](1 - V_f)^{-1} \quad \text{Eq. \{19\}}$$

3D model

$$\frac{\sigma_m}{\sigma_y} + \frac{3}{2} = \left[\frac{0.1}{\left(\frac{a}{e}\right)^2} + \frac{1.2}{\left(\frac{c}{c+e}\right)^{1/2}}\right](1 - V_f)^{-1}\left[1 - \left(\frac{3\sqrt{\pi}}{4}V_f\right)^{2/3}\left(\frac{b}{b_o}\right)^2 e^{\varepsilon_1}\right] \quad \text{Eq. \{20\}}$$

where σ_m is the mean applied stress, σ_y is the yield stress, $A_{n\text{-}2D}$ is the area fraction of the intervoid matrix, a is the major radius of the void (tensile radius), c is the minor radius of the void (transverse radius), V_f is the initial void volume fraction, e is the half of the intervoid spacing, b is the void radius in the second transverse direction, b_o is the initial void radius in the second transverse direction and ε_1 is the applied plastic strain. The 2D case of Thomason's model has been shown to be rather inaccurate with a 45% underestimation of coalescence strain (however this may be due to the experimenter's definition of coalescence not being the same as Thomason's) [69]. The 3D case of the model has a large diversity of error margins, depending on the angle of void placement [73].

2.3.2 Brittle Fracture modeling

As mentioned previously in Section 2.1.3.1 Ductile Behavior versus Brittle Behavior, brittle fracture occurs primarily through cleavage. Cleavage cracks could produce transgranular fracture (cracks forming and propagating through a grain) or intergranular fracture (cracks forming and propagating through grain boundaries). Cracks may also form through a pile-up of dislocations at a microstructural artifact, similar to void nucleation.

Alan Arnold Griffith laid the foundation of brittle fracture theory, circa 1921 [78]. He noticed that the fracture strength of a material was always lower than its theoretical cohesive strength. This is due to the inherent defects in brittle materials leading to stress concentrations, lowering the fracture strength. He put forth the Griffith criterion for brittle fracture, which states that crack propagation occurs when the released elastic strain energy is equal to the energy required to form a new crack surface. This can be summed up in the following equation (for plane strain situations):

$$\sigma = \left(\frac{2E\gamma_s}{(1-\upsilon^2)\pi a}\right)^{1/2} \quad \text{Eq. \{21\}}$$

where σ is the stress required to propagate an existing crack of length $2a$, E is the elastic modulus of the material, γ_s is the surface energy, υ is Poissons ratio and a is half the length of the crack. However this only applies to completely brittle materials, like glass.

In reality metals are not completely brittle and undergo certain amounts of plastic deformation prior to fracture. Hence the fracture stress is increased due to the blunting of the crack tip. Irwin [79] and Orowan [80] suggested adding a modification to the above equation that takes into account the plastic work γ_p:

$$\sigma = \left(\frac{2E(\gamma_s + \gamma_p)}{(1-\upsilon^2)\pi a}\right)^{1/2} \quad \text{Eq. \{22\}}$$

The Griffith theory only works for cracks that have already nucleated in the material. Clarence Zener [81] and Stroh [82] showed that crack nucleation occurs when the shear stress created by a pile-up of dislocations reaches a threshold value:

$$\tau_s \approx \tau_i + \left(\frac{2\gamma_s}{nb}\right) \quad \text{Eq. \{23\}}$$

where τ_s is the shear stress, τ_i is the lattice friction in the slip plane, n is the number of pile-up dislocations and b is the Burgers vector. This applies for cracks nucleating at a grain boundary.

Stroh made an addition to the model that took into account the grain size d. He suggested the length of the dislocation pile-up spans half the grain ($d/2$), nucleating a microcrack with an effective shear stress of:

$$\tau_{eff} = \tau_y + \tau_i \sqrt{\frac{E\pi\gamma_p}{4d(1-v^2)}} \quad \text{Eq. \{24\}}$$

where τ_{eff} is the effective shear stress and τ_y is the shear yield stress for that slip plane. The limitation of this model is that it only takes into account the shear stresses acting on the slip band.

2.3.3 Finite Element Methodology

The finite element method (FEM) is a process with which one can simulate the effects of external stimuli on an object. By dividing the object into a mesh consisting of a large number of "nodes" or "elements", it would be possible to apply partial differentials (specific to the properties under analysis) to each of these elements for incrementing time steps. For a specific time step, the differential equations are solved for every node using the data procured from calculations from the previous time step (the first time step calculations would obviously be calculated using initial boundary conditions). The results of calculations at each node influence the results at the surrounding nodes. Calculations are repeated for that time step until the results reach equilibrium. Once this is achieved the whole process is repeated for the next incremental time step. An example of a meshed single cubic shaped grain with a void at its center is shown in Figure 40.

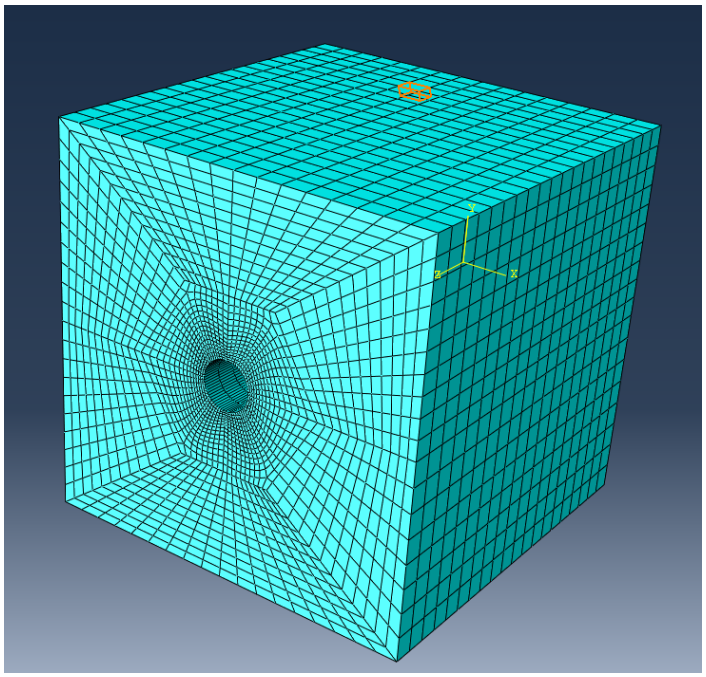

Figure 40: A model of a single crystal with a void propagating through its center, with its mesh defined in a symmetrical manner

Due to the immense number of calculations involved, contemporary FEM analysis is conducted using certain software packages, such as Abaqus FEA or COMSOL Multiphysics. The development of constitutive equations for use within simulations is dependant primarily on physical experimental data. However as research continues in materials and mechanical phenomena, the reliance on experimental data will decrease since FEA packages will be fine-tuned to a greater degree of accuracy.

Such programs are readily equipped to deal with engineering problems with a large length scale; however when dealing with micron and sub-micron length scales these packages sometimes provides skewed and incorrect results. This is primarily due to an issue of continuum bulk mechanics versus localized material effects. As such there have been recent efforts to address this issue through the development of models or subroutines (mini programs equipped to run within Abaqus utilizing specific material behaviour and definitions).

For anisotropic metals such as titanium it is critical that microstructural geometries such as grain orientations be taken into account when dealing with smaller length scales (as in the case of plasticity phenomenon like void nucleation, growth and fracture). Previous studies

have been conducted into determining constitutive equations for void growth and coalescence in anisotropic materials.

A study by O'Regan *et al*. [83] analyzed void growth in HCP single crystals of WC-Co composites via FEM simulations coupled with constitutive equations developed in house (but based on theories put forward in [84]). For the case of a single crystal O'Regan stated that plasticity is described only by shear flow, which is a function of the various slip systems present, with no twinning effects taken into consideration. The results show that lattice orientation (equivalent to grain orientation with respect to tensile direction in this case) is less significant than the effect of slip system orientation on void growth. More importantly it highlights the importance of remeshing when running simulations. As a simulation is carried out, the object under analysis and its mesh will deform. Some areas within the mesh will deform more than others, leading to a larger spacing between nodes in these regions which will affect output results negatively (Figure 41). Therefore depending on the problem at hand it would be wise to remesh the whole simulation once a certain mesh distortion threshold is reached.

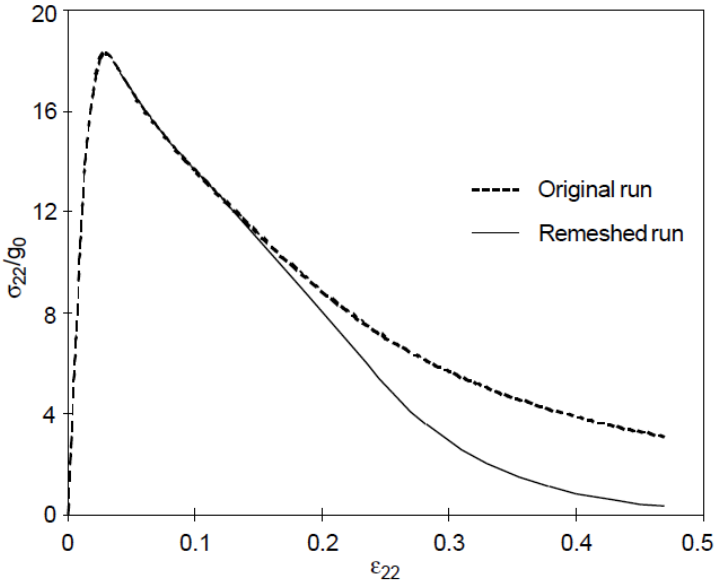

Figure 41: Comparison of true stress-strain behavior for remeshed and non-remeshed simulations of WC-Co single crystal void growth **[83]**

A more recent study looked at general anisotropy in plastic solids [85]. Voids in a HCP material are distributed homogeneously throughout the lattice and a FEM simulation is run

using anisotropy parameters [86] and a cell model that accounts for void volume fraction, void aspect ratio and cell aspect ratio (representing the anisotropy in void distribution). Deformation was characterized by the stages of void growth and coalescence. Through the study of void aspect ratios it is possible to quantitatively demonstrate the point where void linkage begins (Figure 42). The linkage point is also demonstrated by a drop in the load carrying capacity of the unit cell (i.e. a drop in the stress-strain curve).

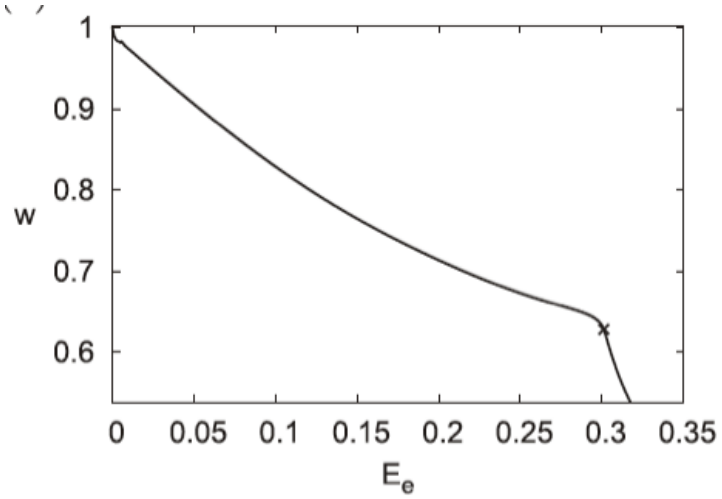

Figure 42: Evolution of void aspect ratio with respect to tensile strain; the X marks the onset of void coalescence **[85]**

Furthermore it was determined that void shape has very little effect on the evolution of ductile fracture within the material, as shown in the relationship between volume fraction of voids versus strain in Figure 43. The anisotropic material labeled *(ib)* is modeled such that it performs better under tension compared to shear, while material *(iii)* works in the opposite manner. Additionally it can be determined from the same image that once void coalescence occurs (data to the right of the X) the amount of anisotropy present does not affect void volume fraction growth rates.

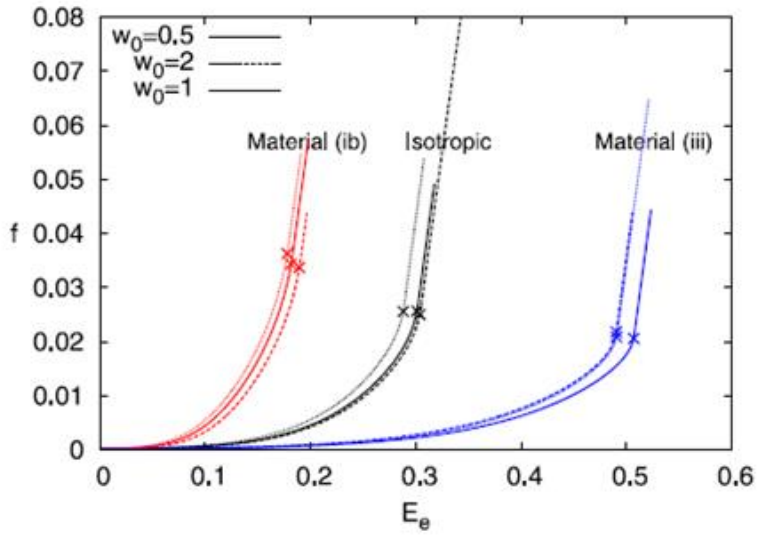

Figure 43: Void volume fraction versus strain for 3 material types with various void aspect ratios w_o **[85]**

A study analyzing the growth of voids in a ductile material in front of a crack tip was published [87]. This FEA-based study determined that (for an unspecified ductile material) voids located in the crack growth region grow dramatically, while voids not located in this region are not as affected. The void clusters were generated randomly. Furthermore the research group witnessed GNDs collecting at the crack tip, and were most dense at grain boundaries in this region.

One of the few FEA studies that incorporate grain orientation as a factor to strain response was conducted by Poterniche *et al.* [88], via the modeling of crystal plasticity through slip planes/direction interactions. Their simulations studied a single FCC crystal. Certain orientations of the crystal exhibited up to twice the growth rate of the voids. Additionally if the unit cell of the crystal were not aligned symmetrically or favorably with the applied tensile direction, then they experienced distorted crystal and void deformation (see Figure 44 and Figure 45). Their analysis on crystals with two voids demonstrate that coalescence effects diminish the influence of lattice orientation, however the lattice orientation does determine the type of shear bands that form between and around the voids. Under biaxial stress conditions the effect of lattice orientation on void growth, with the strain map produced being purely a factor of the type of loading conditions.

One research group [89] developed a crystal plasticity subroutine for Abaqus based on elasto-viscoplastic formulation determined Delannay *et al.* [90]. Void coalescence was developed in the subroutine via the Thomason criteria. The models simulated a BCC crystal with periodic boundary conditions. The results showed a heavy dependence of void growth rates on crystal orientation (with a factor of 2 found between orientations giving the lowest and highest growth rates). The Thomason criteria, although meant for isotropic materials, worked rather well in the prediction of void coalescence. The stress triaxiality also had a significant effect on the behavior of the crystal. Low stress triaxiality meant a heavy dependence of coalescence strain, void morphology and growth rate on the crystal orientation, while a high stress triaxiality only showed a dependence between the growth rate of voids and crystal orientation.

There have been a wide number of ways in which research groups have approached modeling crystal plasticity, including a novel method focused on dislocation-based crystal plasticity [91] (this model was created for materials with a FCC crystal structure and will not be detailed here). A user material (UMAT) subroutine has been designed by Y. Huang with the aim of incorporating single crystal plasticity into Abaqus [92]. While extensively used in ductile fracture-based research projects, this model assumes plastic dislocation occurs solely through slip, and does not take into account twinning or grain orientation. The model is based primarily on theories developed by Rice (Equations 15 and 16; [28] [71] [93]). Modification of this UMAT subroutine in order to incorporate other phenomena is possible; however most of the ductile fracture models presented in this chapter demonstrates a lack in accounting for twinning or grain orientation.

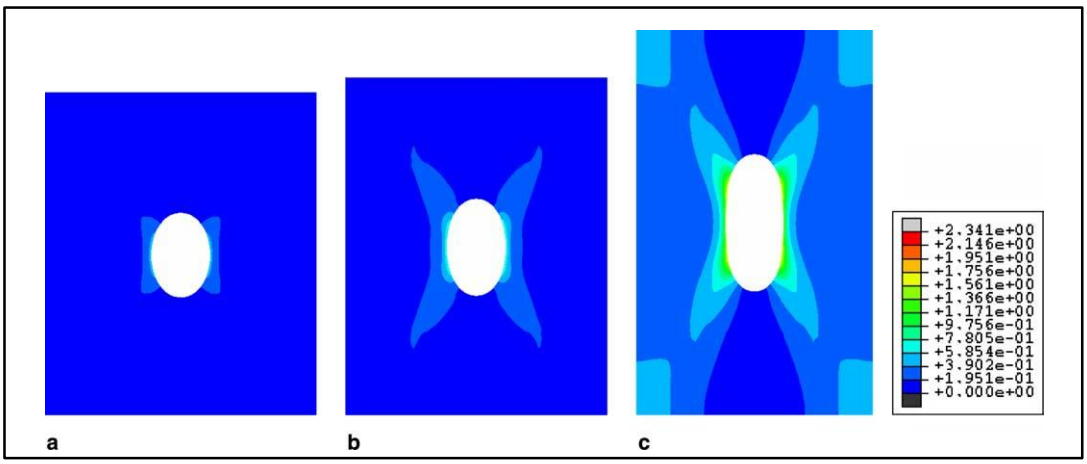

Figure 44: Contour strain plot for an FCC crystal with the [110] direction aligned with the tensile stress **[88]**

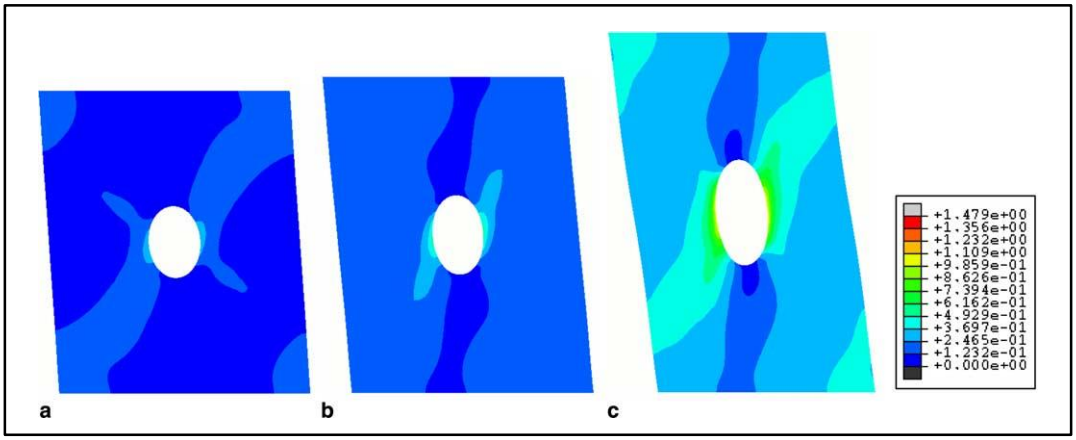

Figure 45: Contour strain plot for an FCC crystal with the [101] direction aligned with the tensile stress, in a non-symmetrical manner **[88]**

A research group based out of Spain has conducted molecular dynamics analysis on void growth in single crystals. Molecular dynamics (MD) can be said to be very similar to FEA with the primary difference being that MD takes into account the physical movement and positioning of individual atoms, as opposed to a predefined mesh. Based primarily on strain gradient plasticity formulation they conducted analysis on the size effect of voids in single crystals [94] and the effect of lattice orientation on void growth [95]. The simulation strategy utilized involved representing dislocations by a linear singularity that is directed perpendicular to the plane containing the Burgers vector. Based on this foundation the following equation was developed:

$$L_{nuc} = \frac{E\ b}{4\pi\tau_{nuc}(1-v)(1+v)} \quad \text{Eq. \{25\}}$$

where L_{nuc} is the distance between two new dislocations, E is the elastic modulus of the material, b is the Burgers vector, τ_{nuc} is the nucleation stress for a dislocation and v is Poisson's ratio for the material. Equation 25 was developed based on the discrete dislocation dynamics framework put forward by Van der Giessen *et al.* [96].

The former study [94] examined a single square crystal with a variable size (0.5 – 2.5 μm), containing a fixed value of void volume fraction (10%) that was deformed in biaxial and uniaxial tension. It was shown that the initial yield stress and work hardening rate increased as cell size decreased and stress triaxiality increased. This was primarily due to dislocation density increasing as cell size decreases, leading to higher work hardening rates and higher void nucleation stresses. These results are in line with strain gradient plasticity analysis.

The second study performed by this group [95] studied the ($\underline{1}$10) plane in an FCC single crystal. It was found that the crystals loaded under uniaxial tension in the [001] and [111] directions exhibited greater resistance to deformation and void growth rates than the crystals loaded in the [110] and [112] directions. This was shown to be the case since more active slip planes exhibit lower hardening and void growth rates. In the cases of uniaxial and biaxial deformation, crystal orientation did not influence the work hardening and growth rates. However the average hardening and growth under deformation parameters were higher than in the uniaxial tension case.

One research group developed a twinning model for HCP materials, particularly for application on zirconium alloys [97]. Their approach involved designating the twins formed as new grains with a different orientation within the polycrystal. Their aim was to see the effect of twins on the stress state within a grain. All stress components should relaxation upon twin formation, with the shear stress being more effected then the diagonal stresses. This is due to shear stresses being the driving force for twin formation. If shear stresses are high enough after twin nucleation, then propagation of the twin shall occur to further relieve the stress state. This model did not take into account the energy of the system at the twin boundaries, meaning the results are slightly underestimated.

2.4 Research Objectives

Based on the literature it is evident that effort has been made into understanding the ductile fracture process through the study of its constituent stages (void nucleation, growth and coalescence). However a common trend identified is the fact that the constitutive models proposed primarily focus on defining plasticity as a function of slip, with twinning, grain orientation and crystal structure effects being almost completely ignored. In order to gain a more complete understanding of ductile fracture it is important to study the effects of such phenomena on void growth and coalescence. Titanium retains the HCP crystal structure at room temperature, which causes it to have anisotropic mechanical properties. This metal is a prime candidate for plasticity studies primarily due to its high anisotropy, which in turn would cause the effects of twins and grain misorientations to heighten; not to mention its extensive usage in the aerospace industry.

This project will conduct two-dimensional studies into the effects of twins and grain orientations on void growth and coalescence in titanium. For example, would a growing void grow into a twin or be hindered by it? How does the growth rate of voids correspond to twin density? How will grain orientation affect the shape evolution and linkage of voids?

This will primarily be done through tensile tests aided with optical microscopy (void growth/coalescence analysis, twin and slip band evolution), EBSD (texture evolution effects on ductility) and DIC (strain path evolution with void growth and coalescence). Abaqus FEA simulations will also be incorporated to determine the effectiveness of various constitutive equations and experimental procedures.

Chapter 3: Materials and Experimental Details

The experimental flow is listed below:

1. Machining of samples
2. Primary polishing stage
3. Heat treatment
4. Vibratory polishing
5. Creation of fiduciary marks
6. Electron backscatter diffraction
7. Machining of voids
8. Third polishing stage
9. Deposition of digital image correlation pattern
10. Conducting tensile tests in-situ on select samples
11. Processing of results/data
12. Finite element modeling with subroutines

The next few subsections will initially discuss the selection of materials for analysis, followed by sample preparation details (design and polishing procedure), heat treatment details, microscopy methods, testing methodology, data analysis and finishing up with explaining the FEM subroutine.

3.1 Material Selection

For the purpose of this project titanium was selected for analysis over other HCP materials (such as zinc or magnesium) particularly due to its widespread use in the industry. Titanium maintains highly anisotropic properties making it relatively easier to study directional effects. In order to make the titanium coupons upon on which tests were performed, titanium foil measuring 0.89mm thick and with 99.7% purity was purchased from Alfa Aesar [98]. This classifies it as commercially pure grade 1 titanium (see Table 2, page 4).

Ideally a thin foil would have been utilized (less than or equal to 0.1mm). The issue with this approach is that, due to the inherent anisotropy of the material in question, it would be hard to promote failure at the center of the sample. Due to grains of certain orientations (soft

grains) thinning out faster than grains of the hard orientation failure could occur at any of these soft spots. In order to overcome this, a thick sample is utilized so that the soft grains are constrained by the bulk material, allowing them to thin down while also preventing failure within these grains.

3.2 Sample Preparation

3.1.1 Design and machining of tensile coupons

The proposed sample design is shown in Figure 46. The sample measures 40 mm long (from end to end) and 5 mm wide at the ends of the sample. The gage is 9 mm long with a curved gradient, measuring 3 mm at the widest section and 2.4 mm at the thinnest section (located at the center of the sample). The gage is sandwiched by fillets of radius 1 mm. The curved gradient was utilized in order to promote failure at the center of the sample without inducing stress concentrations within the gage length (by machining sharp edges or notches). The rather long grip sections are designed so that they may fit within the grips of the tensile machine.

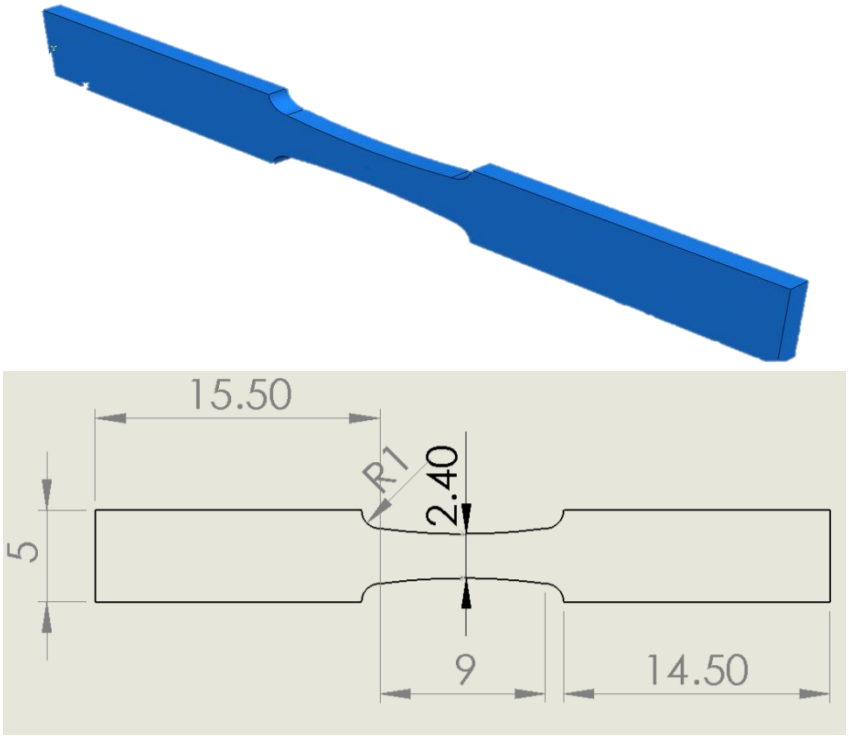

Figure 46: CAE model and drawing of the tensile sample to be utilized in experiments

The sample was machined via a CNC (computer numerical control) machine tool based on the model shown in Figure 46. An example of the final machined tensile sample is shown in Figure 47.

Figure 47: Machined titanium tensile sample

3.1.2 Grinding and polishing

The samples are polished in order to allow for electron backscatter diffraction (EBSD) analysis. Titanium is a notoriously difficult sample to polish for EBSD due to its sensitivity to plastic deformation. Improper polishing procedures may produce a very polished and clear optical microscope image, but will leave behind a surface layer dense with dislocations due to plastic deformation. Any dislocations at the surface or subsurface of the sample may interfere with the creation of the EBSD maps, giving erroneous or even no results at all.

After much trial and error two procedures were shown to have produced satisfactory results, which are detailed in Table 6. These procedures were developed based on research by Voort *et al*. [99]. The principal researcher in this study (George Vander Voort) is very commonly cited when it comes to metallographic preparation of materials.

Since the samples were prepared by hand, low pressure was applied during grinding and polishing (just barely enough to keep the sample from falling off the rotating disc base). Additionally the sample motion was contra to the rotation of the spinning base (the base was spinning counter-clockwise, so the sample was tracked along the surface in a clockwise motion). It is important to clean the sample between each stage of polishing via an ultrasonic bath.

Both procedures worked with respect to the EBSD pattern produced; however Procedure A produced a slightly better output than Procedure B. The indexed area in the first procedure reached 91%, while the second procedure had an indexed area of 81% (see Figure 48). An example of a polished specimen is shown in Figure 49. The polishing apparatus used in this project is shown in Figure 50.

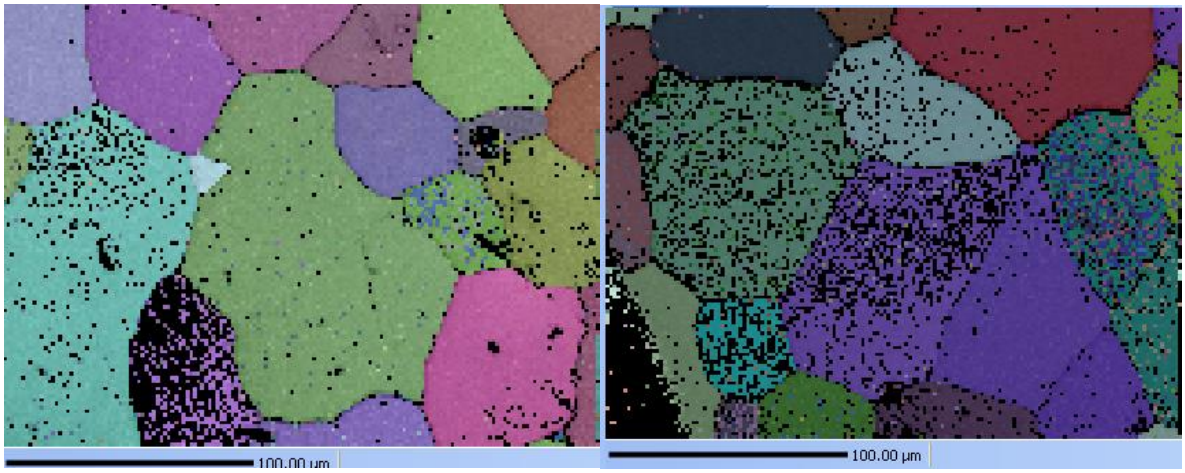

Figure 48: EBSD maps for samples polished with different procedures, indexed area is 91% (left) and 81% (right)

Table 6: Summary of the two polishing procedures developed

Type of cloth	**Grit size/ polishing suspension**	**Polishing time**	**Polishing machine RPM**
Procedure A			
Silicon carbide (SiC) sheet/sandpaper	P1200	Until sample is plane	200 – 250
	P2400		
	P4000		
MicroCloth pad	0.05 micron colloidal silica + 30% H_2O_2 (6:1 ratio)	10 minutes	100 – 150
Procedure B			
Sandpaper	P1200	Until sample is plane	200 – 250
MD-Mol silk cloth	9 µm diamond paste	10 minutes	100-150
MD-Chem cloth	0.05 micron colloidal silica + 30% H_2O_2 (6:1 ratio)	10 minutes	100 – 150

Figure 49: A polished titanium tensile specimen; note the shiny and reflective surface

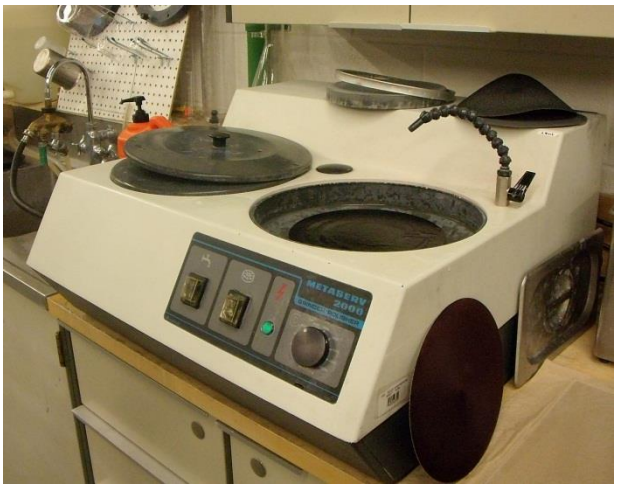

Figure 50: The Buehler Metaserv 2000 polishing apparatus used in this project

After polishing the sample is heat treated to allow for recrystallization and grain growth (details in the next subsection). The heat treatment may cause the sample to retain a surface height differential, which may interfere with EBSD analysis. Hence the sample is put into a vibratory polisher for 2.5 hours with a solution of 50% colloidal silica and 50% distilled water. An RPM of 6 to 8 must be maintained. This will remove any surface plastic damage and increase the flatness of the sample surface. A Buehler Vibromet 2 is used for this purpose and is shown in Figure 51. The polishing surface used is cloth based and must be changed upon any sign of damage. Additionally to prevent any cross contamination the cloth should be reserved for use with one material only (in this case, titanium).

Figure 51: Buehler Vibromet 2 vibratory polisher

3.3 Heat Treatment

The tensile samples are heat treated to promote grain growth and recovery within the material. This is done after the initial grinding and polishing stage to ensure extensive removal of defects and dislocations that arise as a result of grinding and polishing. A picture of the vacuum furnace set-up is shown in Figure 52.

The heat treatment is conducted in vacuum to prevent over-oxidation of the material. The vacuum is powered by a vacuum pump-diffusion pump combo that typically reaches 10^{-7} Torr (approximately 10^{-4} Pa).

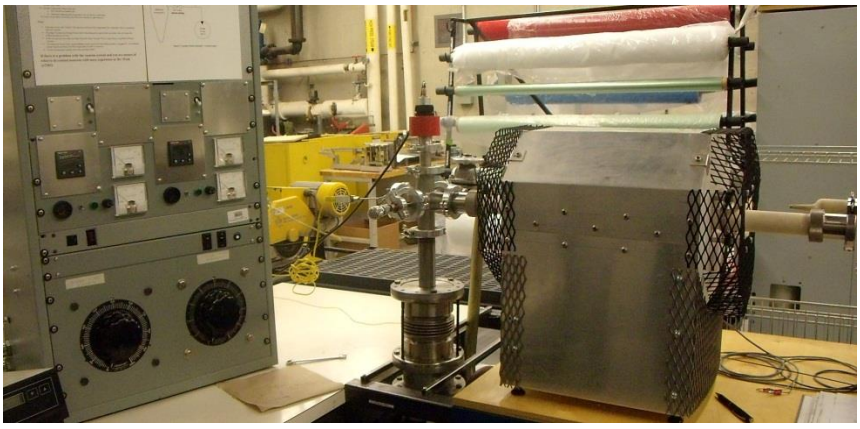

Figure 52: Vacuum furnace set-up; the furnace chamber is on the right and the controller is on the left

The heat treatment is done in two stages. The first stage is at 600°C for 60 minutes. The purpose of this is twofold: to allow for the specimens to achieve recrystallization and to allow for the stabilization of the vacuum at the high temperatures. After this stage the temperature in the furnace is elevated to 850° C for 5 hours to allow for grain growth. The heating profile is shown in Figure 54. In the literature review it was mentioned that grain growth rates over the α/β transition temperature (882°C) is higher than growth rates below that temperature. However samples heat-treated in the β-phase (1000°C) exhibited extremely brittle behavior, impacting the extent of our studies on ductile fracture. This was due to the formation of platelets and a martensitic microstructure (see Figure 53), arising due to the presence of the second phase (BCC β-Ti). It is also possible that stray oxygen molecules are absorbed by the titanium coupons during the heat treatment process, as titanium is very susceptible to oxygen absorption at elevated temperatures [1].

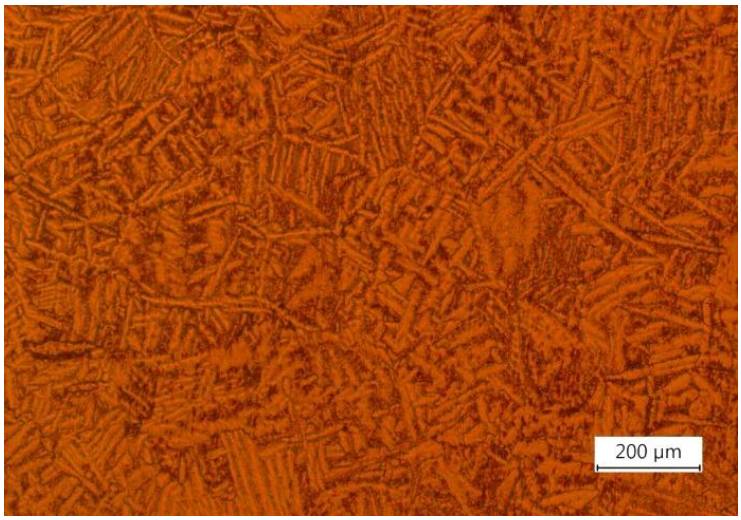

Figure 53: Titanium microstructure after heat-treatment at 1000 ^{0}C

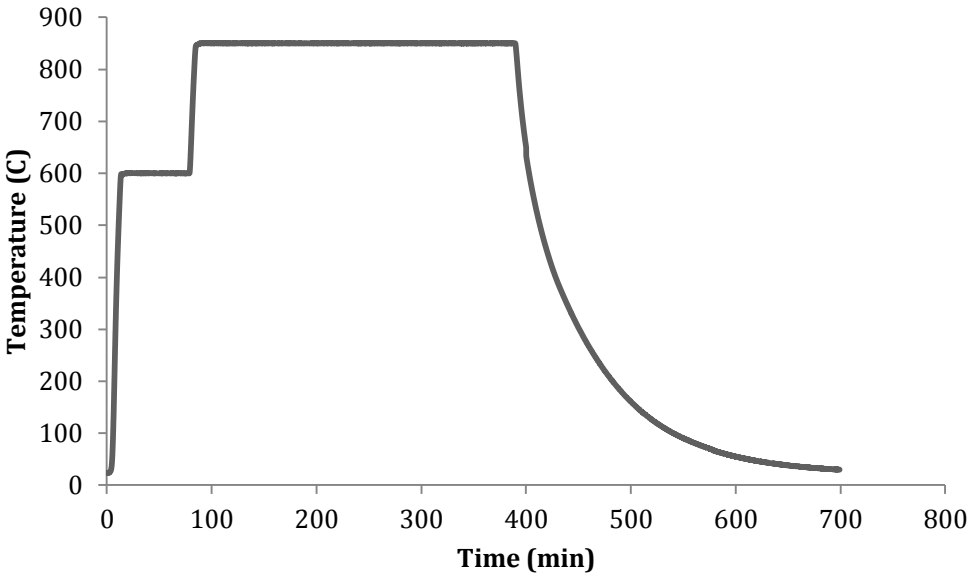

Figure 54: Temperature-time graph showcasing the typical heat-treatment conducted on the tensile samples

The heat treatment is a required stage of the sample preparation process since there is a lower limit to the size of voids that can be machined within a grain, as at least two voids are needed within a grain to study void growth and coalescence. Ideally the voids need to be spaced far enough apart so that they do not affect each other's growth, and at the same time they need to be far enough from the edges of the grain to prevent any transversal constraining effects. The average grain size post heat treatment is 75 μm (see Figure 55).

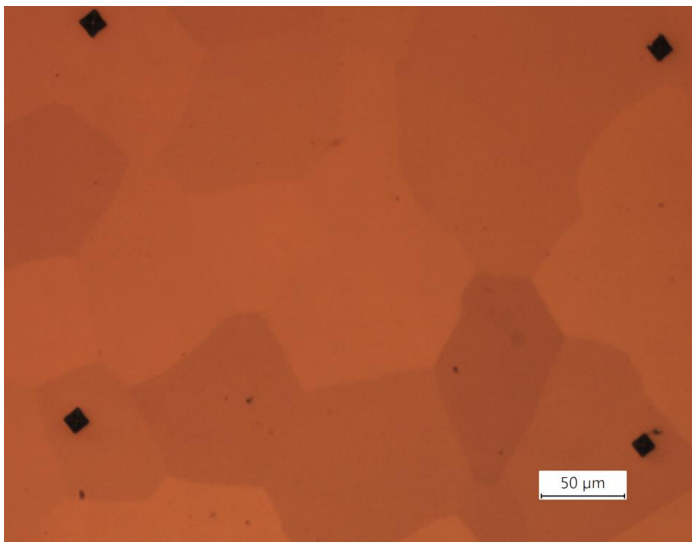

Figure 55: Optical micrograph of a titanium sample after heat treatment, shown under polarized light

3.4 Electron Backscatter Diffraction

Once the polishing and heat treatment are complete, the tensile sample should be ready for EBSD analysis. EBSD will create an orientation map for the specimen. An example of orientation map and diffraction pattern is shown in Figure 56. The center grain shown in the figure has an Euler orientation of {66.3°, 122.0°, 14.6°}.

Using a hardness indenter, four fiduciary marks were made on the surface of the sample. These would mark the four corners of a square, and exist to highlight the area within which EBSD analysis is to be conducted. The EBSD used a step size of 3.00 µm to scan the area bounded by the fiduciary marks (and some of the outer region), measuring 340 µm x 240 µm. The system itself consists of an EVO-MA10 SEM from Zeiss, outfitted with a NordLys Detector. The software used for data processing and acquision are HKL Fast Acquisition and HKL Channel 5 by OXFORD Instruments America Inc. The EBSD process was carried out by Dr. Mohammed Yandouzi, a research assistant within the department.

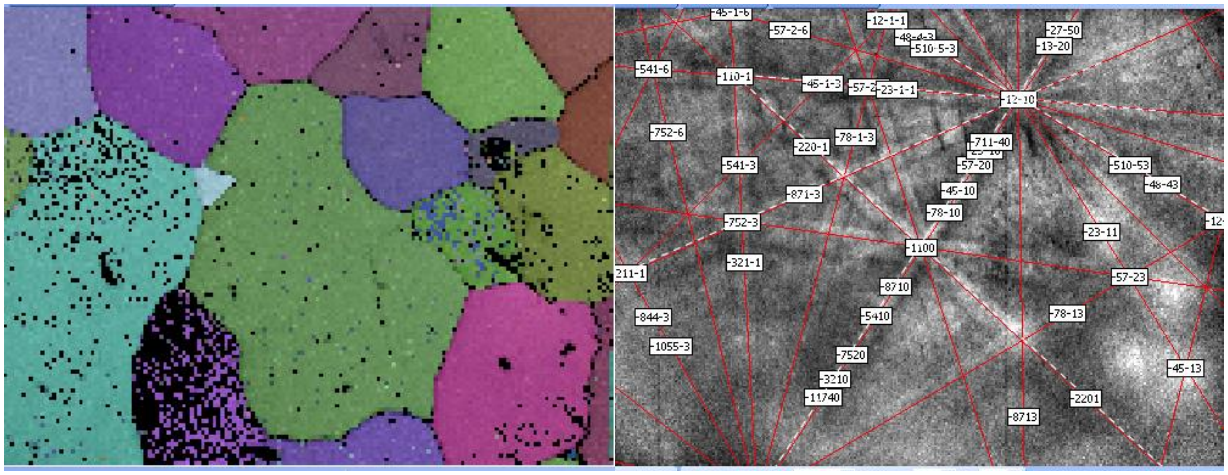

Figure 56: Euler-angle based color map of grains in a titanium sample (left); corresponding diffraction pattern (right)

3.5 Tensile Tests

Prior to conducting the tensile tests, voids must be machined into select grains using a femtosecond laser. After machining of the voids, a pattern for DIC (digital image correlation) must be deposited on the sample in order to track the localized strain development during tension.

3.5.1 Laser Machining of Voids

Samples not utilized for hardness analysis can be machined with voids for studying their growth in-situ. The procedure includes an ultrafast (femtosecond) laser micro-machining system. Using a laser energy per pulse of 5 μJ and an exposure time of 50 seconds at a laser repetition rate of 1 kHz, a void 13 μm in diameter and approximately 100 μm in depth can be machined (see Figure 57). Using the orientation maps we can choose the exact grains we would like to machine voids in. If more than one void will be machined in a grain, it will be done so that they lay μm away from each other (measured edge-to-edge). This is also to ensure that enough growth is witnessed prior to coalescence. The voids need to be at least 20 μm away from the grain boundary too to prevent any limiting effects on growth. This adds up to having grains at least 80 μm in width, showing the need for the heat treatment.

The issue is that there is a surface affected zone around the void, as shown in Figure 57below. This region can and will interfere with optical microscope imaging and consequentially, DIC results. In order to rectify this grinding and polishing should be conducted after the machining of voids.

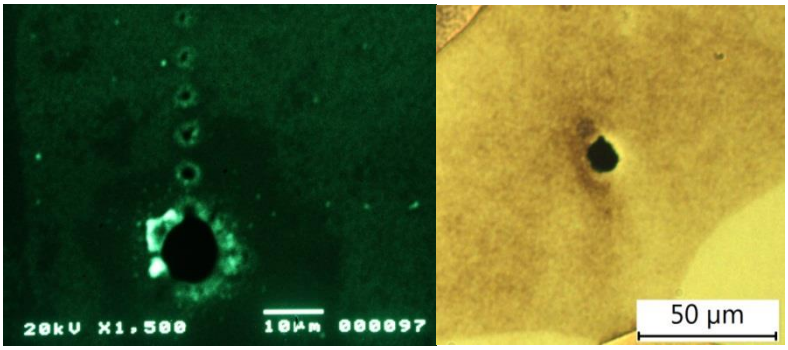

Figure 57: Void machined at a laser energy of 20 mJ for 5 seconds, before (left) and after (right) grinding and polishing

3.5.2 Electrodeposition of Digital Image Correlation (DIC) pattern

In order to conduct stain path analysis on the tensile coupons, a random speckle pattern must be created on the sample surface. This is typically done via electrodeposition (although other processes have been known to be used). For the purposes of this project copper deposition was conducted with an electrolyte containing the following:

- Copper sulfate - 40 g/L $CuSO_4 \cdot 5H_2O$
- Sulfuric acid - 10 g/L H_2SO_4

- Polyethylene glycol – 300 ppm PEG

Electrodeposition of copper particles occurs in 3 stages: particle nucleation, growth and coalescence. In order to retain a good DIC pattern, emphasis needs to be placed on the nucleation of particles. However due to titanium's sensitivity to deposition of copper, the time frame where nucleation occurs is very small leading to very rapid growth of deposits. Our initial electrodeposition set-up involved a simple power supply connected directly to the anode (a copper bar) and the cathode (the sample to be coated), immersed in a basic copper sulfate solution and manually controlling the deposition time and voltage. This proved problematic since an appropriate combination of deposit size and density was not achievable.

According to Emekli *et al.* [100] utilizing PEG in a copper sulfate electrolyte allows for smaller and denser copper nucleates. It is thought that the PEG acts as a suppressor, primarily through hindering the surface growth of particles and increasing the overpotential of the circuit. The addition of PEG proved to be a useful tactic, in that the deposit pattern on the titanium surface was better, however further improvements were required in order to achieve an ideal DIC pattern.

Pulsed electrodeposition is commonly used to create nano-grained materials. By having the current in the circuit turn on and off in preprogrammed pulses, one can place emphasis on the nucleation of particles versus growth/coalescence. Using this approach the voltage (or current density) can be used to control the density of deposits, while short pulses can control the size of deposits. A schematic of the set-up used is shown in Figure 58.

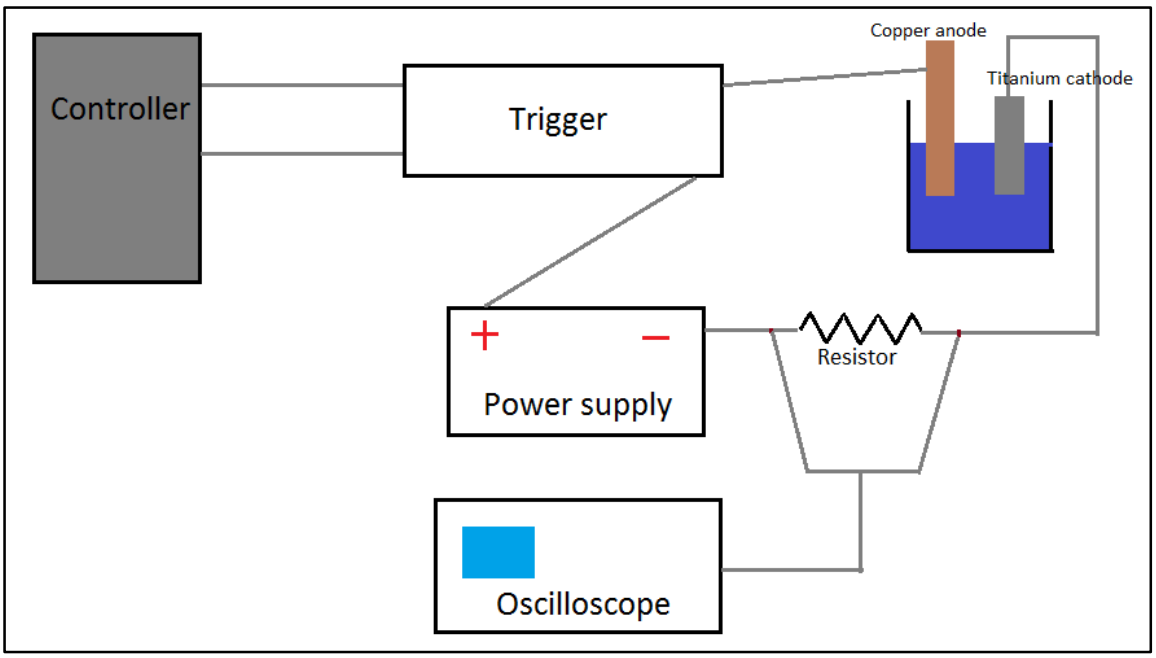

Figure 58: Schematic of the pulsed electrodeposition set-up

An interesting effect that comes about when depositing copper on titanium is preferential deposition dependent on grain orientation; that is certain grain orientations of titanium will see higher deposition rates than other orientations. A picture of a sample of titanium showcasing such a phenomenon is shown in Figure 59. The lighter colored grains around the center of the picture have a lower density of copper particles on their surface (the grain at the bottom right has very little to no deposition), while the grains at the top and right side of the figure are almost completely coated with copper. This is explained by Davepon *et la.* [101] as due to different grains having different densities of surface atoms, changing the effects of directional electrochemical reactions. As the current during electrodeposition flows past the surface of different grains, different interactions occur based on the surface density of atoms.

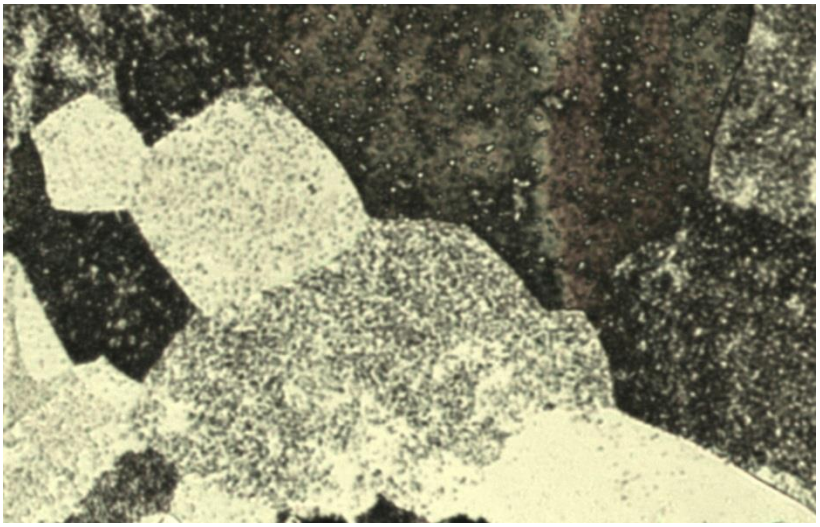

Figure 59: Optical micrograph of titanium showing preferential deposition of copper depending on grain orientation

This obviously poses a problem for DIC as all grains will need to be coated with a sufficient size and density of copper particles. However pulsed deposition seems to rectify this error, since the focus on nucleation of particles seems to prevent grains from coming out of the deposition process with little or no copper particles (although the grains do witness different densities of copper deposits; see Figure 60).

The procedure settled upon for deposition is 15 pulses with an on-time of 10 ms and an off-time of 200 ms, with an applied voltage of 10 volts.

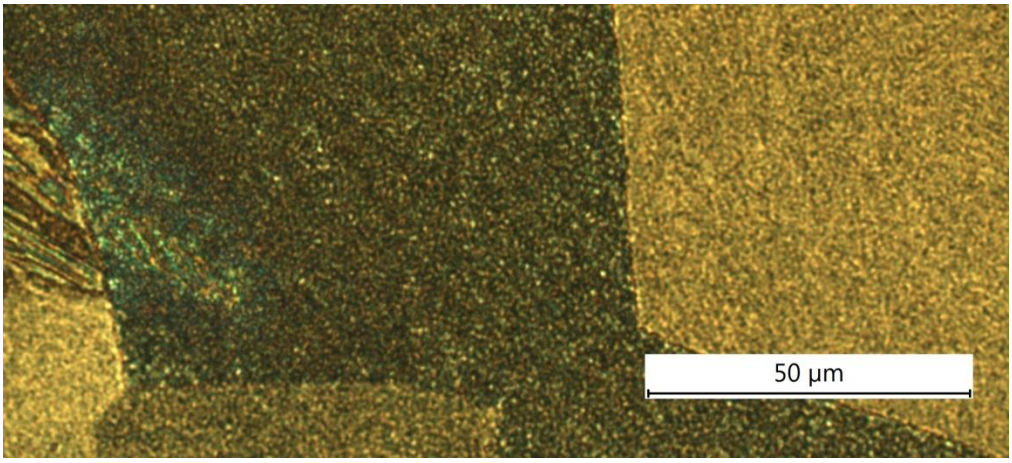

Figure 60: Copper deposits on polished titanium via pulsed electrodeposition

3.5.3 Tensile Tests

Once a good DIC pattern has been deposited on the titanium samples, the tensile test can be conducted. The tensile machine used is shown in Figure 61 and is controlled via a MATLAB-based GUI. When running the test, the tensile machine is placed under a Nikon Optiphot 100 microscope using a 20x ULWD (ultra-long working distance) objective, connected to a Pixelink camera. The camera interfaces with proprietary software to take snapshots of the sample every 0.5 seconds (this value can be adjusted).

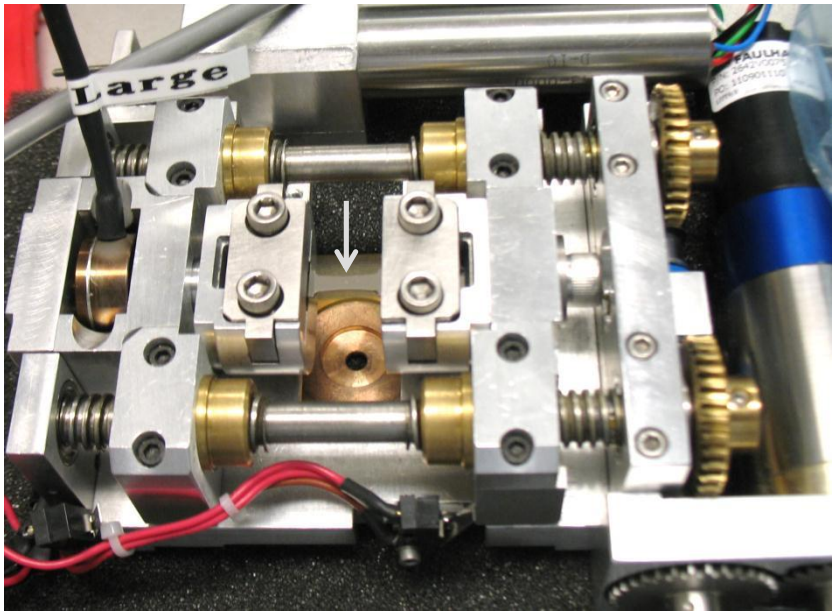

Figure 61: Picture of tensile machine used in this project; the width of the tensile sample in the grips is 2.4 mm (marked by the white arrow)

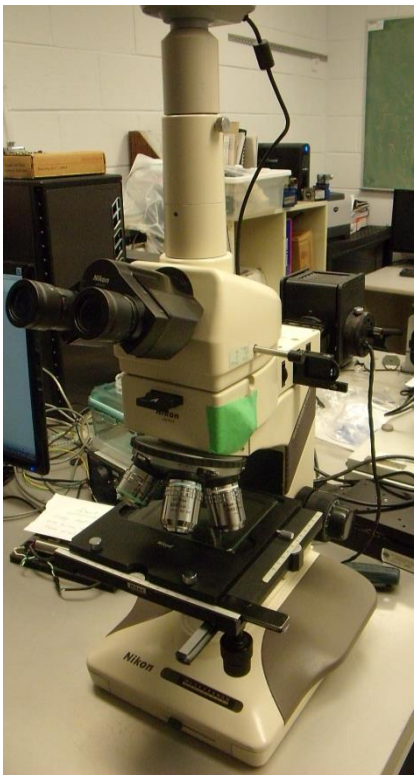

Figure 62: Nikon Optiphot 100 microscope used during tensile tests

The tensile test is run at a crosshead grip speed of approximately 2.7 μm/s, which translates to a strain rate of 6 x 10^{-5}/s, categorizing the tests as near-quasistatic.

3.6 Analysis and Processing of Data

Two primary sets of data are required for each tensile sample: void growth information and local strain information.

Initial plans were to use the ImageJ software to automatically measure the major and minor diameters of our voids through batch processing. Using the threshold limiting plug in one could isolate certain regions of an image through pixel intensity filtering (example shown in Figure 63). However due to the extensive surface deformation that occurs, the software would not be able to differentiate between voids and highly deformed regions. In the end we opted for manually measuring the void dimensions at 10 different points during the tensile test.

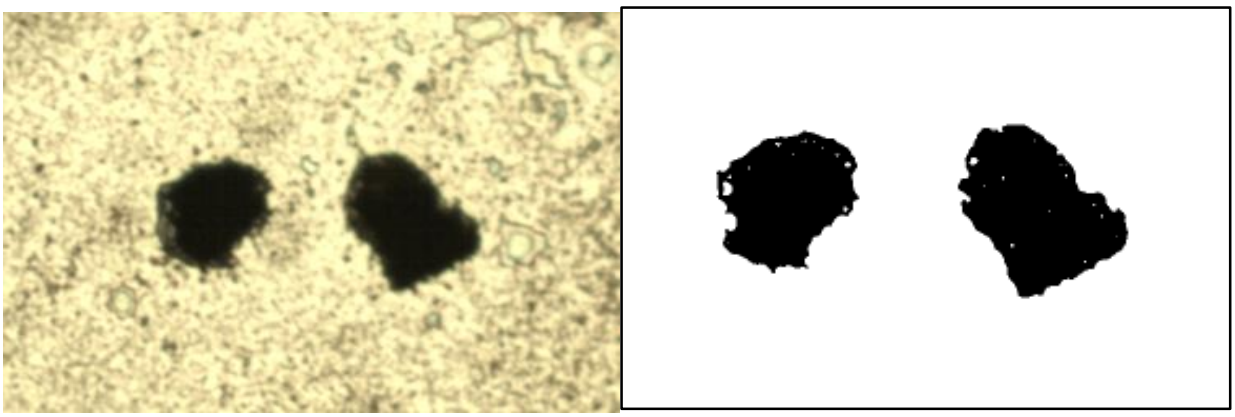

Figure 63: A micrograph of two voids in a sample before and after threshold limit application via ImageJ; note that typically the voids formed in the tensile coupons are circular, not an irregular shape

For retaining the strain path and evolution information from the tensile test, the output images are processed with the proprietary DaVis software. Using the strain module in the program, images can be selected for strain analysis. The software will be able to track the features on the surface to produce a strain map. The software can output this strain map in a number of ways (images, videos, plots, etc.). In terms of software parameters, 3 seeding points were chosen with one being close to the voids (seeding points are the points where the deformation calculations initiate). Window and step lengths were kept around 100 pixels and 15 pixels respectively.

3.7 Finite Element Modeling: Crystal Plasticity Subroutine

To conduct simulations for this research project a subroutine developed by Dr. Javier Segurado (Department of Materials Science, Polytechnic University of Madrid) was used. This subroutine incorporates the effects of crystal plasticity into FEM simulations. What follows is an explanation of the approach taken to model crystal plasticity, along with the inputs required and output generated by the subroutine. Most of the information below has been taken from the subroutine FAQ provided by Dr. Segurado and the book *Crystal Plasticity Finite Element Methods* by Roters *et al.* [102].

The deformation gradient vector $\boldsymbol{F}$ is broken down into two components: elastic deformation and plastic deformation, represented by $\boldsymbol{F}^e$ and $\boldsymbol{F}^p$ respectively. This is represented by the equation:

$$\boldsymbol{F} = \boldsymbol{F}^e \boldsymbol{F}^p \quad \text{Eq. \{26\}}$$

The velocity gradient is defined as the change in relative velocity between parallel planes throughout the depth of the material. Typically represented by $\nabla \boldsymbol{v}$, we will utilise the term $\boldsymbol{L}$ for brevity. This term is defined mathematically as:

$$\boldsymbol{L} = \dot{\boldsymbol{F}} \boldsymbol{F}^{-1} \quad \text{Eq. \{27\}}$$

where $\dot{\boldsymbol{F}}$ is the time derivative (or time-dependent change) of the deformation field, and $\boldsymbol{F}^{-1}$ is the deformation gradient's inverse. By substituting Equation 26 in the above and simplifying, one can derive an expression that contains the elastic and plastic components of the velocity gradient:

$$\boldsymbol{L} = \boldsymbol{L}^e + \boldsymbol{F}^e \boldsymbol{L}^p \boldsymbol{F}^{e-1} \quad \text{Eq. \{28\}}$$

According to Von Mises [31] and Taylor [32] at least 5 slip systems need to be activated in order for ductile fracture to occur. If we were to take the assumption of Rice [103] that dislocation slip is the sole deformation process, then the plastic velocity gradient can be written in terms of the shear rate:

$$\boldsymbol{L^p} = \sum_{\alpha=1}^{N} \dot{\gamma}^{\alpha} (\boldsymbol{s}^{\alpha} \otimes \boldsymbol{n}^{\alpha}) \quad \text{Eq. \{29\}}$$

where $\dot{\gamma}^{\alpha}$ is the shear rate on slip system α, with s^{α} and n^{α} acting as the unit vectors in the slip direction and the normal to the slip plane. N is the number of active slip systems. The $\otimes$ symbol represents a tensor product.

The shear rate can be formulated by resolving the shear stresses on each system and knowing their respective critically resolved shear stresses. A suggested formulation for the shear rate in FCC crystals for a slip system α is [103] [104] [105] [106]:

$$\dot{\gamma}^{\alpha} = \dot{\gamma}_0 \left| \frac{\tau^{\alpha}}{\tau^{\alpha}_{crss}} \right|^{\frac{1}{m}} sgn(\tau^{\alpha}) \quad \text{Eq. \{30\}}$$

where $\dot{\gamma}_0$ is the reference shear rate, τ^α is the shear stress resolved onto the α slip system, τ^α_{crss} is the critically resolved shear stress for the slip system and *m* is the rate sensitivity of slip. The *sgn(x)* function simply extracts the sign (positive or negative) of the real number *x*.

The Kirchhoff stress is defined as the product of the Koche stress tensor and the jacobian (which is essentially the strain energy release rate around a crack tip or void) [107]. By projecting the Kirchhoff stress onto the slip system, one can determine the shear stress τ^α in Equation 30. This can be summarily defined as:

$$\tau^\alpha = \mathsf{C}\left[(\boldsymbol{F}^{eT}\boldsymbol{F}^{e})^{1/2} - \boldsymbol{I}\right] \cdot (\boldsymbol{s}^\alpha \otimes \boldsymbol{n}^\alpha) \qquad \text{Eq. \{31\}}$$

where C is the elastic stiffness tensor of the material, $\boldsymbol{F}^{eT}$ is the transverse of the elastic deformation gradient and $\boldsymbol{I}$ is the identity matrix.

The critically resolved shear stress can be determined using the model suggested by Asaro and Needleman [108]:

$$\dot{\tau}^\alpha_{crss} = \sum_{\beta=1}^{N} q_{\alpha\beta}\, h(\Gamma)\, \dot{\gamma}_\beta \qquad \text{Eq. \{32\}}$$

where α and β are the slip systems, and $q_{\alpha\beta}$ is the latent-hardening coefficient between those respective slip systems. In the special case α = β then q would be the self-hardening coefficient. $h(\Gamma)$ is the hardening modulus as a function of the accumulated shear strain and can be determined either by the Asaro-Needleman hardening law [108] or the Voce model (as adapted by Tomé *et al.* [109]), shown below in Equations 33 and 34 respectively:

$$h(\Gamma) = h_0 \operatorname{sech}\left|\frac{h_0\Gamma}{\tau_s - \tau_0}\right|^2 \qquad \text{Eq. \{33\}}$$

$$h(\Gamma) = h_0 + \left(h_0 - h_1 + \frac{h_0 h_1}{\tau_s}\Gamma\right) e^{-h_0\Gamma/\tau_s} \qquad \text{Eq. \{34\}}$$

where h_0 is the initial hardening modulus, h_1 is the final hardening modulus, τ_0 is the initial yield shear stress and τ_s is the saturated yield stress (and should always be taken as

positive). In order to determine the accumulated shear strain Γ, a simple integral of the shear strain rate can be used:

$$\Gamma = \int_0^t \sum_{\alpha=1}^{N} \dot{\gamma}^{\alpha} \, dt \qquad \text{Eq. \{35\}}$$

For our purposes the Voce model (Equation 34) will be utilized over the Asaro-Needleman model (Equation 33).

There are specific inputs that the subroutine requires to run. The standard material properties Abaqus uses are not required (typically elastic modulus, Poissons ratio, yield stresses and corresponding plastic strains). Instead a file with the properties of the material being simulated is linked to the subroutine. This property file contains the following information:

- The elastic stiffness tensor; since titanium is an orthotropic material there will be 6 values here (see Table 7)
- The values of $\dot{\gamma}_0$ and m in Equation 30; taken to be 1 and 0.1 respectively. Note that the shear rate in this case is representative of the applied strain rate
- The number of slip systems, along with their respective Miller-Bravais notations in the *cubic* format, not the *hexagonal* format (i.e. represented by 3 indices, not 3)
- The hardening coefficients $q_{\alpha\beta}$ between slip systems; we will be assuming that there is no hardening effect between the slip systems, so all the coefficients will be equal to 1
- The Voce parameters in Equation 34 (τ_0, τ_s, h_0 and h_1) for each set of slip systems; these values were adjusted so that they fit the stress-strain curve for a sample of titanium that has been heat-treated and contains no voids. The methodology used to obtain these parameters are explained in Chapter 5, along with the parameters themselves.
- A few internal parameters that control iterations of model discretization, and whether implicit or explicit calculation of hardening must be carried out

Table 7: Elastic stiffness properties used for titanium; all values are in GPa and taken from **[42]**

C_{11}	C_{12}	C_{44}	C_{13}	C_{33}	C_{66}
162.4	92	117	69	180.7	35.2

The main model-specific parameter required is the grain orientation(s) of the sample, which is provided instead of the Abaqus' standard plasticity material properties. Each grain's orientation is defined by providing the subroutine with the vectors that represent its [100] and [001] directions, with respective to the global system axis.

Chapter 4: Experimental Results

This section deals with detailing the results of experimental work, along with ancillary and relevant information

4.1 Tensile Machine Rigidity Factor

Most of the parts of the tensile machine are constructed from pure aluminum, so when conducting a test on a material that is stronger than aluminum the tensile machine frame would elastically deform significantly. This deformation will skew the displacement/strain results of the test slightly. This can be verified by checking for the measured elastic modulus from a tensile test versus the expected elastic modulus of the material. By applying a rigidity factor it is possible to correct these distorted values.

The rigidity factor is calculated simply by taking macroscale photos in-situ during a tensile test, the field of vision being large enough to see the entire sample. By measuring the change in a samples gauge length from the pictures, and comparing those values to the readings from the LVDT (linear variable differential transformer; used to measure the displacement of the tensile machine grips) the rigidity factor can be determined.

Tests for the rigidity factor were conducted on samples oriented along the transverse direction (TD) and rolling direction (RD). Since it was shown in the literature review that samples in these different orientations have different mechanical behavior, it would follow that they would require different rigidity factorsFigure 64 shows an example of the real and LVDT measurements of a TD sample. Two trendlines are drawn through the data points: a linear and a polynomial trend, with their respective equations displayed. Normally a linear factor would be required, but due to the shape of the data set the effect of an order 2 polynomial was investigated.

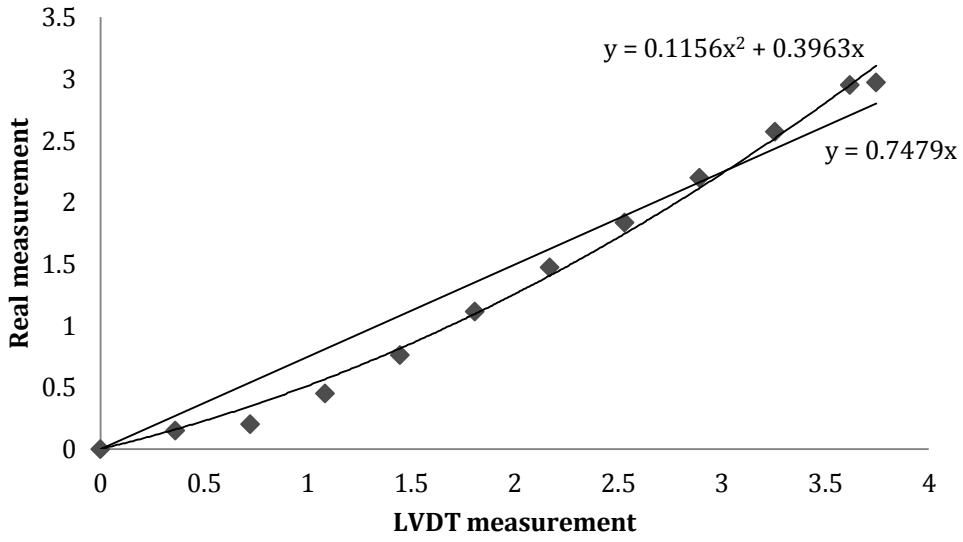

Figure 64: Real measured change in gauge length versus change measured by LVDT for a TD sample, with a linear and a polynomial trendline

From the figure it is evident that a polynomial factor fits the data better and would be more suitable. Figure 65 shows3 graphs: a stress-strain curve of a TD sample prior to the application of a rigidity factor, one with an applied linear factor of 0.7789, and the same data with an applied polynomial factor ($y = 0.1171x^2 + 0.4416x$).

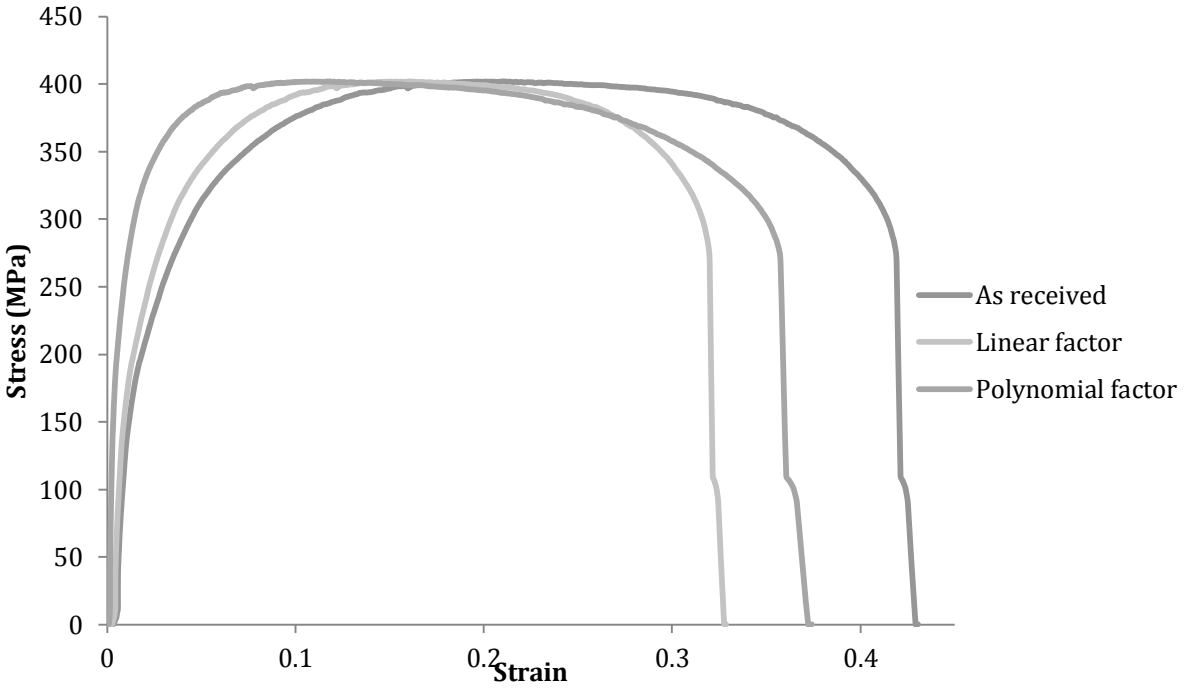

Figure 65: Stress-strain curve of a titanium sample with as received results, results with an applied linear factor and with a polynomial factor

Table 8 summarizes the rigidity factors obtained. In the end the polynomial factors were utilized since they better fit the data points and produced an elastic modulus closest to the expected value. Titanium has an elastic modulus of 110 GPa; the as-received stress-strain data had an elastic modulus of 42 GPa. With the application of the polynomial factor this value jumps to 86 GPa.

Table 8: Linear and polynomial rigidity factors for samples cut along the rolling and transverse directions

	Rolling direction (RD)	**Transverse direction (TD)**
Linear factor	$y = 0.8398x$	$y = 0.7789x$
Polynomial factor	$y = 0.0834x^2 + 0.603x$	$y = 0.1171x^2 + 0.4416x$

4.2 Texture and Grain Orientation Analysis

The sheets of titanium used in this study were allegedly hot-rolled (rolled into shape above the recrystallization temperature of the material). As such some texture bias would be expected prior to and after heat treatment. Post-heat treatment EBSD analysis was

conducted on all samples and all orientation information compiled in order to give us an idea of the orientation preferences for the material.

By plotting the three Euler angles {ϕ_1, Φ, ϕ_2} for all grains into a 3D scatter plot, one can create a graph called *Euler space* which visualizes any bias. Due to limitations in presenting the Euler space on paper, three 2D scatter plots follow that plot the Euler angles against each other (ϕ_1 vs. Φ, ϕ_1 vs. ϕ_2 and Φ vs. ϕ_2; see Figure 66). It can be seen that the first two Euler angles (ϕ_1 and Φ - *Phi1* and *Phi* respectively) localize at certain angles, while there is no pattern present for the last angle (ϕ_2 or *Phi2*). This can be explained by the way the angles are defined. Since the first and last angles both involve rotations about the *z*-axis, the latter would be dependent on the former. The preferred Euler angle biases are shown in Table 9. These values were received by visually locating where the angles localize then averaging out the values within a certain range.

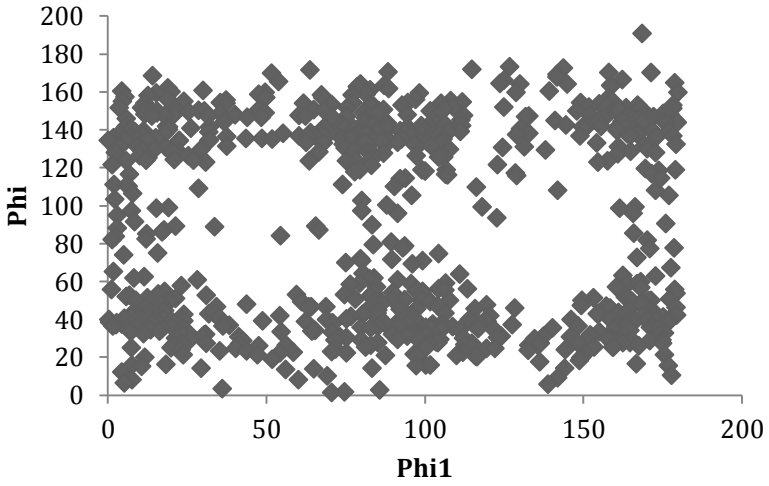

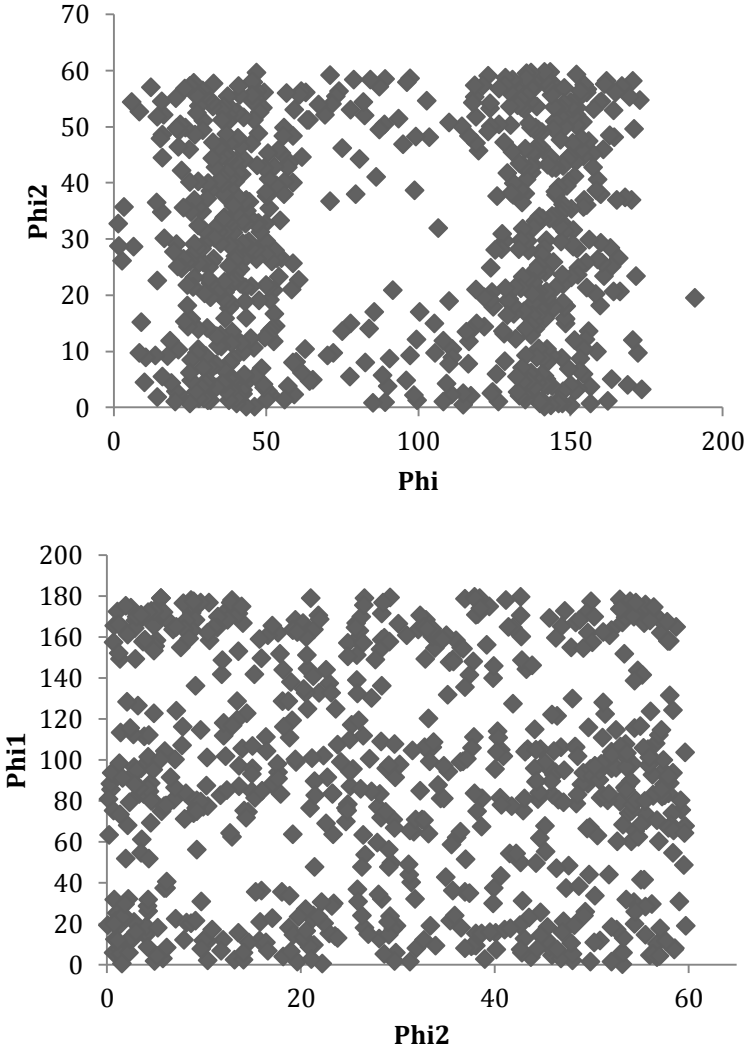

Figure 66: Plotting the three Euler angles against each other

Table 9: Preferred Euler angle orientations

Phi1 ϕ_1 (°)	**Phi Φ (°)**	**Phi2 ϕ_2 (°)**
9.3°	142.74°	-
84.67°	45.09°	-
165.32°	-	-

Pole figures were also created to see the preferred textures with respect to the HCP crystal directions/planes. Shown below in Figure 67 are the pole figures. The data was extracted from the EBSD maps using the VMap software (developed by Dr. John Humphreys at the Manchester Materials Science Center), then converted into heat/contour maps using

MATLAB. Doing this helps visualize where preferred orientations lie. It is evident that the [0001] poles have a preferred orientation along the tranverse direction, and the [10$\underline{1}$0] pole along the rolling direction (both slightly offset from the RD and TD directions). It should be noted that the [0001] pole figure is what was expected based on the literature, while the [10$\underline{1}$0] pole figure does not (see Figure 5 on page 5).

Using the ASTM E112-12 standards for grain size measurements [110], particularly the Heyn Linear Intercept Procedure, it was determined that the average grain size after heat-treatment is 71.86 μm.

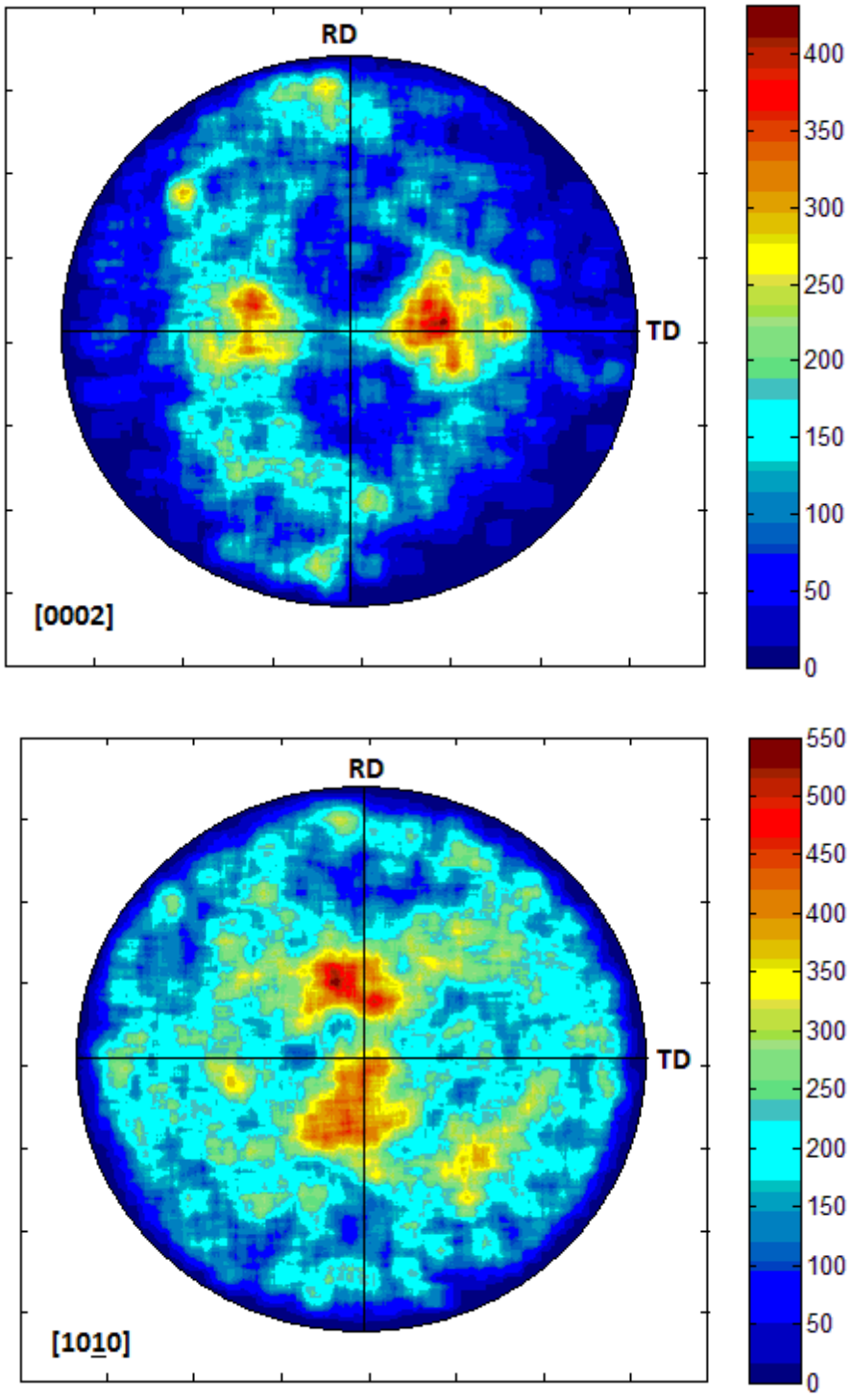

Figure 67: Pole figures for the [0002] and [10$\bar{1}$0] directions respectively, generated using cumulative data for all samples tested

4.3 Void Growth Analysis

A number of titanium coupons were machined with a single void in a preselected grain. The average void size was 13.4 µm (Figure 68). The main criteria in mind when selecting grains was that the orientations should cover a wide range, which was accomplished using the inverse pole figures. Figure 69 shows the orientations of grains analyzed for samples in the RD (rolling) and TD (tranverse) orientations. Samples are labeled from RD-1 to RD-9 along the rolling direction and TD-1 to TD-9 along the transverse direction. Euler angle data for the samples may be found in the appendix.

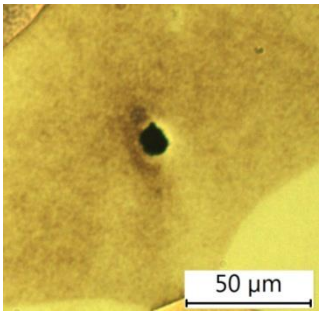

Figure 68: Void laser-machined into a grain in sample RD-3 and electrodeposited with copper, 20x magnification

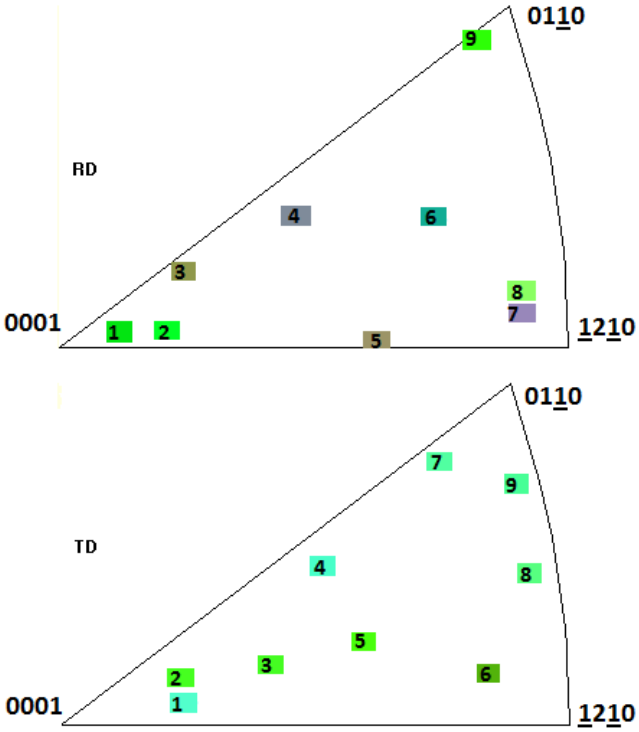

Figure 69: Inverse pole figures showing the range of orientations studied for RD and TD samples

Figure 70 shows the evolution of a void during a tensile test (more graphs may be found in the appendix). The sample in question is oriented parallel to the RD. The x-axis shows the strain over the entire sample and the y-axis shows the normalized change in major diameter (vertical length of void) $\Delta a/a_0$. Slip bands form throughout the grain typically at a 45° to the tensile direction, as the major diameter of the void increases and the minor diameter (horizontal length) of the void decreases. The dark patch that forms on the right-side of the void in the third image is a highly deformed area that cannot be appropriately visualized by an optical microscope. These deformed areas grow until they meet with the grain boundary, forming a path of high strain. Should this path meet with high strain regions in the surrounding grains then it becomes a potential location for crack formation and subsequent fracture. However since this process is highly dependent on crystal orientation and due to the small overall void volume fraction, final crack propagation need not necessarily pass through our grain with the void

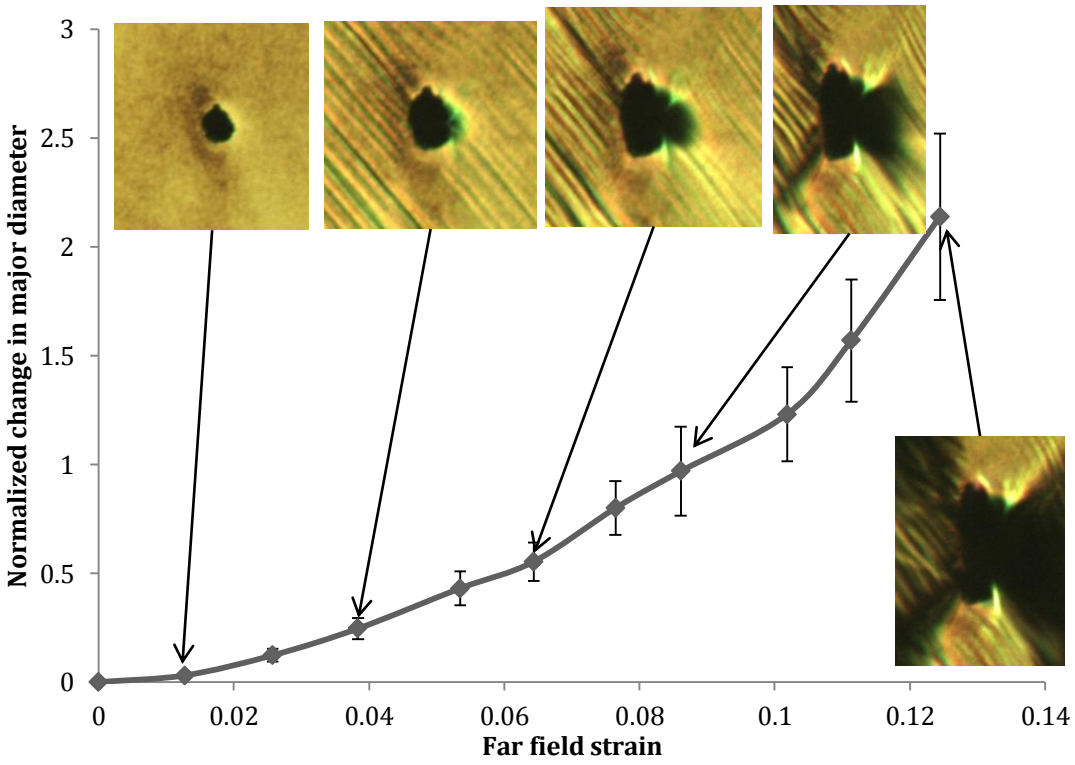

Figure 70: Graph showing the evolution of a void in sample RD-3 during a tensile test

The error bars in Figure 70 were calculated by magnifying each individual image and measuring the thickness of the void edge in pixels. This value was then converted into

microns using the scale bar. As the tensile test progresses the error in measurement increases since the sample gets more deformed, blurring the lines between the void interior and sample surface. This process is how all error bars for all samples were measured. It should be noted that minor diameter measurements saw larger errors due to extensive deformation that typically occurs on the left and right sides of the void.

Figure 71 shows an SEM image of the fracture surface of the sample RD-3 shown in Figure 68 and Figure 70. Near the bottom of the image you can see the interior surface of the void. Following this surface deeper into the material will lead to a globulous and bubbly texture at the tail end of the void that is the actually redeposited titanium. The remelted material is an artefact of the femtosecond laser machining process. When under exposure to the laser, material vaporizes at a rapid rate but then redeposits itself on the interior of the void surface when the laser pulses off, leading to the formation of this texture.

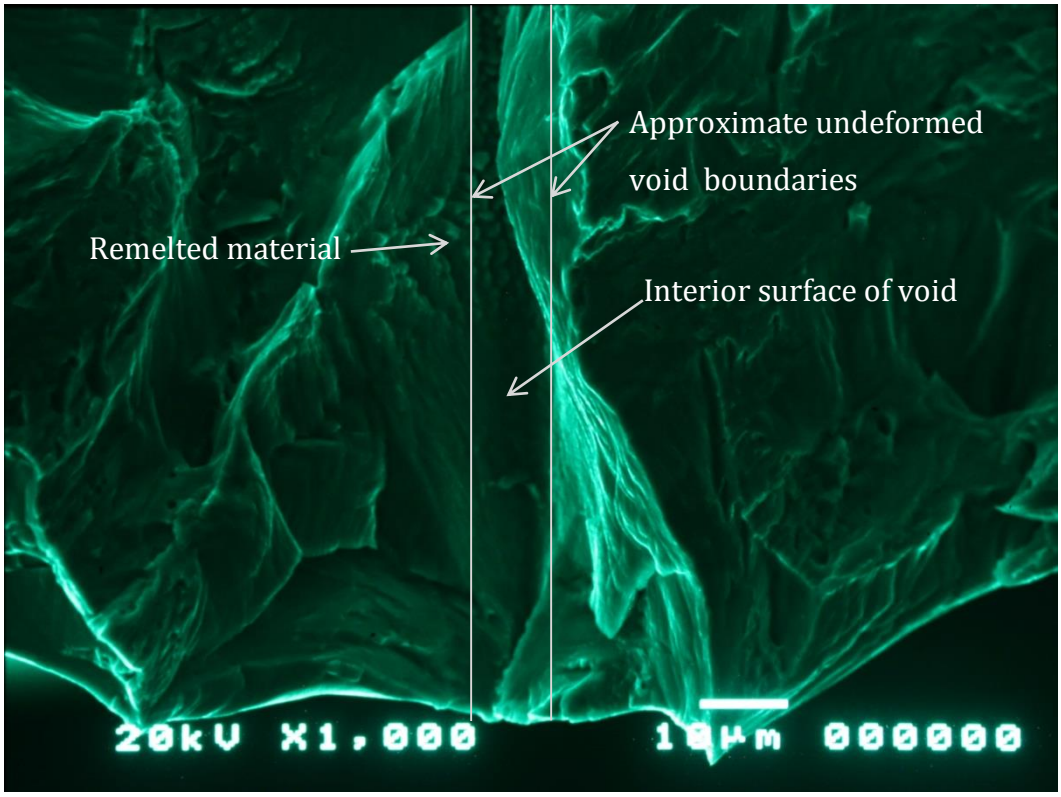

Figure 71: Fracture surface showing cross section of the void in sample RD-3; the redeposited material is apparent bubbly-type surface

4.3.1 Results of Major Diameter Measurements

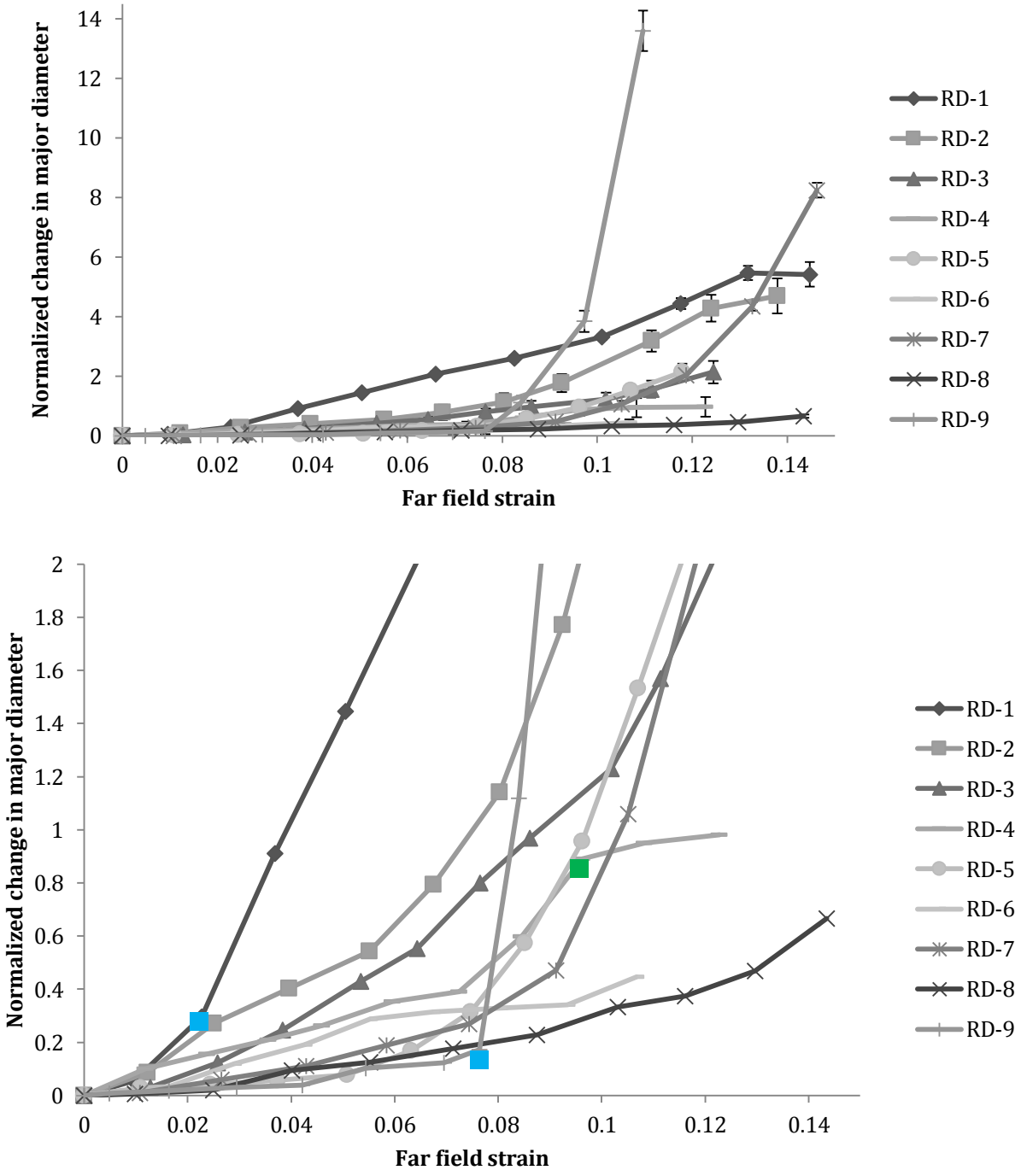

Figure 72: Normalized change in major diameter versus far field strain for RD samples, the first graph shows the entire data range and the second graph reduces the x and y axes range and removes the error bars to better see the results; the blue squares represent points where a crack propagates through the void (RD-1 and RD-6) and the green squares where cracks form elsewhere in the sample (RD-4)

Figure 72 shows the normalized change in major diameter for RD samples over the course of the tensile test. The graphs are generally semi-linear lines. A couple of the samples see sharp increases on the y-axis (such as RD-7 and RD-9). This is because cracks forming in other areas of the material meet with our void increasing its growth rate. Sample RD-1 has the highest void growth rate over the whole test. According to its position on the inverse pole figure (see Figure 69) it should portray the hardest properties of all the voids due to its proximity to the [0001] direction. In fact soon after the tensile test had begun, a crack had formed in the grain through the void as shown in Figure 73. The presence of slip bands shows that there was initially some ductile deformation, however this did not allow for fast enough stress relief in the grain leading to sudden and relatively rapid crack formation. Samples with soft grains such as RD-8 exhibit the lowest void growth rates since they absorb a lot of the strain.

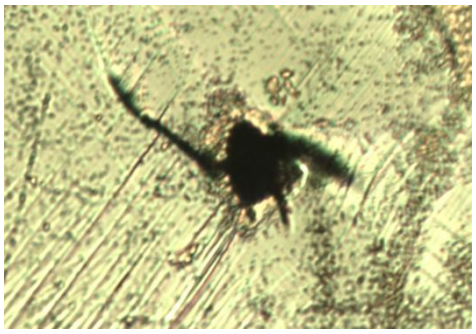

Figure 73: Crack forming through the void in sample RD-6, 20x magnification

Doing the same for the TD samples yields similar trends, as shown in Figure 74. Sample TD-5 shows little to no void growth. This is because cracks had formed in the grains above and below the grain containing the void, see Figure 75. The strain loaded on the sample was then prevented from reaching the void. It is not clear why these brittle cracks formed, though it is postulated to be due to oxygen diffusing into the sample during heat treatment. However none of the other samples that were heat treated at the same time produced such behavior (samples RD-5 and RD-9).

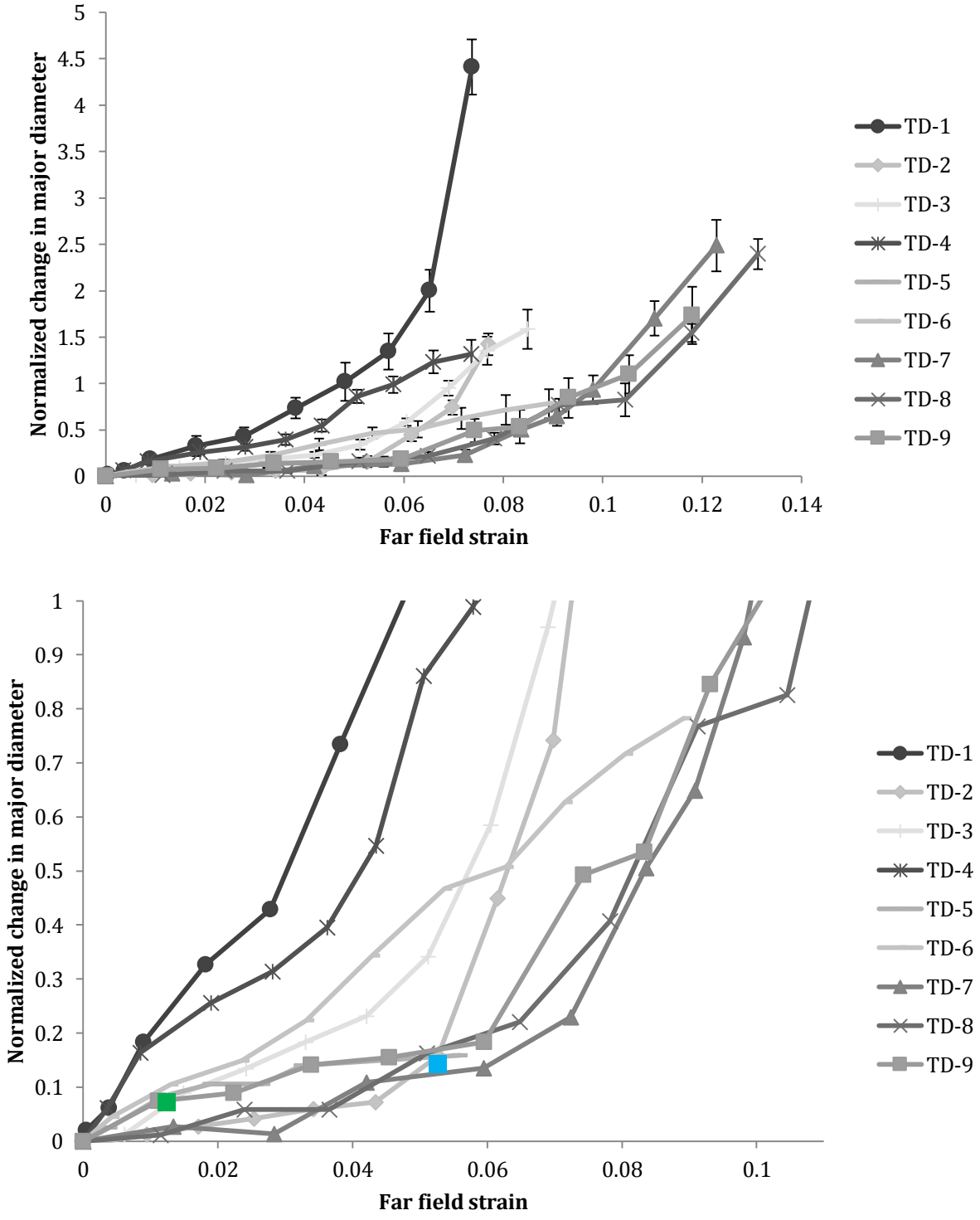

Figure 74: Normalized change in major diameter versus far field strain for TD samples, the first graph shows the entire data range; the second graph reduces the y-axis range and removes the error bars to better see the results; the blue square represent points where a crack forms through the void (TD-2) and the green square where cracks form elsewhere in the sample (TD-5)

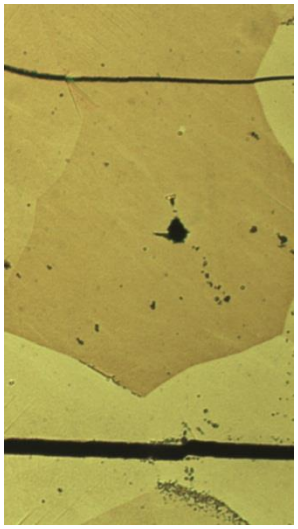

Figure 75: Cracks forming around the grain containing a void in sample TD-5

4.3.2 Results of Minor Diameter Measurements

Figure 76 displays the measured values of the change in minor diameter for the RD samples. Unlike the major diameter, the minor diameter decreases with increasing strain since compressive forces act in the x-direction (perpendicular to the tensile direction). However some of the samples such as RD-7 exhibit large increases in the minor diameter partially through the tensile test. This is evident of the void coalescing with a crack entering the grain.

The second graph in Figure 76 shows only the negative measurements of the changes in minor diameter. Unlike the major diameter results, there is no strong trend that is apparent in these results.

Figure 77 shows similar results for the TD samples, though there is stronger evidence of anisotropic behavior.

Note the large error bars for the minor diameter measurements. This is because there is generally extensive deformation occurring along the direction of the minor diameter, preventing truly accurate measurements. As the tensile test progresses this deformation increases, leading to larger error bars.

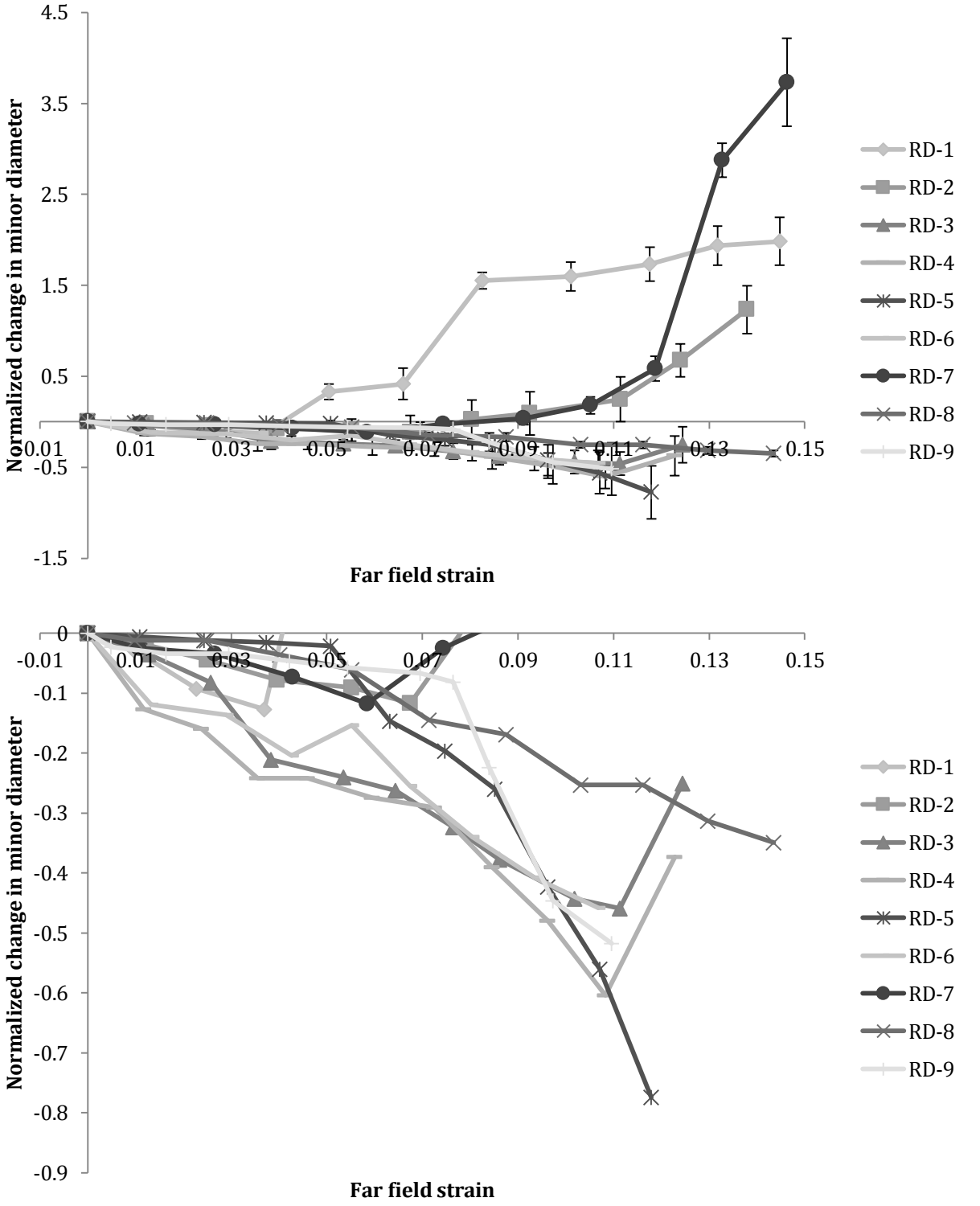

Figure 76: Normalized change in minor diameter versus far field strain for RD samples; the first graph shows the entire data range, while the second shows only the negative values and removes the error bars for clarity

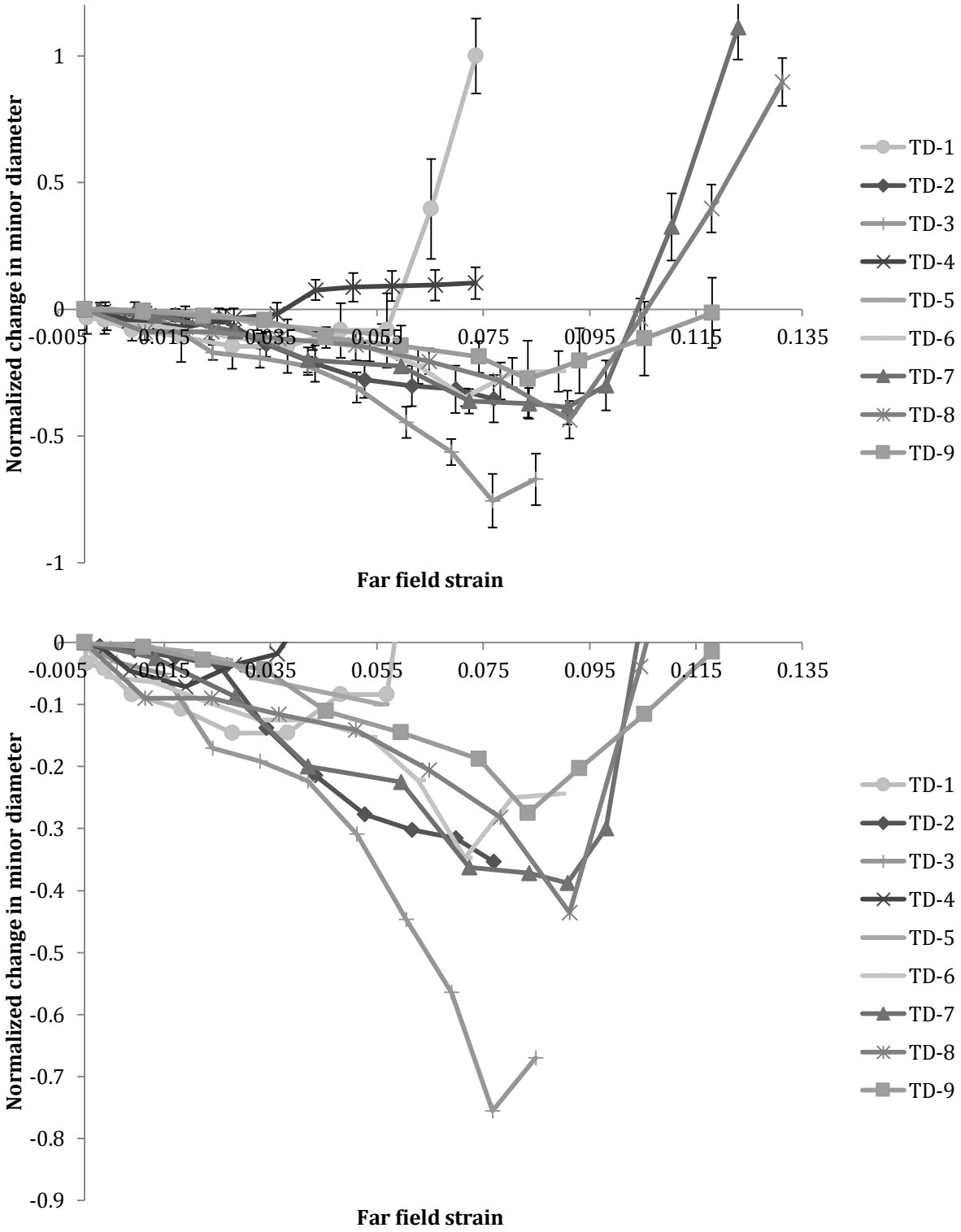

Figure 77: Normalized change in minor diameter versus far field strain for TD samples; the first graph shows the entire data range while the second shows only the negative values and removes the error bars for clarity

4.3.3 Local Strain Measurement During Tensile Tests

Using the DaVis software it was possible to monitor the strain evolution around each void during the tensile tests. An example of this is show in Figure 79 on the right. More examples of the DIC results for void growth and coalescence may be found in Chapter 5.3.

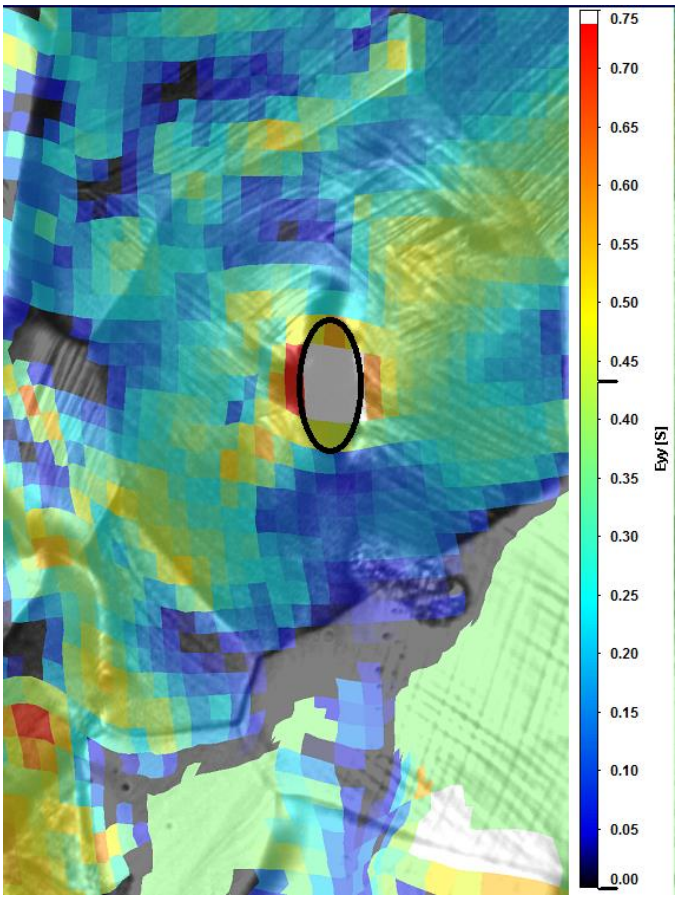

Figure 78: Example of strain measurement around a void in sample TD-8 via DaVis; the void is marked with a black ellipse for clarity

When extracting the strain values from the software, extra diligence was paid to making sure the values were taken from a predetermined point. The points selected were located on either the left side or right side of the void, as it is at these areas were maximum strain is seen within the grain.

Figure 79 plots the local strain next to the void versus the global bulk strain of the RD samples. The trends shown are comparable to the ones in Figure 72 (major diameter measurements for the same samples), with sample RD-1 showing the highest strain values due to the crack that propagated through the void early in the test. Similar trends can be seen in Figure 80, displaying the strain results for TD samples.

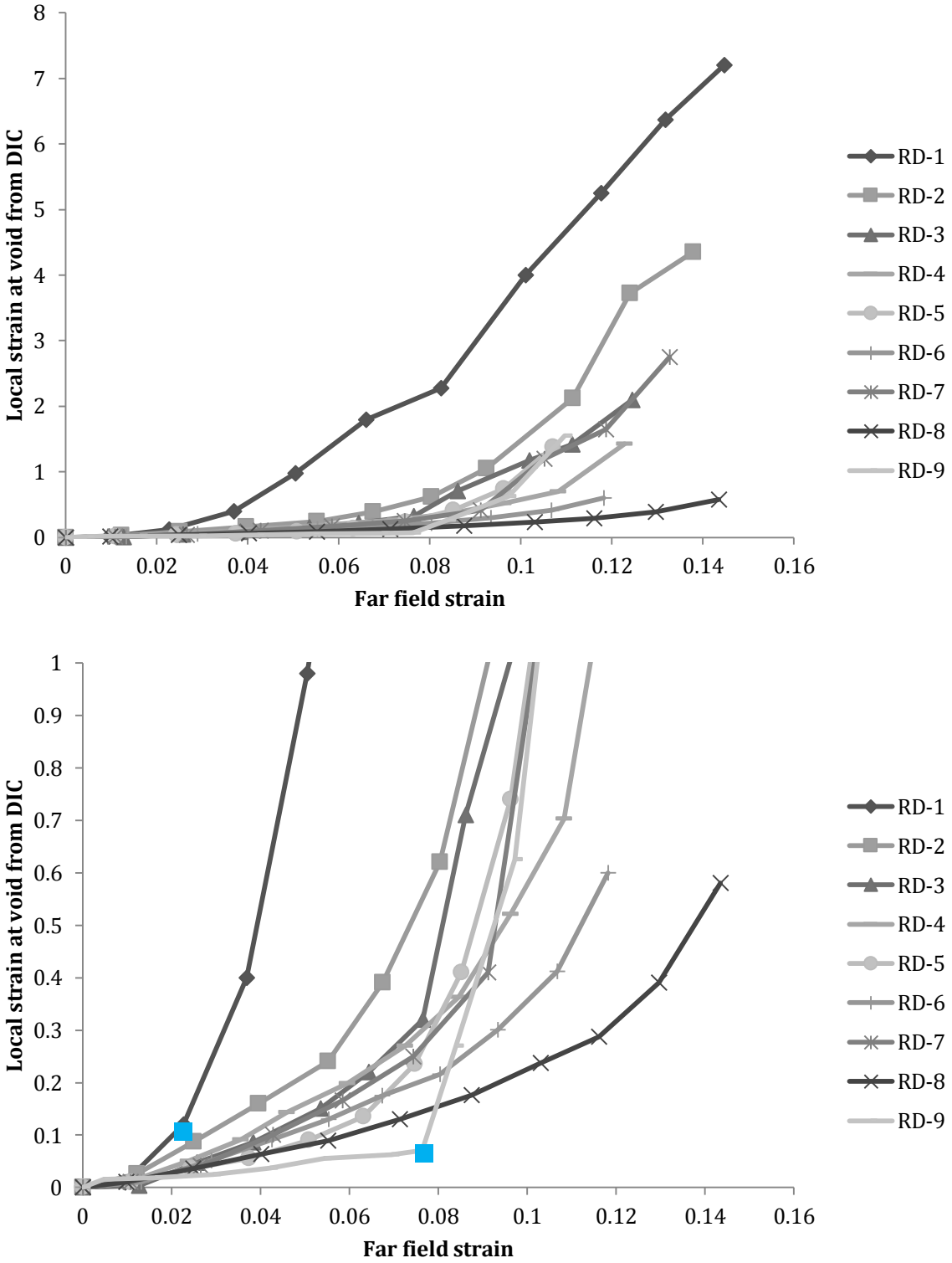

Figure 79: Local strain next to void versus far field strain for the RD samples; the first graph shows the whole data range and the second graph limits the y-axis range; the blue squares represent points where a crack forms through the void (RD-1 and RD-6)

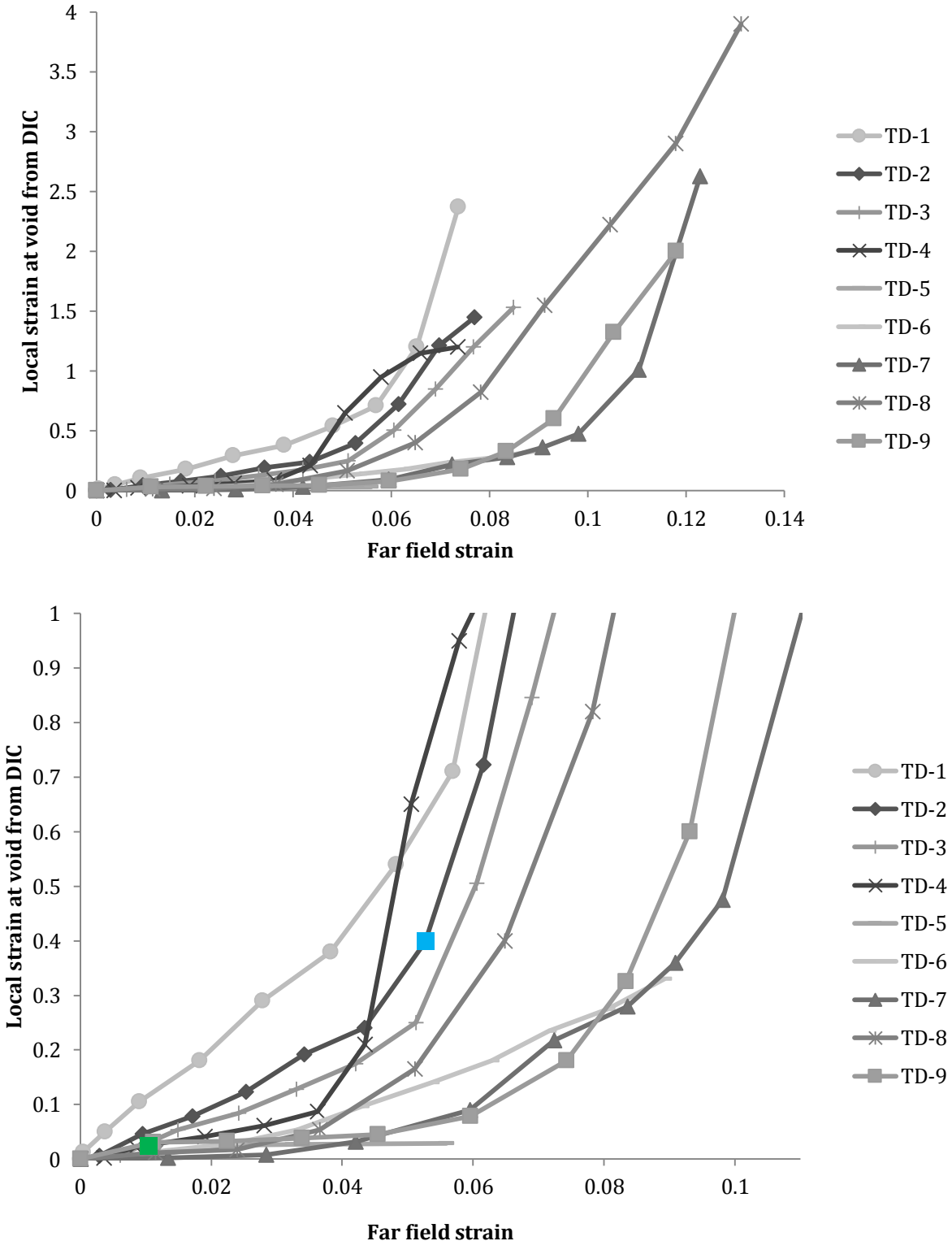

Figure 80: Local strain next to void versus far field strain for the TD samples; the first graph shows the whole data range and the second graph limits the y-axis range; the blue square represent points where a crack forms through the void (TD-2) and the green square where cracks form elsewhere in the sample (TD-5)

4.3.4 Comparison of Local Void Strain and Major Diameter

It is interesting to note that the strain measurements around the void and change in major diameter ($\Delta a/a_0$) are somewhat comparable. As seen in Figure 81 these values have a ratio that is close to 1, with the exception of samples RD-4 and RD-6. In the latter case this discrepancy is possibly due to the brittle crack that had formed through the void. For sample RD-4 this is most likely due to the errors brought up during the test. The sample was not properly held in place by the tensile machine grips so it began to slide out of them while also undergoing very slight deformation. The test had to be temporarily paused to tighten the grips, and in the process underwent a very strong loading shift.

Figure 82 shows the local void strain versus change in major diameter for the TD group of samples. A similar trend is shown here, though it is interesting to take note of samples TD-1 and TD-9. The former has a slope closer to 0.5 and the latter has a slope closer to 2. As can be seen in Figure 69, these samples lie on the opposite ends of the inverse pole figure. However sample TD-3 overlaps initially with TD-9 and then deviates, though going from sample TD-3's location on the inverse pole figure, it should be closer to the behavior of TD-1.

This type of analysis can be used to validate the results of the digital image correlation in a roundabout way. The normalized change in major diameter and calculated local strains are both strain measurements, though the former covers a slightly larger area.

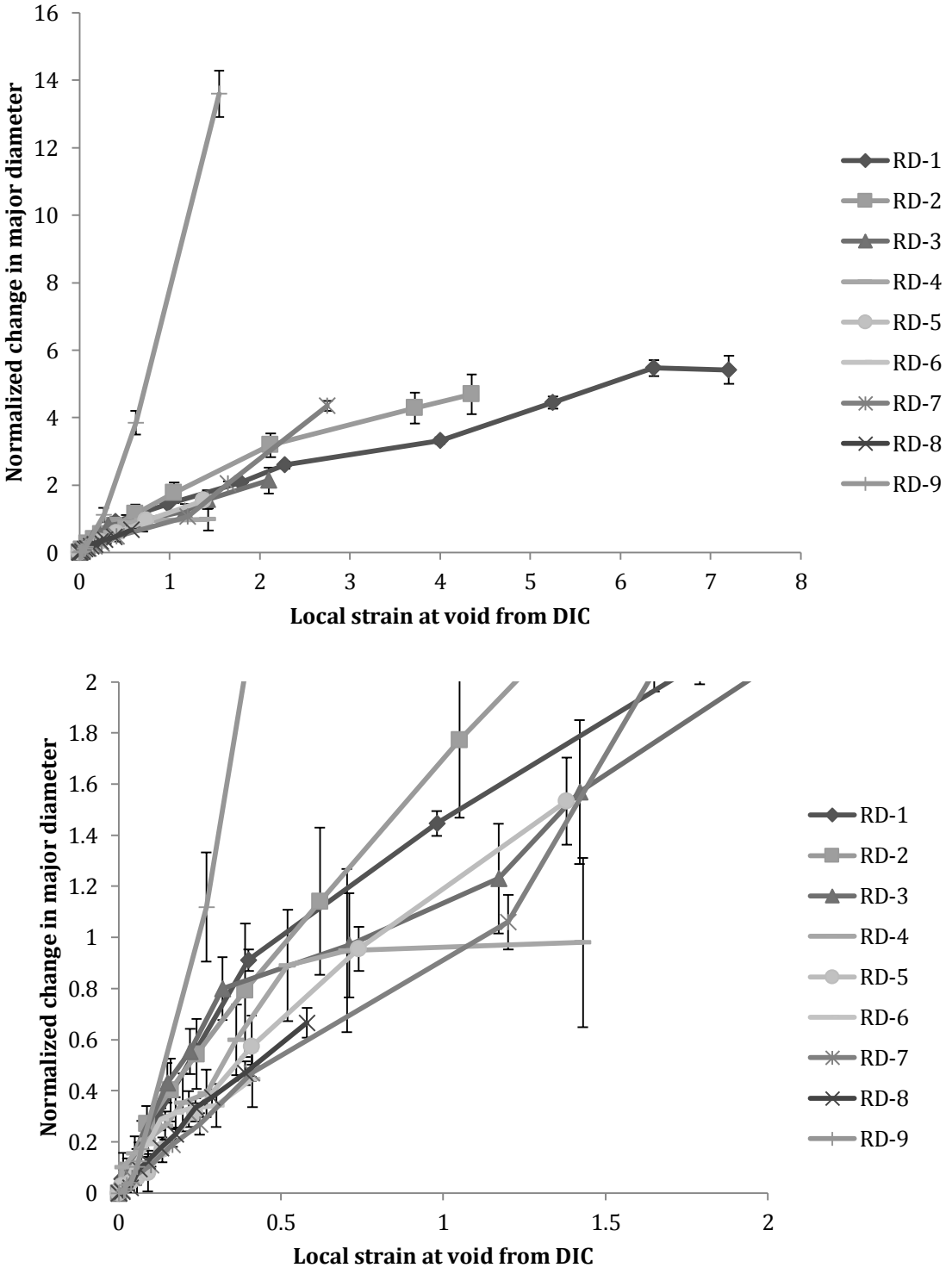

Figure 81: Local strain at void versus normalized change in diameter for RD samples; the first graph shows the whole data range and the second graph limits the y-axis and x-axis ranges

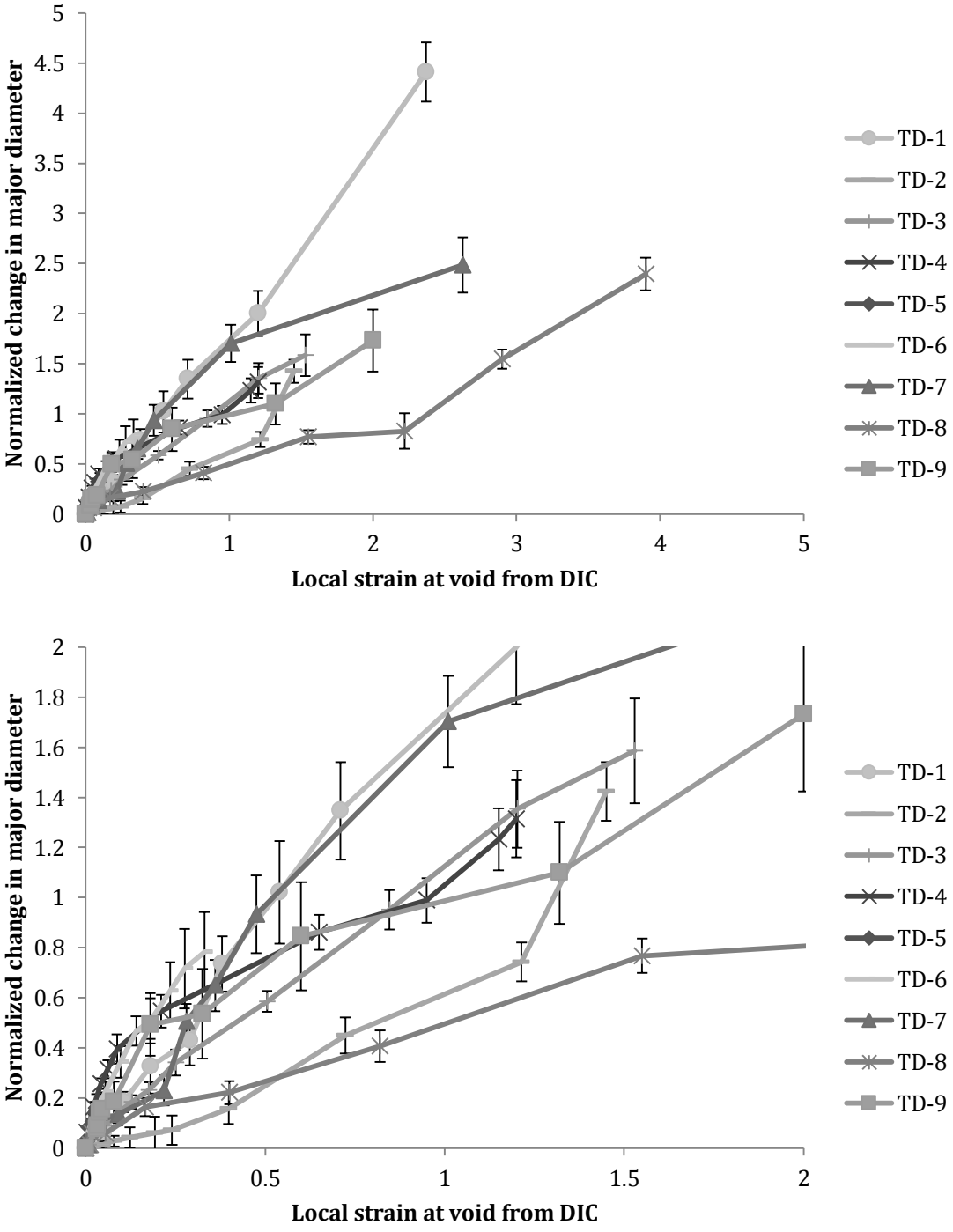

Figure 82: Local strain at void versus normalized change in diameter for TD samples; the first graph shows the whole data range and the second graph limits the y-axis and x-axis ranges

4.4 Void Coalescence Analysis

Another group of titanium tensile coupons were machined with two voids within a preselected grain. Since the voids were just under 13 µm in diameter, the intervoid spacing (edge-to-edge distance between them) was set at 30 µm, as shown in Figure 83. The next image Figure 84 shows the orientations of the samples used to study the coalescence phenomenon. They are labeled in increasing numbers going from left to right on the inverse pole figure, and from bottom to top. The samples oriented in the rolling direction are designated RD-C1 to RD-C7, and the samples in the transverse direction are designated TD-C1 to TD-C3. Euler angle data for the samples may be found in the appendix.

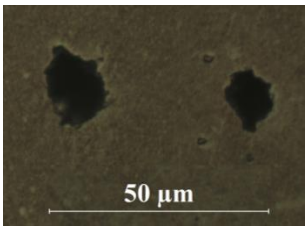

Figure 83: Sample RD-C6 with two voids machined into it

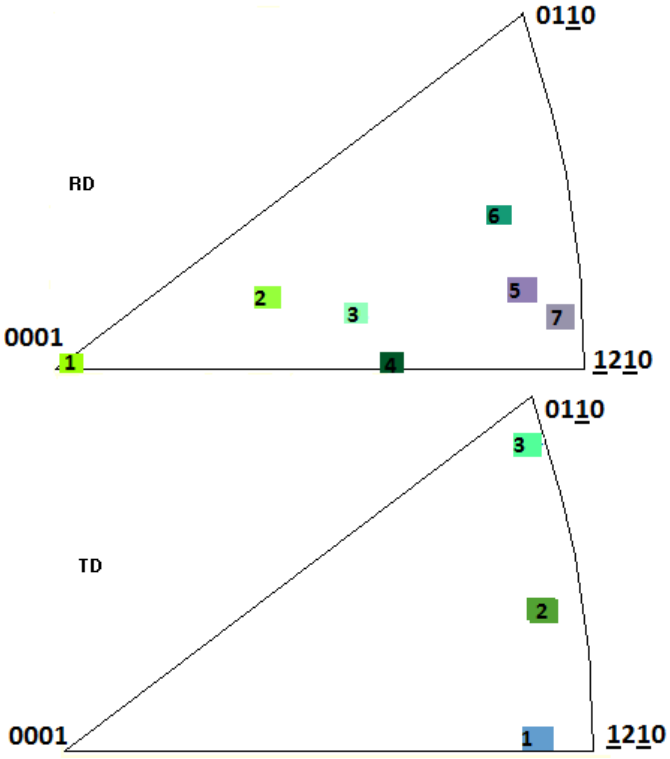

Figure 84: Inverse pole figures showing the orientations of the samples used to study void coalescence, 7 RD oriented samples and 3 TD oriented samples

Typically the coalescence can occur through two different processes. The voids will initially see elongation along the tensile direction causing the formation of shear bands typically at 45° angles to the tensile direction, and a decrease in the minor diameter of the voids. Once a critical condition is reached in between the two voids, the ligament between them will begin to neck down, and the minor diameter of the voids will begin to increase. Eventually coalescence and void linkage occur. This is demonstrated in Figure 85 below for sample TD-C2 (more graphs may be found in the appendix).

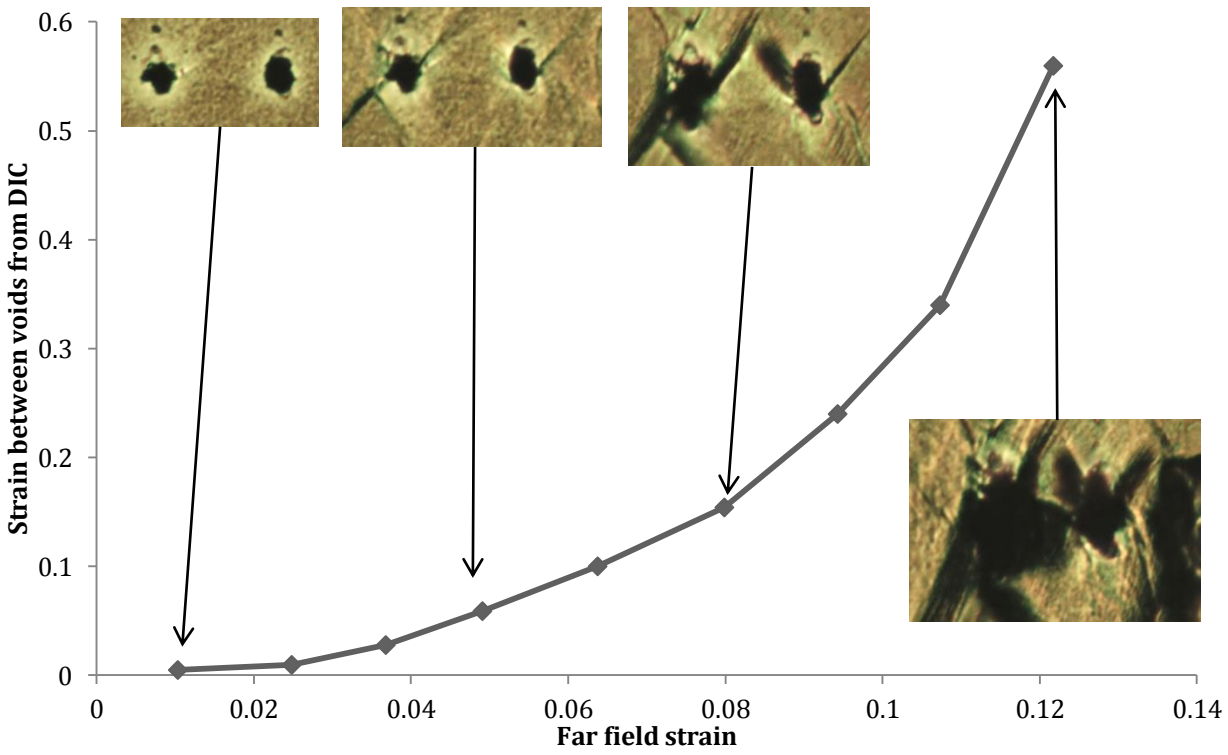

Figure 85: Graph of the strain evolution between the two voids versus far field strain for sample TD-C3

The second type of coalescence occurs in a similar manner, except instead of the inter-void ligament necking down to a point, the shear bands of the two voids create a path of high strain. This path forms the basis of the crack that will connect the two voids. This is exhibited in Figure 86 (more graphs may be found in the appendix)

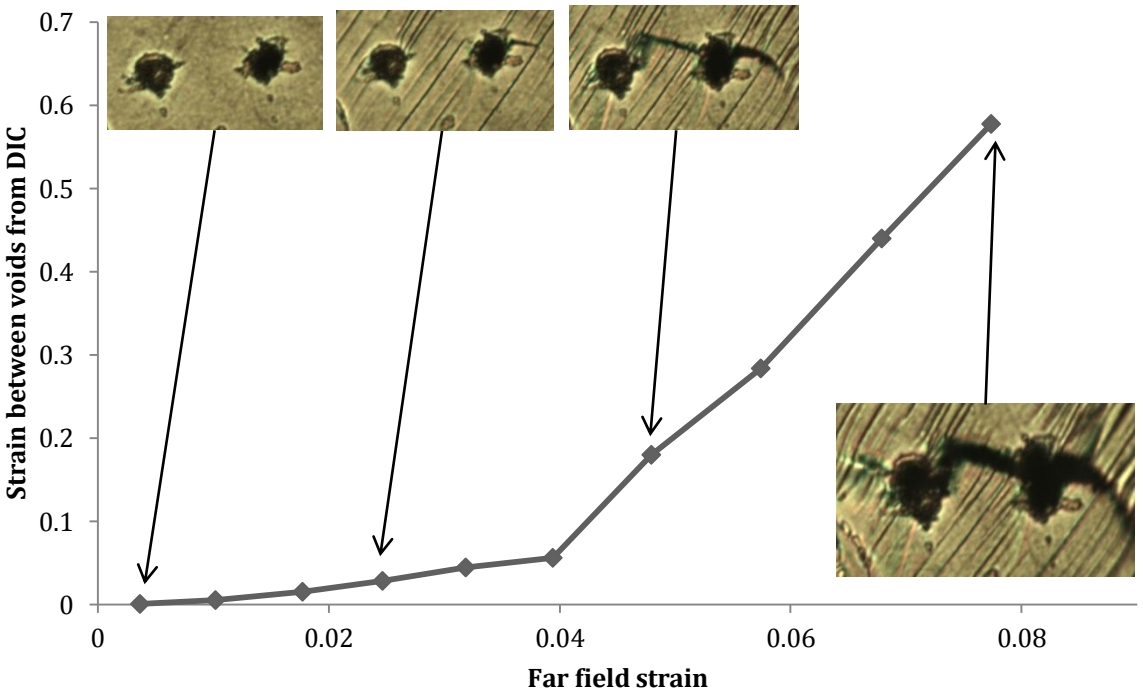

Figure 86: Graph of the strain evolution between the two voids versus far field strain for sample RD-C1

If we were to plot the strain evolution between the voids versus far field strain for all the RD samples, an interesting trend occurs (Figure 87). All the samples witness similar increase in strains initially, with a variable exponential increase partially through the tensile test. The harder grains see this exponential increase first, while the softer grains will see a delayed increase. This increase marks the beginning of the localization of the intervoid ligament (i.e. coalescence). Additionally, samples RD-C1 and RD-C2 are the only two samples that coalesced through crack formation, as opposed to necking down to a point, and this is evident in Figure 87 as they are the two hardest samples. Figure 88 shows the same information but for the 3 TD-C samples. All 3 of them coalesced by necking.

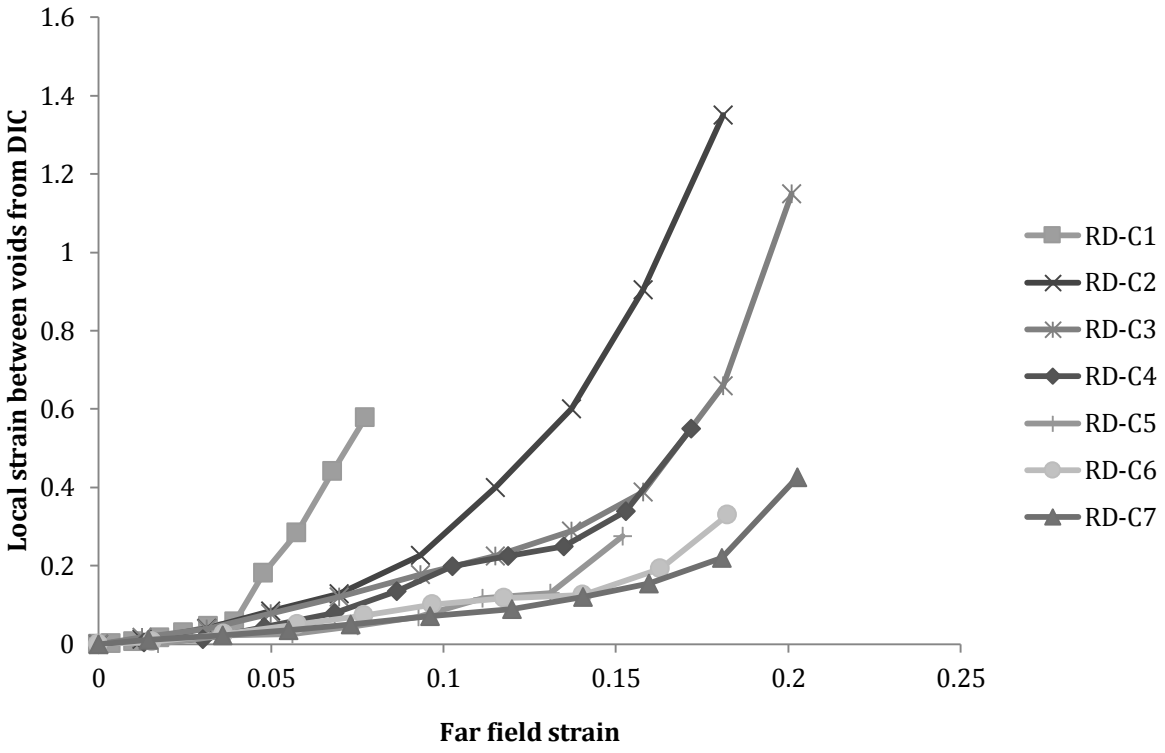

Figure 87: Strain between voids versus far field strain for the RD-C group of samples

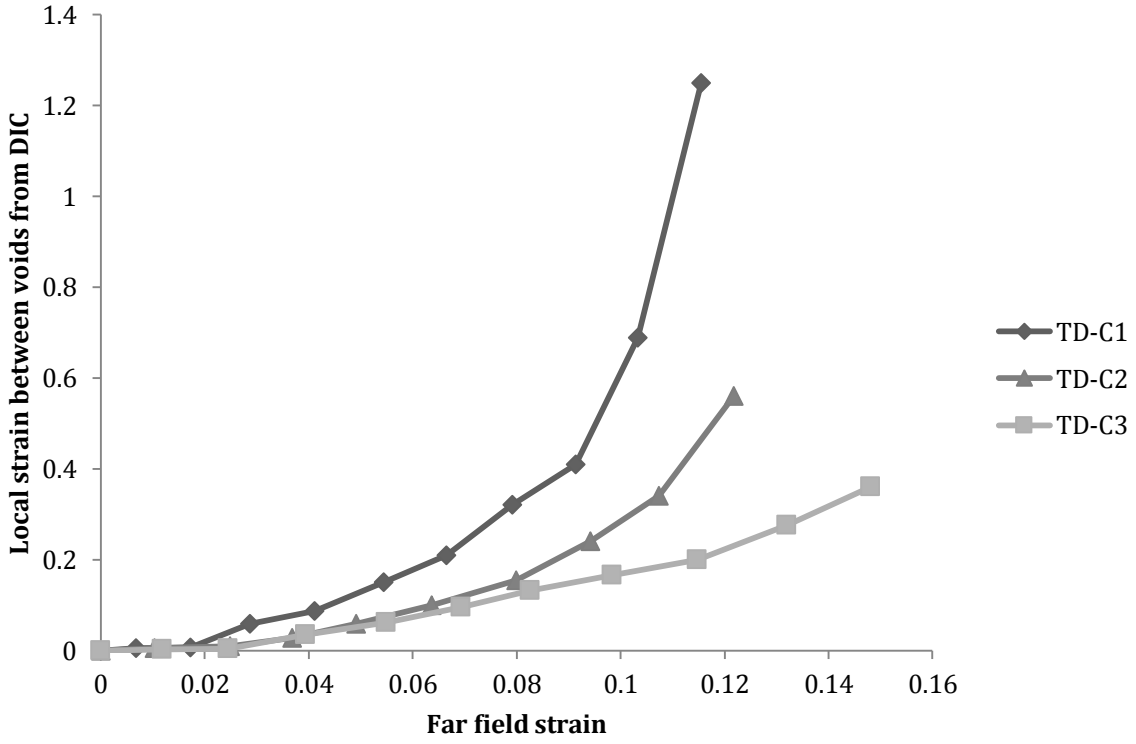

Figure 88: Strain between voids versus far field strain for the TD-C group of samples

4.5 Comparison of RD and TD-oriented Samples

As mentioned in the literature there is a difference in behavior of samples that are loaded along the rolling direction and samples loaded parallel to its transverse direction. This is evident in our results and is likely due to the texture differences between the two directions. First let us look at the stress-strain curves produced by these two sets of samples.

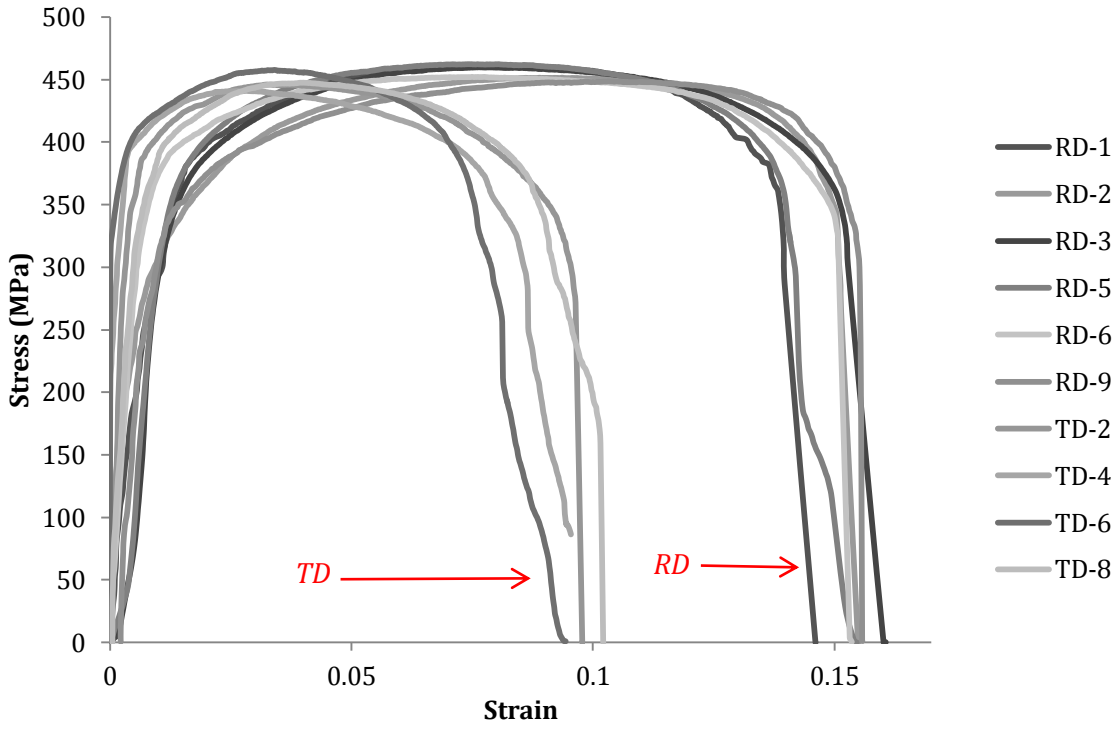

Figure 89: Stress-strain curves for samples tested along the TD and RD directions

In Figure 89 the samples oriented in the transverse direction have a lower failure strain than samples oriented along the rolling direction (approximately 0.1 versus 0.15, respectively). The TD samples also have a higher elastic modulus than the RD samples. The ultimate tensile strengths for all the samples are around 440 MPa. Note that all of the tensile coupons were heat-treated at 850 °C for 5 hours.

The fracture surfaces of a TD sample and an RD sample show no noticeable differences between the two, as seen in Figure 90 and Figure 91. Both demonstrate a fibrous and ductile fracture surface full of dimples (voids that had formed in the bulk). Both images also contain areas with smooth surfaces, likely caused by intergranular fracture through grains of a hard orientation (c-axis or [0001] direction parallel to tensile direction).

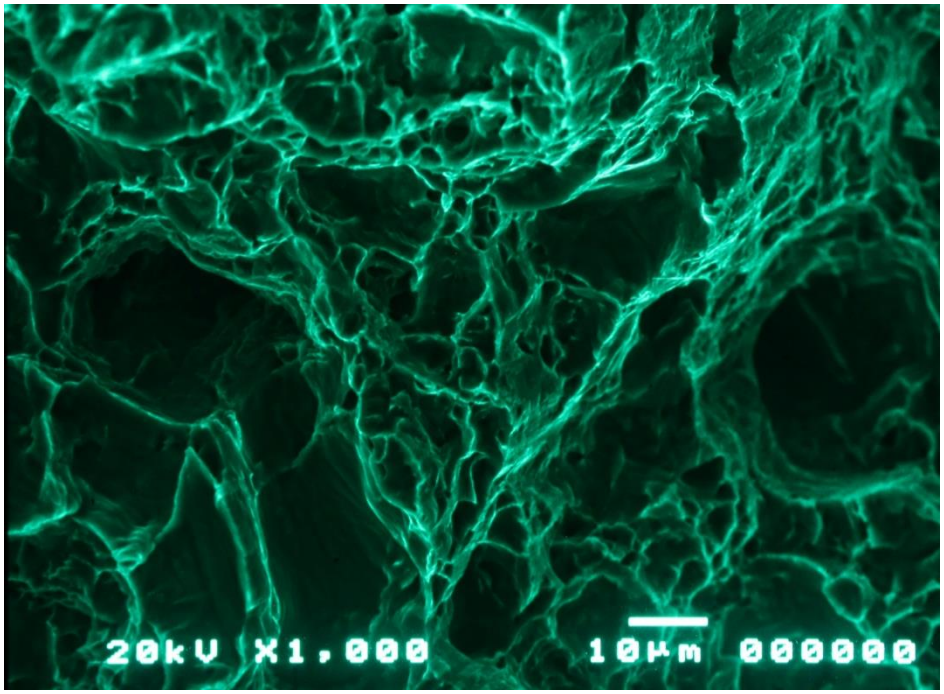

Figure 90: Fracture surface of RD-3

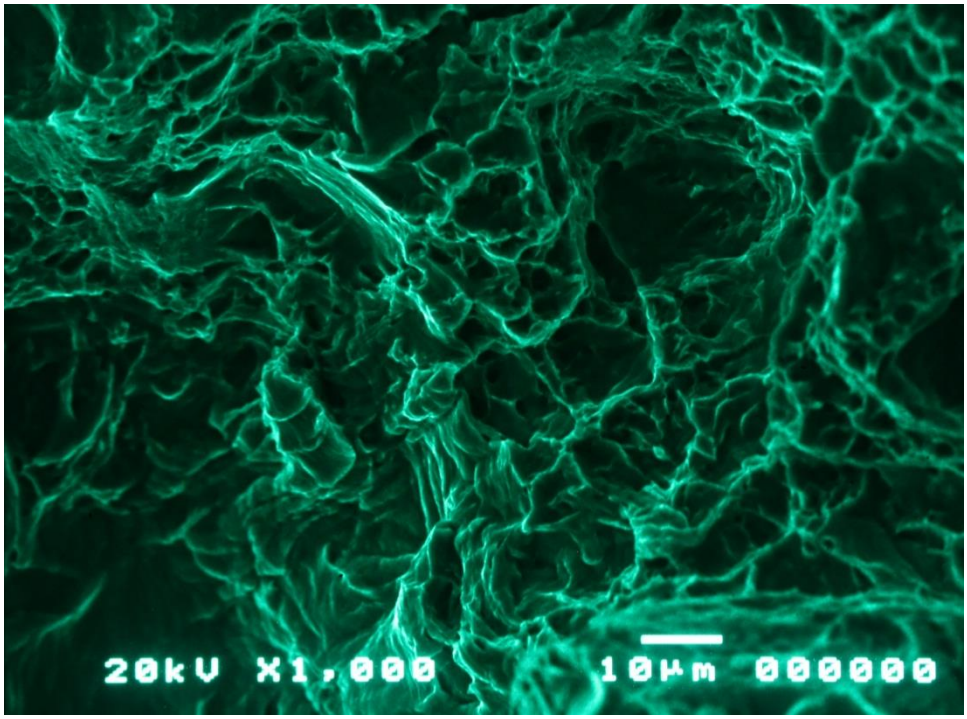

Figure 91: Fracture surface of TD-9

However an interesting idea crops up when comparing the evolution of the major diameter of the RD and TD samples. As an example we will refer to samples RD-2 and TD-1 since these two samples contain voids in crystals with similar orientations (refer to the inverse pole

figure, Figure 67 on page 86), in addition to samples TD-6 and RD-7 (again because these samples have similar orientations). In Figure 92 the two samples are initially divergent but then become almost parallel towards the end of the test, whereas in Figure 93, the two graphs overlap.

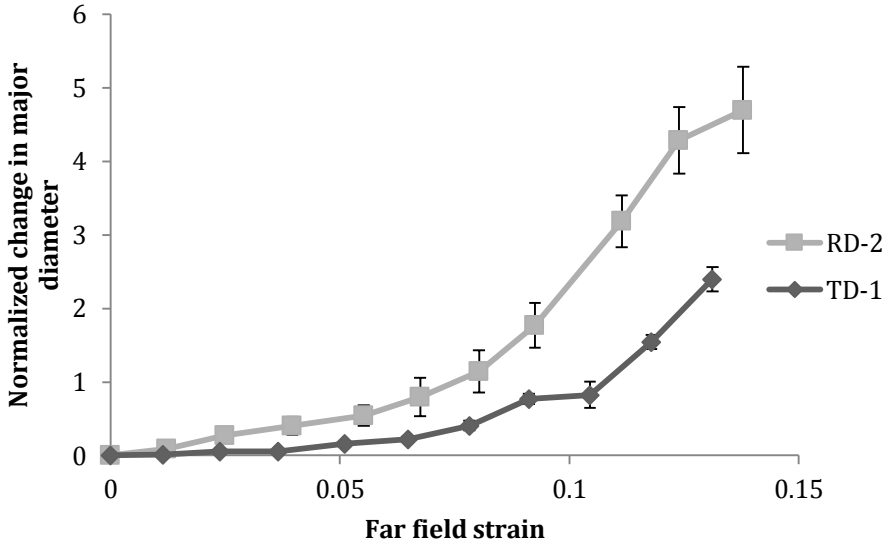

Figure 92: Normalized change in major diameter versus far field strain for samples RD-2 and TD-1

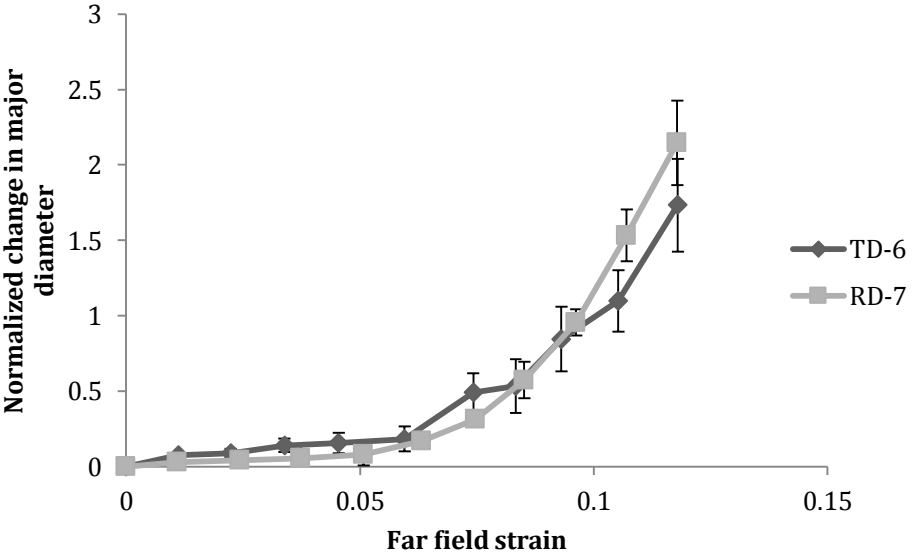

Figure 93: Normalized change in major diameter versus far field strain for samples TD-6 and RD-7

The local strain analyses of these two pairs of samples are shown in Figure 94 and Figure 95. In both cases the two curves almost overlap, giving credence to the idea that these two

samples are very similarly oriented. Though this raises the question of why the major diameter measurements in Figure 92 above do not overlap, the answer to which is not clear.

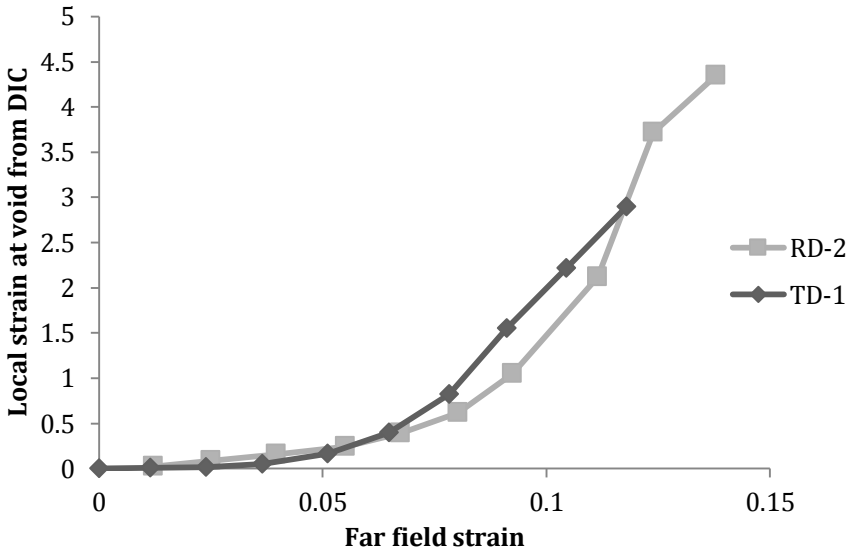

Figure 94: Local strain at void versus far field strain for RD-2 and TD-1

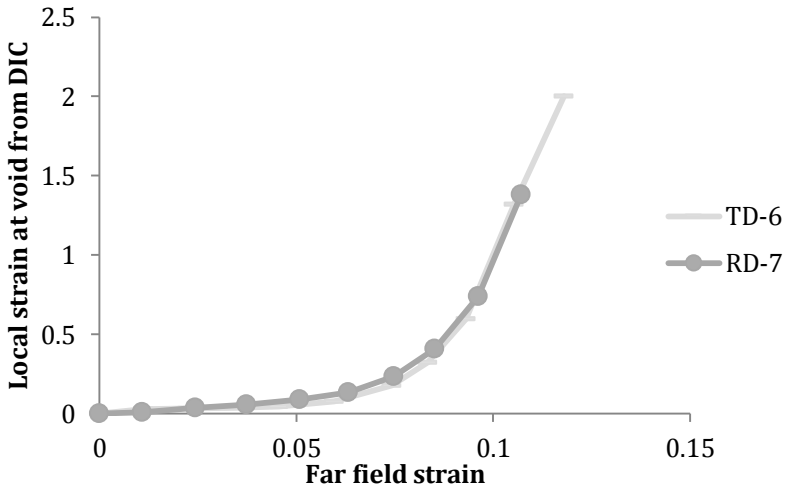

Figure 95: Local strain at void versus far field strain for TD-6 and RD-7

Note that the macro stress-strain curves for these two samples are different, whereas the local strain analysis is the same. This is because on the macroscale the rolling direction affects the cumulative texture of the grains, leading to macroscopic differences in mechanical properties. However on the scale of the individual grains only the orientation of the grains in question are important and to a lesser extent, the surrounding grains.

Chapter 5: FEM Results

This chapter will go into detail regarding the results of using the crystal plasticity subroutine. At first the methodology to determine the Voce hardness parameters is shown along with the parameters themselves. This is followed up with the results of basic crystal orientation manipulation (rotation about the *a*-axis). Finally we will compare the FEM results with experimental results.

5.1 Determining the Voce Hardness Parameters

Initially simulations were attempted using values taken from the literature, in particular values proposed by Gurao *et al*. [111]. The simulation was a cube that contained 1000 elements, with each element portraying a randomly oriented grain. This cube is supposed to represent bulk polycrystalline titanium. Upon insertion of the Voce parameters and loading the cube in tension, a stress-strain curve is generated. This plot is compared with the stress-strain curve of a heat-treated Titanium specimen.

Using the values proposed by Gurao *et al*. [111], the simulation did not produce a similar response to our experimental stress-strain curve. There are a few reasons for this, particularly that Gurao's tests were conducted in compression and at high strain rates, while our tests were conducted in tension and at near quasi-static rates.

There are 4 Voce parameters for each slip system. HCP materials like titanium have 4 independent slip systems, amounting to a total of 16 parameters. In an ideal scenario one would design 16 different types of mechanical tests (compression, torsion, bending, etc.) to independently verify each parameter through trial and error. Due to time restrictions this was not possible. Instead through adjusting each value and running the simulation via Abaqus, while continuously checking the results with experimental stress-strain curves, the values in Table 10 were settled upon.

Figure 96 shows the stress-strain curve generated via the FEM along with an experimental stress-strain curve. Past the UTS (ultimate tensile strength) point the two curves deviate as the FEM does not account for internal void nucleation/growth/coalescence, which causes the experimental results to plateau slightly then begin decreasing.

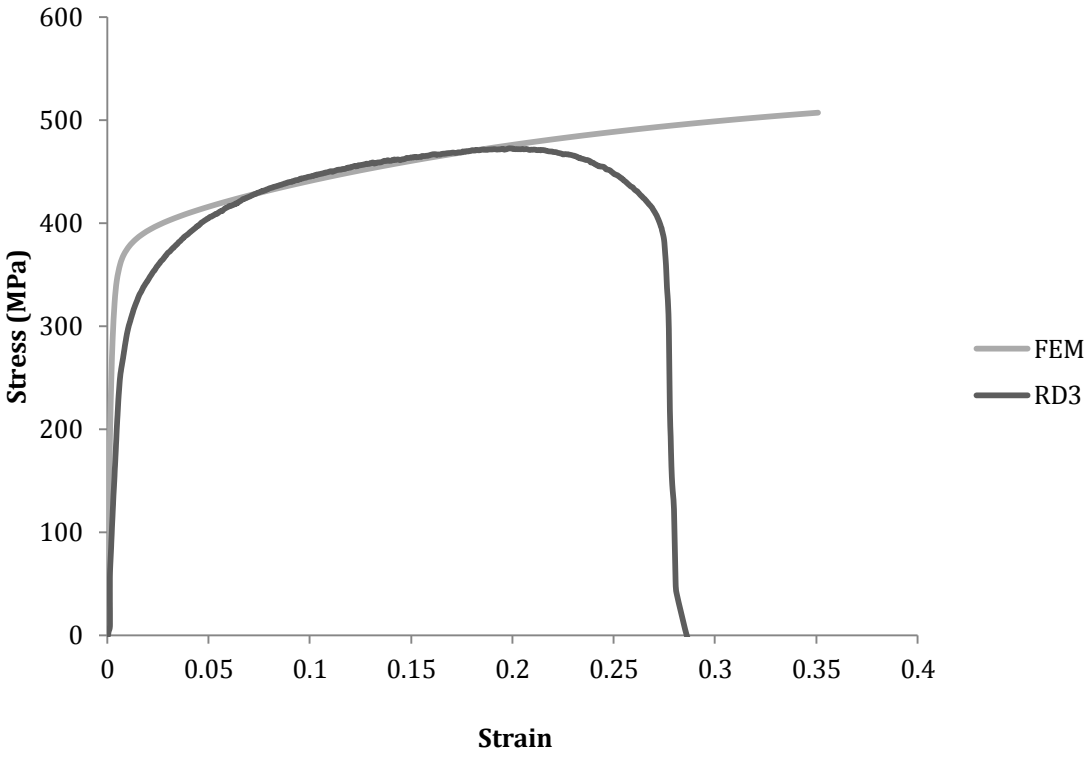

Figure 96: Stress-strain curve showing the FEM and experimental results.

Table 10: Voce parameters for the 4 sets of slip systems (refer to Table 4 on page 17 for details on each system)

Slip system type	τ_0 **(MPa)**	τ_s **(MPa)**	h_0**(MPa)**	h_1**(MPa)**
1	103.923	115.47	1000	180
2	90	100	1000	180
3	900	1000	1000	180
4	235.69	261.878	1000	180

5.2 Rotation about the a-axis in the Unit Cell

In order to get an understanding of how the HCP single crystal behaves in different orientations, we took a single crystal containing a single void (Figure 40 on page 52) and oriented it such that it's *a*-axis was parallel to the tensile direction (the y-axis of the global system). Boundary conditions were placed such that each face of the cube could not bend out of plane they are contained in with the exception of the front face. This was done to simulate

the boundary conditions of the grains in the test specimens. The simulations were re-run with the crystal being rotated about the x-axis in increments of 10°.

Based on the literature it was expected to see a generally decreasing strength as the rotation angle increases but this was not so. Instead a sinusoidal pattern with a period of 60° was received. Figure 97 below shows the peak strain measured around the void versus the angle of rotation about the x-axis. All measurements were taken at a strain of 50%. Based on the literature (Figure 19 on page 26 in particular), a linear decreasing trend was expected.

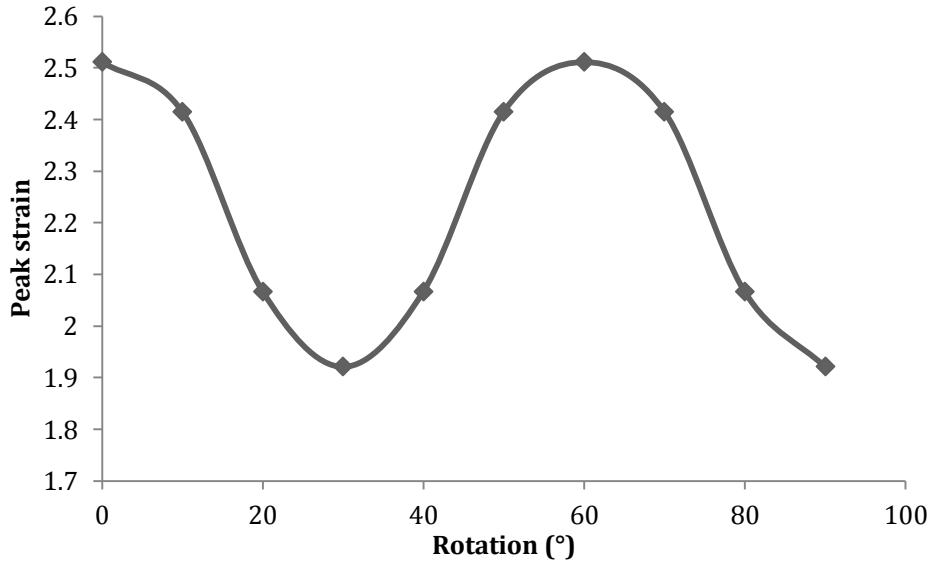

Figure 97: FEM results for peak strain around the void versus angle of rotation about the x-axis

The reason for such a result may be in part due to the Voce hardness parameters that were settled upon. Prismatic slip (slip system 2 in Table 10 on the previous page) is supposed to be the most active slip system in HCP titanium, meaning that it should have the lowest slip activation and hardness values. However the parameters of slip system 1 (basal slip) and 2 are very close, possibly leading to the activation of the first slip system when it would not be active in reality. Unfortunately the subroutine used to model crystal plasticity does not provide information as to which systems are activated during a simulation.

The results of the normalized change in major diameter versus far field strain are shown in Figure 98 for the above mentioned simulations. Note that only the first 4 simulations are shown as the rest of the simulations repeat the data. In terms of the trends shown there is

not much variation in terms of the results with a maximum difference between the major diameter values of 0.283 (which is 4.245 μm). Also note that the graphs of 0°, 10° and 20° do not intersect with each other, while the 30° graph follows a different pattern and intersects through all of them. This is a likely indicator of a different slip system being activated.

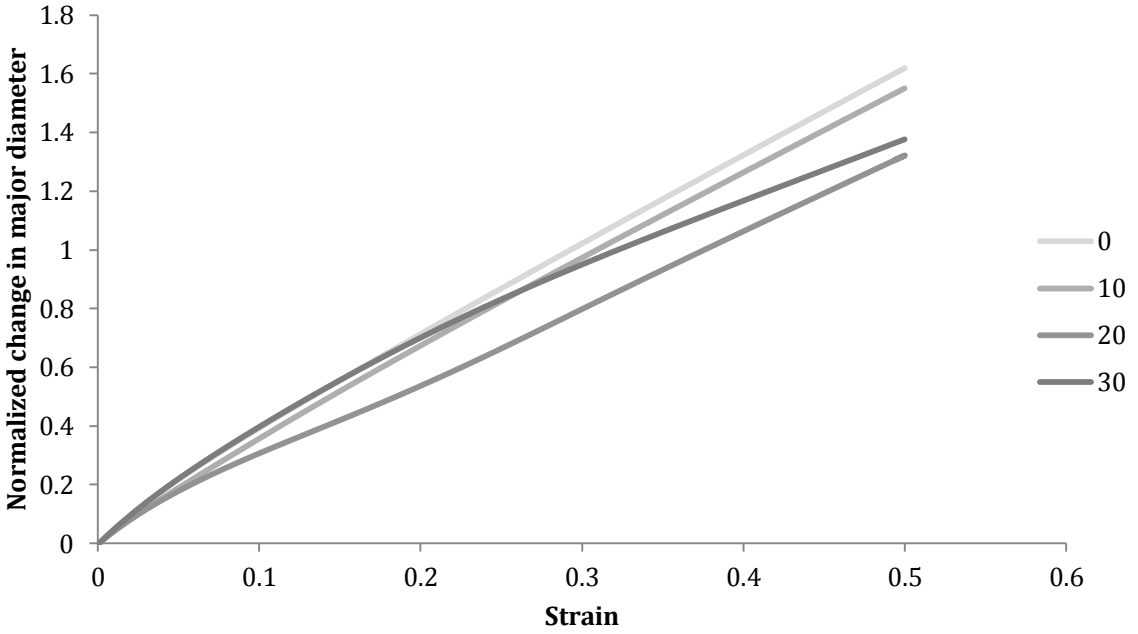

Figure 98: FEM results for normalized change in major diameter versus far field strain for the crystals rotated about the *a*-axis; only 4 simulations are shown as the others repeat the same data

5.3 Simulating Test Specimens

In order to tell the crystal plasticity subroutine the orientation of a grain, the [100] and [001] directions of its unit cell are represented as vectors within the global Cartesian system. The EBSD analysis of our test specimens provides us with the Euler angles of the grains. These Euler angles can be converted into a vector notation with the following rotation matrix (taken from [112]):

$$\begin{bmatrix} \cos\varphi_1 \cos\varphi_2 - \sin\varphi_1 \sin\varphi_2 \cos\Phi & \sin\varphi_1 \cos\varphi_2 + \cos\varphi_1 \sin\varphi_2 \cos\Phi & \sin\varphi_2 \sin\Phi \\ -\cos\varphi_1 \sin\varphi_2 - \sin\varphi_1 \cos\varphi_2 \cos\Phi & -\sin\varphi_1 \sin\varphi_2 + \cos\varphi_1 \cos\varphi_2 \cos\Phi & \cos\varphi_2 \sin\Phi \\ \sin\varphi_1 \sin\Phi & -\cos\varphi_1 \sin\Phi & \cos\Phi \end{bmatrix} \quad \{\text{Eq. 36}\}$$

When the Euler angle values are plugged into the above matrix, the first and third columns will result in the vectors representing the [100] and [001] directions, respectively (in the HCP Miller-Bravais notation this would be the [10$\underline{1}$0] and [0001] directions).

To study void growth, samples RD-1, RD-7 and RD-9 were simulated by retrieving the [100] and [001] vectors from the above rotation matrix and inserting them into the model shown in Figure 40 on page 52. These samples were selected because they are close to the 3 corners of the inverse pole figure (see Figure 69 on page 87). For sample RD-1 (Figure 99) a crack propagated through the void early in the test causing a large discrepancy between the experimental and simulated results. Samples RD-7 and RD-9 (Figure 100 and Figure 101 respectively) show a good fit between the experimental and FEM results during the early stages of loading, but then deviate at a far field strain of 0.08. This is most likely due to the voids meeting with a ductile crack that has formed.

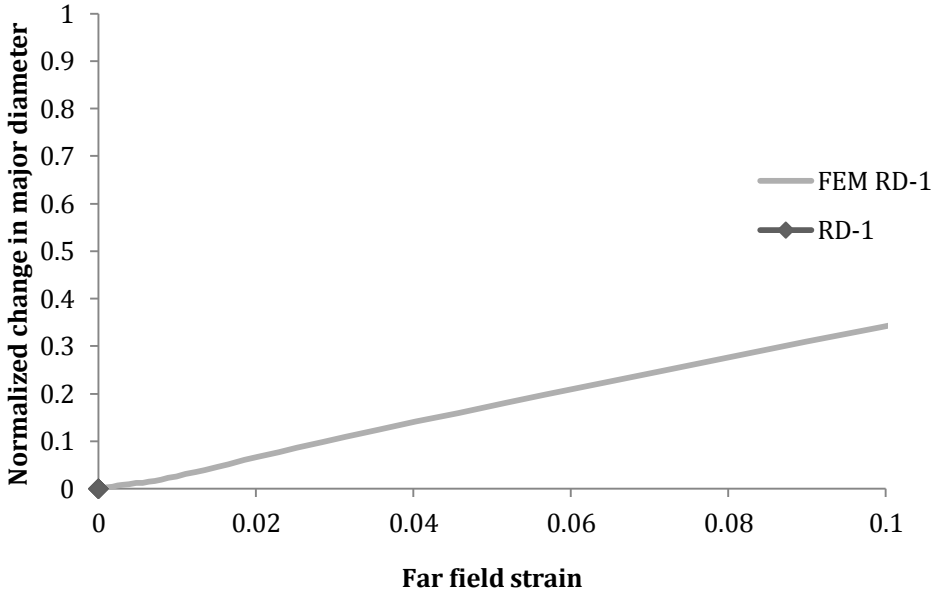

Figure 99: Experimental and simulated normalized change in major diameter for sample RD-1

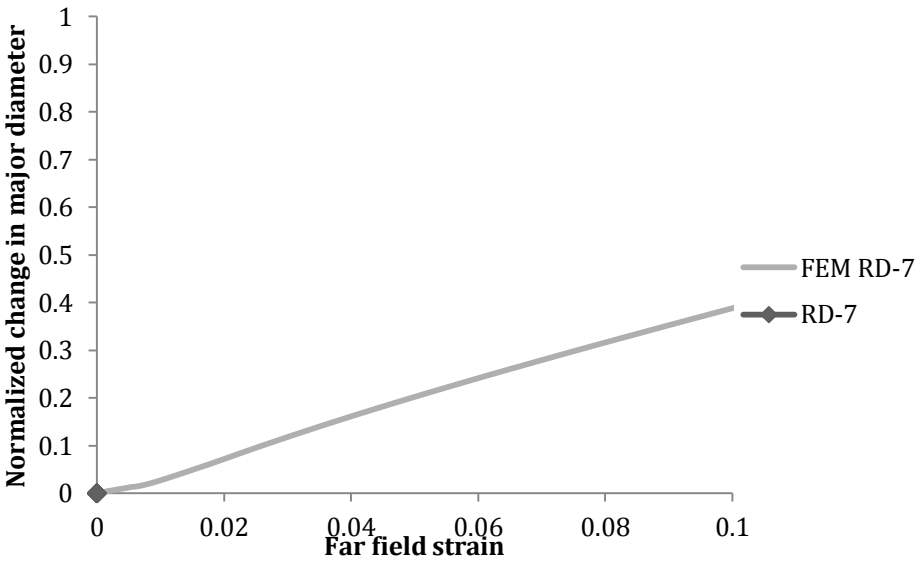

Figure 100: Experimental and simulated normalized change in major diameter for sample RD-7

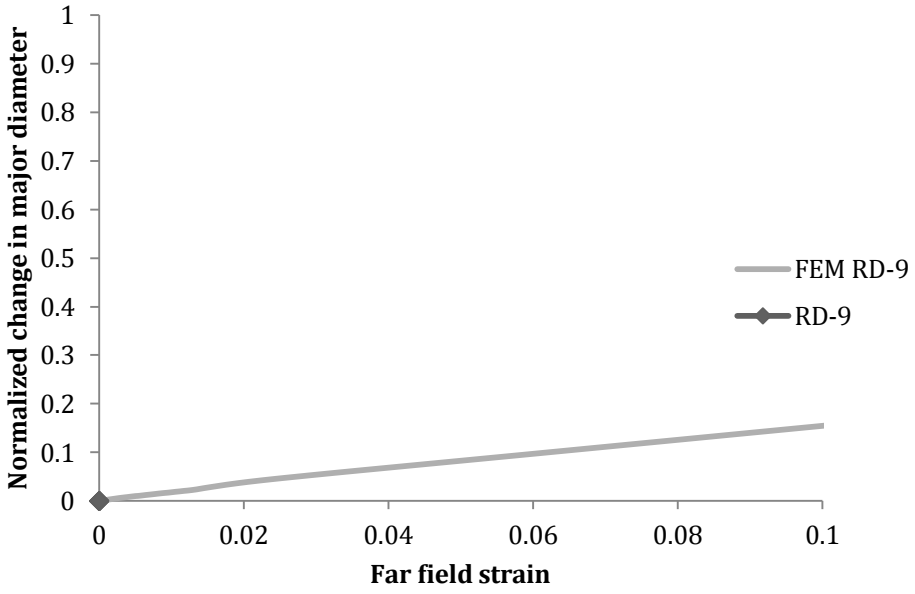

Figure 101: Experimental and simulated normalized change in major diameter for sample RD-9

If we were to compare the FEM results amongst themselves, we can see that a qualitative similarity to the experimental results is apparent (as shown in Figure 102), i.e. RD-1 behaves in a stronger manner than RD-7 and RD-9.

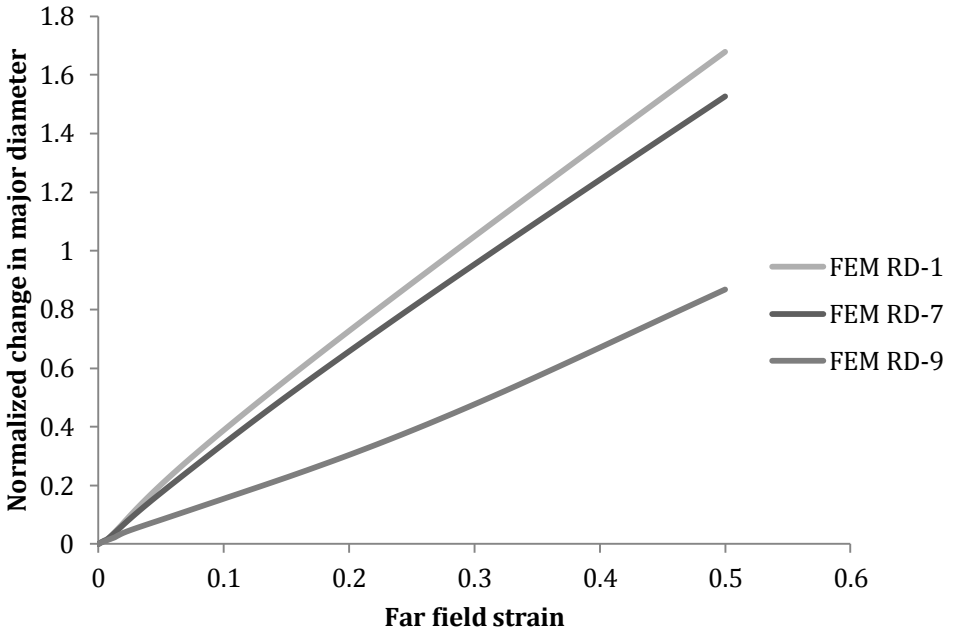

Figure 102: Comparison of FEM results of normalized change in major diameter for samples RD-1, RD-7 and RD-9

Figure 103 compares the local strain results from the DIC analysis with the simulated FEM strain results for sample RD-7. The results show that the crystal plasticity subroutine appropriately predicts the local strain evolution around the void, specifically the formation of the shear bands at a 45° angle to the horizontal. The experimental results also produce this shear band though slightly askew to the 45° angle. Additionally the shape of the void evolves in a similar manner between the FEM and experimental results.

Figure 104 shows the same information but for sample RD-9. In the FEM results the shear bands form not at a 45° angle to the horizontal, but at a bearing of about 10° to the horizontal and vertical directions. In the experimental results, slip bands can be seen passing through the void in only one of these directions.

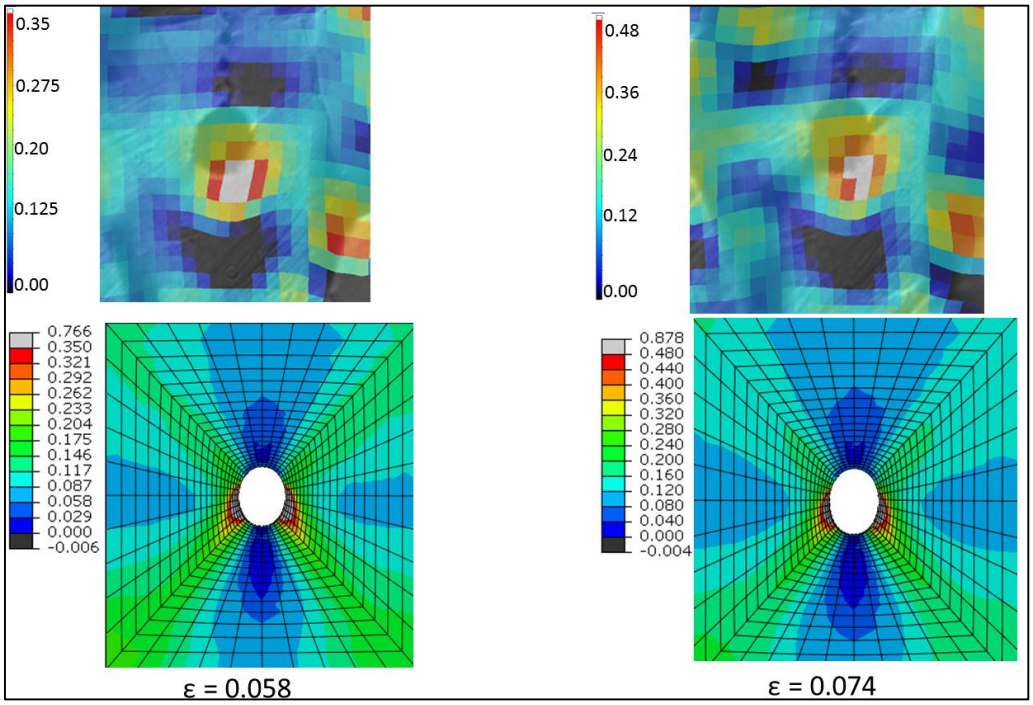

Figure 103: Comparison of DIC results with FEM results at different far field strains for sample RD-7

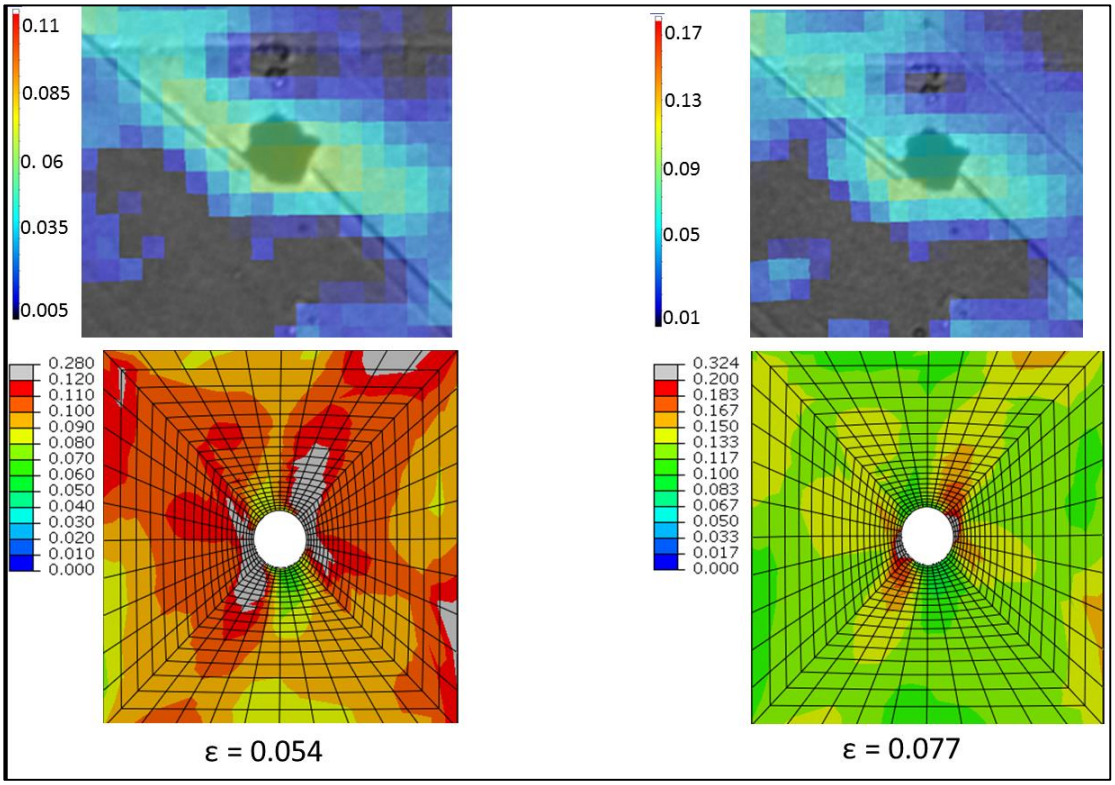

Figure 104: Comparison of DIC results with FEM results at different far field strains for sample RD-9

In order to study void coalescence, a model containing two voids was created, shown in Figure 105. The samples chosen for this study was RD-C1, RD-C7 and TD-C3 because these samples have their grains located closest to the 3 corners of the inverse pole figure (according to Figure 84 on page 102).

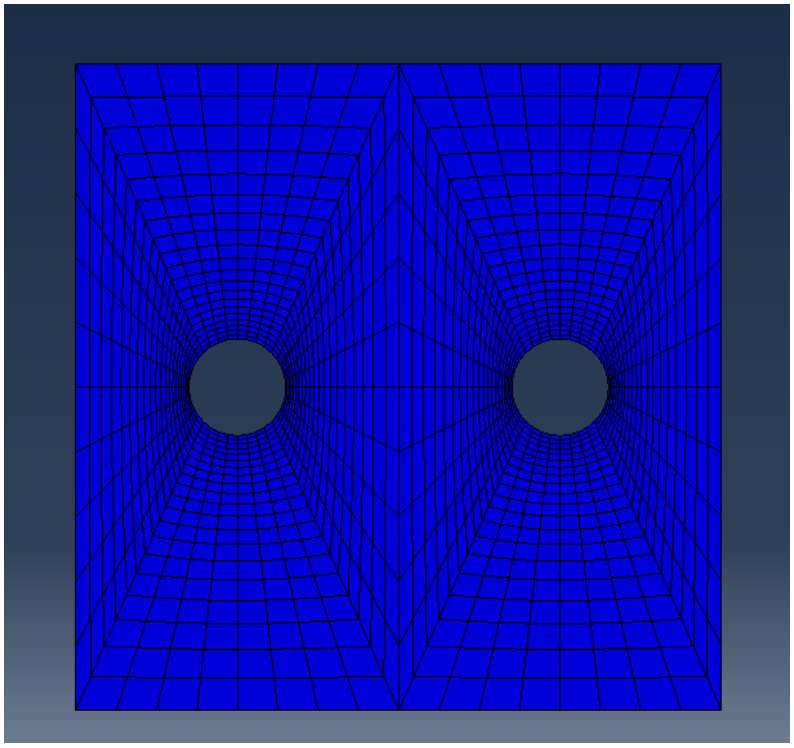

Figure 105: Model of a grain with two voids used to study void coalescence

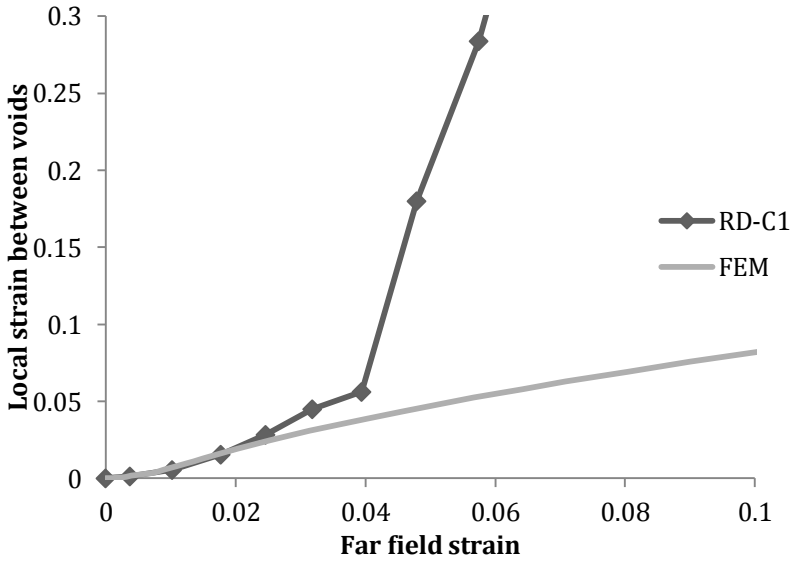

Figure 106: Simulated versus experimental data for the strain between voids in samples RD-C1

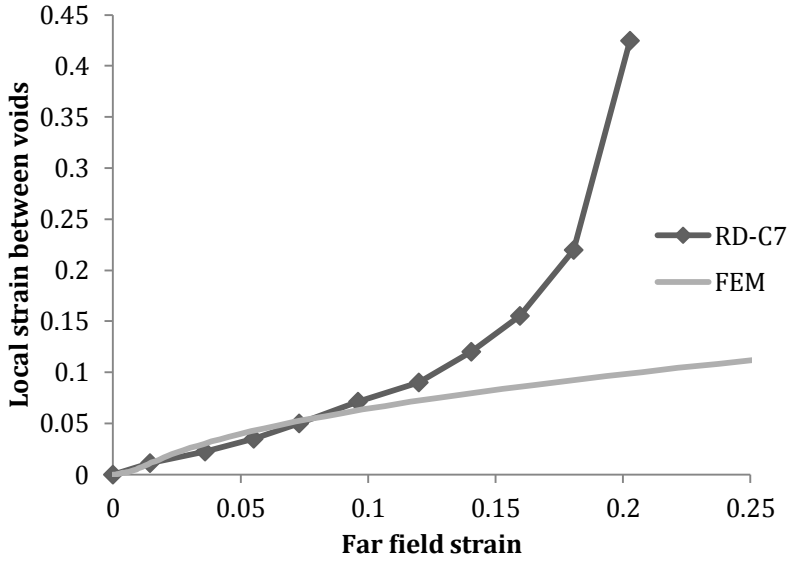

Figure 107: Simulated versus experimental data for the strain between voids in samples RD-C7

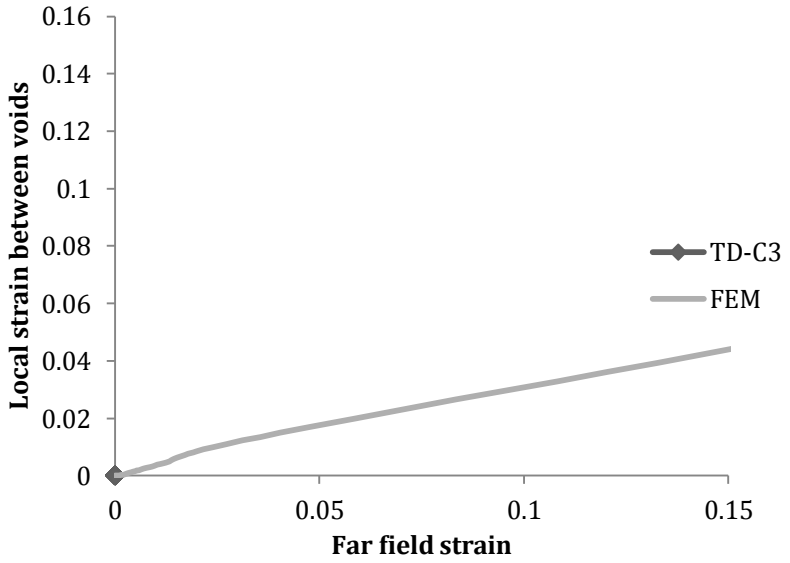

Figure 108: Simulated versus experimental data for the strain between voids in samples TD-C3

A similar trend to void growth appears in void coalescence, as seen in the above 3 figures (Figure 106, Figure 107 and Figure 108). The crystal plasticity subroutine provides a good prediction of strain evolution between voids at low bulk strains, but then deviates at higher strains. This is because the subroutine cannot predict the onset of coalescence and the results of such a process. This is also evident in the above figures by the concavity of the curves. The experimental results have a trend with positive concavity, while the FEM has a

negative concavity initially then trends towards linearity past a bulk strain of 0.1. It is the coalescence process that causes the exponential increase in void growth and strain in our experimental results. In the absence of coalescence these parameters would likely behave similarly to what the FEM results predict.

In Figure 109 the results of DIC analysis is compared with the FEM results for local strain evolution in sample TD-C3. In the DIC results strain localizes around the void in the familiar 45° angle". The FEM results also show the localization of shear bands in a similar manner but stronger in the bottom half of the crystal..

Figure 110 shows the evolution strain in sample RD-C1, for both the DIC and the FEM. At the highest far field strain, the FEM correctly predicts that the right void will see more deformation than the void on the left. The crack that forms in the experimental results skews the strain localization around the right void slightly, but it is similar to the band that forms on the right side of the void in the FEM results.

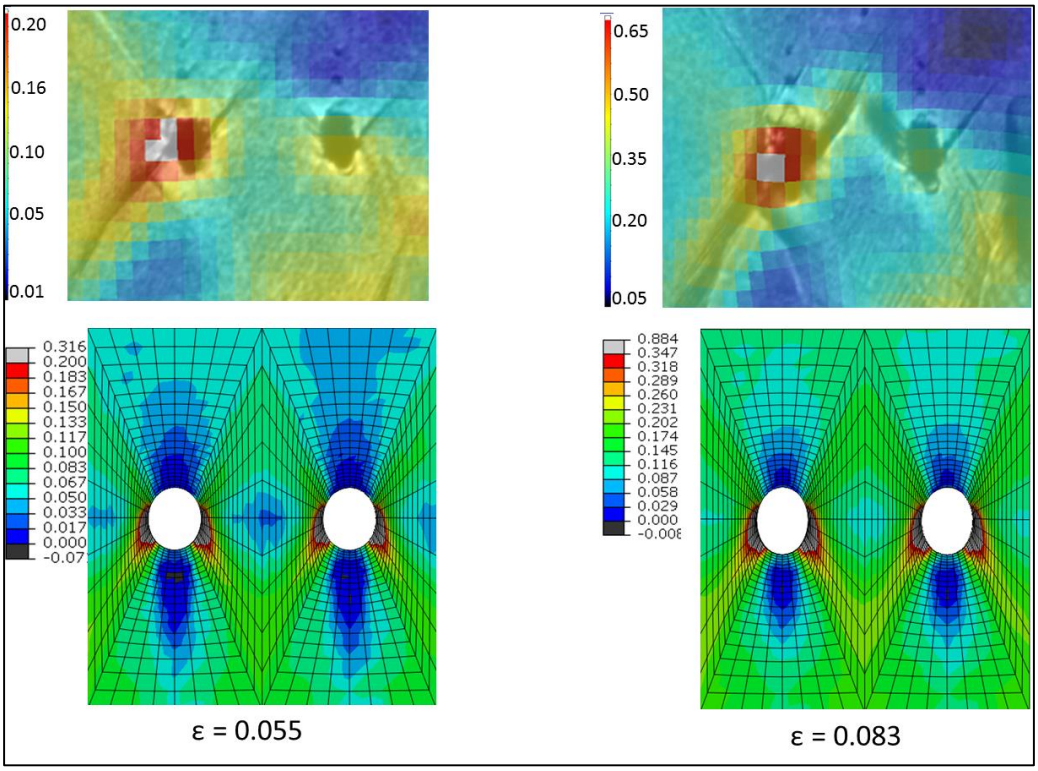

Figure 109: DIC versus FEM results for sample TD-C3 at various far field strains

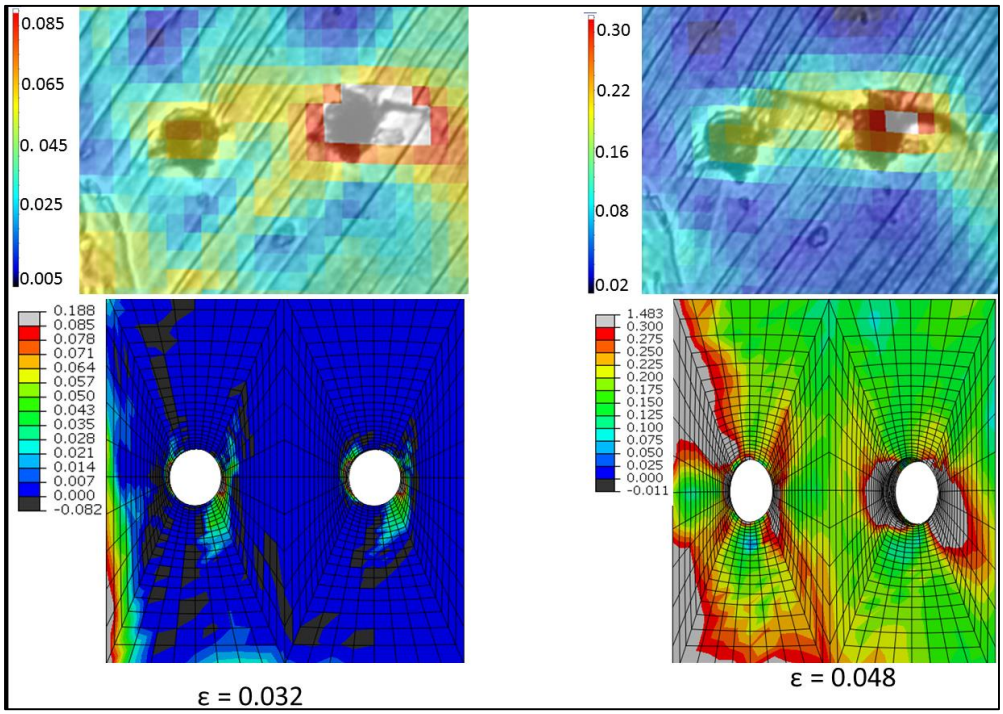

Figure 110: DIC versus FEM results for sample RD-C1 at various far field strains

Chapter 6: Discussion and Analysis of Results

This section is concerned with analysis of the results outlined in the previous 2 sections, along with connecting them to the information outlined in the literature review.

6.1 Effect of Grain Orientation on Mechanical Response

In sections 4.3 and 4.4 the results of the tensile tests on the samples were shown; with particular focus on the evolution of the major diameter of the voids and the strain development around/in-between the voids. These results will be discussed in the next two subsections, the first focusing on the void growth results, and the second on the void coalescence results.

6.1.1 Void Growth

In an attempt to connect our results to the results from the literature, the growth rates of the voids was extracted by obtaining the slope of the curves in Figure 72 and Figure 74 (normalized change in major diameter versus far field strain for the RD and TD samples). As the slopes of these curves typically increase exponentially further into the tensile test, the values calculated will be using the first half of the tensile test. The results are shown in Table 11.

Table 11: Measurements of the slopes of **Figure 72** and **Figure 74**; data points taken from the first half of each test; each set of samples are ordered from highest to lowest slope (harder to softer properties); the R^2 values of the slope measurements are also included

RD Samples	Major diameter slope	R^2	TD Samples	Major diameter slope	R^2
RD-1	28.275	0.967	TD-1	16.488	0.956
RD-2	10.795	0.953	TD-4	11.609	0.964
RD-3	7.7079	0.951	TD-6	7.3922	0.966
RD-6	4.4545	0.975	TD-3	5.8024	0.955
RD-4	3.6351	0.965	TD-5	4.5672	0.948
RD-7	3.2392	0.958	TD-9	3.1877	0.977
RD-8	2.2658	0.945	TD-8	2.9172	0.942
RD-5	2.0435	0.946	TD-7	2.5996	0.961

RD-9	1.191	0.933	TD-2	1.6784	0.989

As a reminder, the samples are labeled based on their position on the inverse pole figure (Figure 69), namely in increasing order as we go from [0001] direction to the [11$\underline{2}$0] to the [10$\underline{1}$0] (left-to-right, bottom-to-top). According to the literature (Figure 20 on page 27) this is the order in which grains go from the hard to the soft orientations. In the table above, this is mostly followed in terms of void growth slopes where harder grains have higher slopes with a few exceptions. These discrepancies could be due to a number of factors (crack meeting with the void early in the test, errors in the hand measurement of major diameters, irregular void shape). Note that as we move away from the [0001] orientation, the growth rate of the voids initially sees large drops (a difference in 18 units between RD-1 and RD-2), but then sees smaller drops as we reach the other end of the inverse pole figure (a difference of about 1.1 units between RD-8 and RD-9).

Table 12: Measurements of the slopes of Figure 79 and Figure 80; data points taken from the first half of each test; each set of samples are ordered from highest to lowest slope (harder to softer properties); the R^2 values of the slope measurements are also included

RD Samples	Local strain slope	R^2	TD Samples	Local strain slope	R^2
RD-1	20.874	0.94	TD-1	10.385	0.934
RD-2	4.8678	0.935	TD-2	5.2146	0.922
RD-4	3.0095	0.914	TD-3	3.9101	0.945
RD-7	2.9107	0.975	TD-4	2.3022	0.964
RD-3	2.8756	0.925	TD-6	1.9726	0.978
RD-6	2.3487	0.963	TD-5	1.8598	0.941
RD-5	1.8636	0.989	TD-8	1.2351	0.964
RD-9	1.6972	0.910	TD-9	1.1511	0.942
RD-8	0.9754	0.957	TD-7	0.8337	0.974

In Table 12 above the same analysis is carried out but substituting the normalized change in major diameter for the local strain at the void (based on Figure 79 and Figure 80). These results are more in line with the literature, in most part due to the reduction of error in measuring the local strain at the void (this value is measured using the cross-correlation

function via the digital image correlation software; nothing is measured by hand). Comparison of these slope values with the microhardness values from [42] did not yield a quantitative relationship, only a qualitative one.

6.1.2 Void Coalescence

The results for the void coalescence samples are shown in Figure 87 and Figure 88, for the RD-C and TD-C samples respectively. For these samples, instead of taking a simple linear slope for the beginning of the test, a better option would be to use an exponential trendline to determine the properties of the curve, particularly because most of the samples have the same initial slope. The difference between these trends and the variable initial slope of the void growth set of samples can be chalked down to the idea of stress triaxiality. In the single void samples, the triaxiality around the void is controlled predominantly by the curved edges of the sample. In the void coalescence samples (two voids), the triaxiality between the voids is largely controlled by the voids themselves, leading to it being higher in this case. As shown in the literature review, a higher triaxiality will reduce the effects of void morphology on their growth, while increasing the effects of crystal orientation on growth [90].

Table 13: Exponential trendlines for the data Figure 87 and Figure 88; each set of samples are ordered from highest to lowest exponent (harder to softer properties); the R^2 values of the trendlines are also included

RD-C Samples	Local strain exp. equation	R^2	TD-C Samples	Local strain exp. equation	R^2
RD-C1	$0.0026e^{78\,\varepsilon}$	0.962	TD-C1	$0.0067e^{47\varepsilon}$	0.962
RD-C2	$0.0027e^{32\varepsilon}$	0.959	TD-C2	$0.0048e^{41\varepsilon}$	0.958
RD-C3	$0.0076e^{27\varepsilon}$	0.960	TD-C3	$0.0041e^{34\varepsilon}$	0.952
RD-C4	$0.0165e^{26\varepsilon}$	0.955			
RD-C5	$0.0219e^{20\varepsilon}$	0.967			
RD-C6	$0.0111e^{19\varepsilon}$	0.961			
RD-C7	$0.0117e^{17\varepsilon}$	0.959			

Table 13 above contains the exponential trendlines for the RD-C and TD-C samples, ordered in terms of decreasing exponent (see Figure 111 for an example of these trendlines; the R^2 values are a measure of how accurate the trendline is). As with the results for the void growth samples (Table 11 and Table 12) there is a clear trend of harder grains being located near the [0001] orientation, with the grains getting softer as we move further away from that orientation.

The reason for this most likely lies within the idea of active slip systems. Of the 4 slip systems in HCP titanium, the one that is most active is the prismatic system <11$\underline{2}$0>{10$\underline{1}$0}. However close to the [0001] position, basal slip <11$\underline{2}$0>{0001} will dominate. As we increase the angle between the *c*-axis and the loading direction these other slip systems have a higher chance of activating, reducing the strain that develops within the crystal.

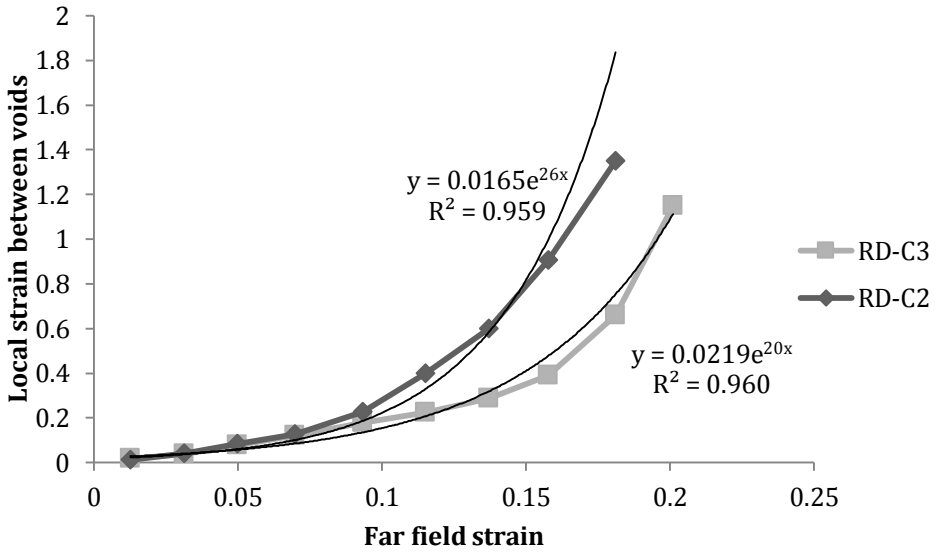

Figure 111: Exponential trendlines plotted for samples RD-C2 and RD-C3; the R^2 value shows the accuracy of the trendline

6.2 Modeling Void Growth and Coalescence

Equation 13 on page 44 shows the McClintock model for void growth. In order to adapt this model for the tested samples, it will have to be further developed. The model is repeated below for reference:

$$\ln\frac{R}{R_o} = \frac{\varepsilon\sqrt{3}}{2(1-n)}\sinh\left[\frac{\sqrt{3}(1-n)(\sigma_1 + \sigma_2)}{2Y}\right] + \left(\frac{\varepsilon_1 + \varepsilon_2}{2}\right) \quad \text{Eq. \{13\}}$$

Our tests fall under the category of uniaxial tension, where $\sigma_1 = Y$ and $\sigma_2 = 0$. This stress state brings about a triaxial strain such that $\varepsilon_2 = -\varepsilon_1/2$. Substituting these values into Equation 13 produces the following:

$$\ln\frac{R}{R_o} = \frac{\varepsilon\sqrt{3}}{2(1-n)}\sinh\left[\frac{\sqrt{3}(1-n)}{2}\right] + \left(\frac{\varepsilon}{4}\right) \quad \text{Eq. \{37\}}$$

McClintock proposed an eccentricity parameter *m* to better model experimental results in the case of elliptical void growth (which occurs under uniaxial tension) [68]. This parameter will enable one to predict the major diameter *a* and minor diameter *b* dimensions, as opposed to the mean radius of the void *R*. *m* is defined as:

$$m = \frac{a-b}{a+b} \quad \text{Eq. \{38\}}$$

McClintock states that the eccentricity parameter for a plastic material witnessing elliptical void growth can be written as:

$$m = \frac{\sigma_a - \sigma_b}{\sigma_a + \sigma_b} + \left(m^0 - \frac{\sigma_a - \sigma_b}{\sigma_a + \sigma_b}\right) \times e^{\left[\frac{-\varepsilon\sqrt{3}}{1-n}\sinh\left(\frac{\sqrt{3}(1-n)(\sigma_1-\sigma_2)}{2Y}\right)\right]} \quad \text{Eq. \{39\}}$$

where m^0 is the initial eccentricity of the void. In the case of a spherical void this value is 0. Substituting for the stress values in the case of uniaxial tension the eccentricity parameter can be simplified to the following:

$$m = 1 - e^{\left[\frac{-\varepsilon\sqrt{3}}{1-n}\sinh\left(\frac{\sqrt{3}(1-n)}{2}\right)\right]} \quad \text{Eq. \{40\}}$$

with $\frac{a}{a_0} = \frac{R}{R_0}(1+m)$, and using Equations 38 and 39, we can retrieve the relative major and minor void diameters to be:

$$\frac{a}{a_0} = e^{\left\{\frac{\varepsilon\sqrt{3}}{2(1-n)}\sinh\left[\frac{\sqrt{3}(1-n)}{2}\right]+\left(\frac{\varepsilon}{4}\right)\right\}}\left[2 - e^{\left[\frac{-\varepsilon\sqrt{3}}{1-n}\sinh\left(\frac{\sqrt{3}(1-n)}{2}\right)\right]}\right] \quad \text{Eq. \{41\}}$$

$$\frac{b}{b_0} = e^{\left\{\frac{\varepsilon\sqrt{3}}{2(1-n)}\sinh\left[\frac{\sqrt{3}(1-n)}{2}\right]+\left(\frac{\varepsilon}{4}\right)\right\}}\left[e^{\left[\frac{-\varepsilon\sqrt{3}}{1-n}\sinh\left(\frac{\sqrt{3}(1-n)}{2}\right)\right]}\right] \quad \text{Eq. \{42\}}$$

McClintock defines hardening exponent *n* as the true stress just prior to failure divided by the average true stress up until that point. Figure 112 shows the McClintock model for the cases of *n = 0* and *n = 1.* The hardening parameter averages out to 0.7873 for the RD and RD-C samples, and 0.7352 for the TD and TD-C samples. The results of this model are shown in Figure 113, Figure 114, Figure 115 and Figure 116 . Note that the results of Equations 41 and 42 are reduced by 1 unit in these graphs, effectively making them $\Delta a/a_0$ and $\Delta b/b_0$, as the results in Chapter 4 are displayed as such.

From these four figures it is apparent that the McClintock model provides good estimates for void growth at low far field strains (<0.05), but then experiences large deviations from the experimental results. This deviation is likely due to the model not taking into account interaction between our main void and other microscopic artifacts such as secondary voids and ductile cracks. Additionally it only provides good estimates for the major and minor diameters for the more ductile samples, not for the samples with harder grains. This is probably due to the hardening parameters for the harder grains deviate from the bulk material hardening, making the McClintock model underestimate the major and minor diameter values.

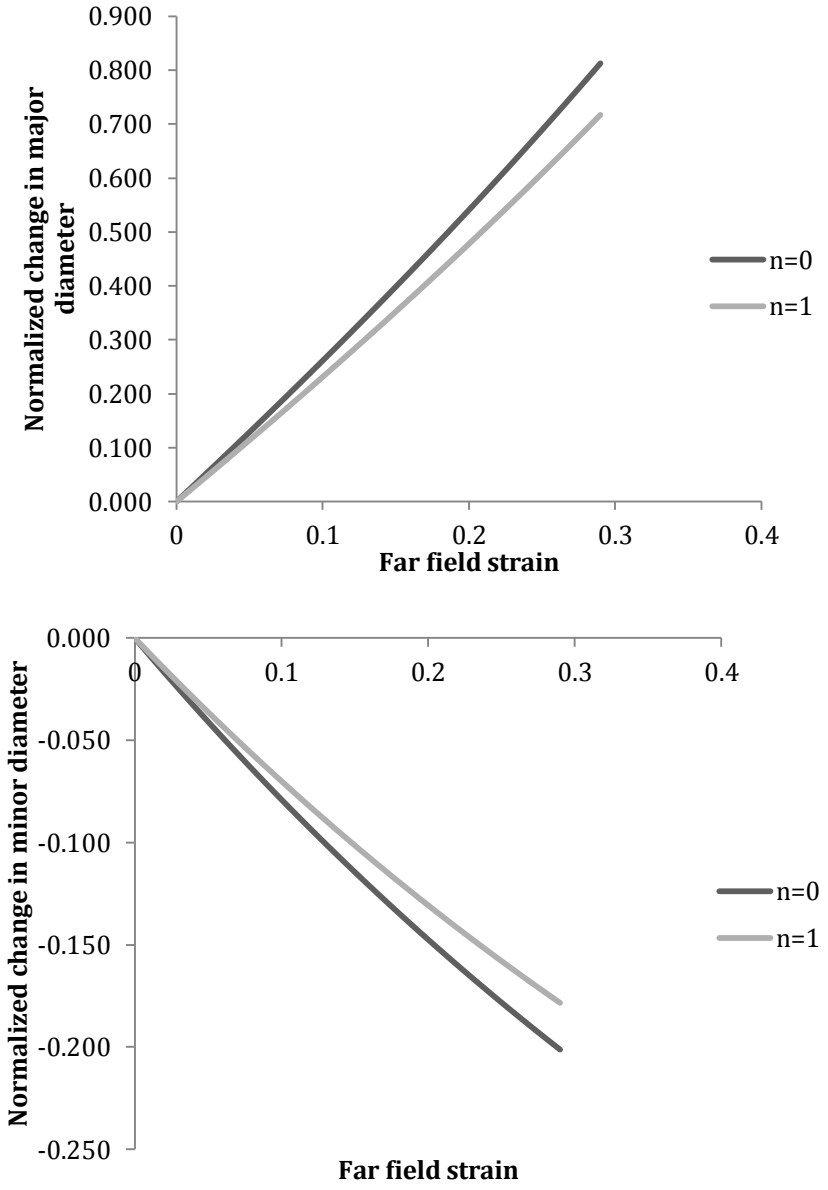

Figure 112 The McClintock model displayed for a non-hardening (n=0) and linear hardening (n=1) material, for the major and minor diameters

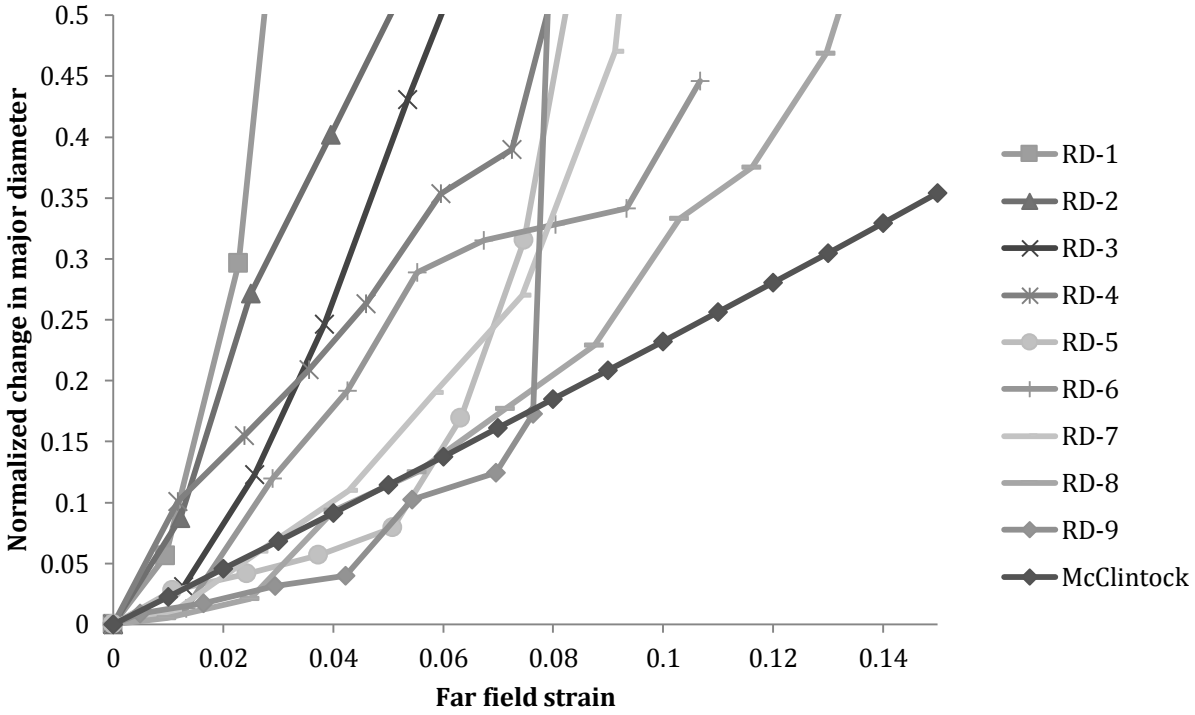

Figure 113: Results of the McClintock model displayed alongside the major diameter results for the RD set of samples; error bars have been removed for clarity

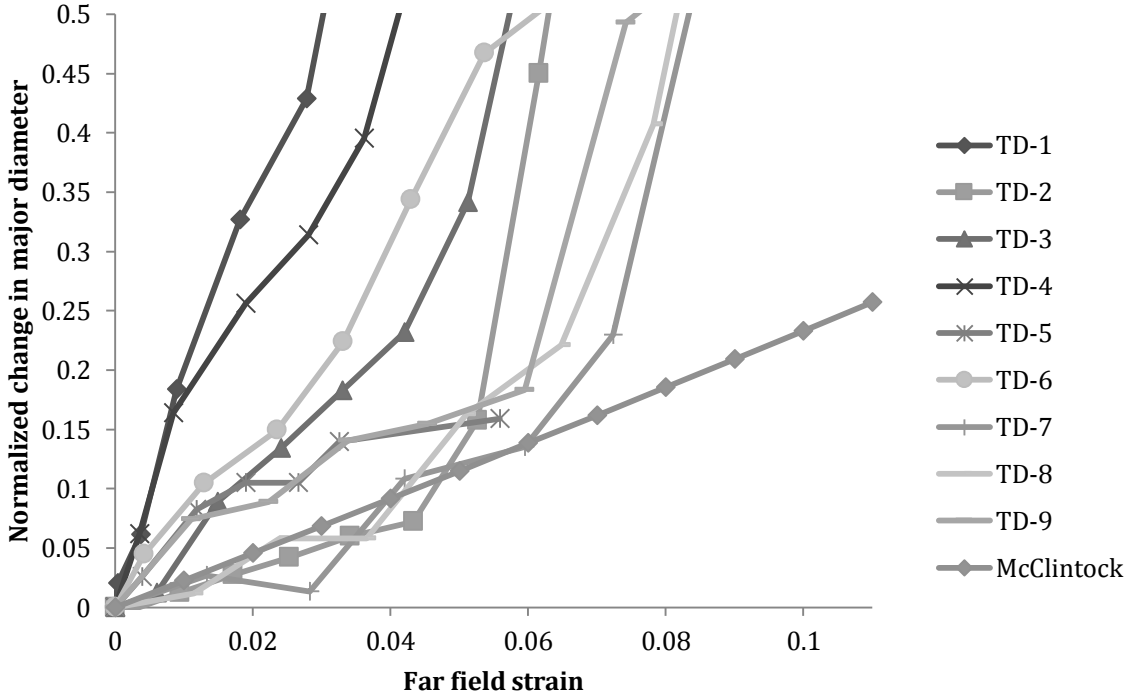

Figure 114: Results of the McClintock model displayed alongside the major diameter results for the TD set of samples; error bars have been removed for clarity

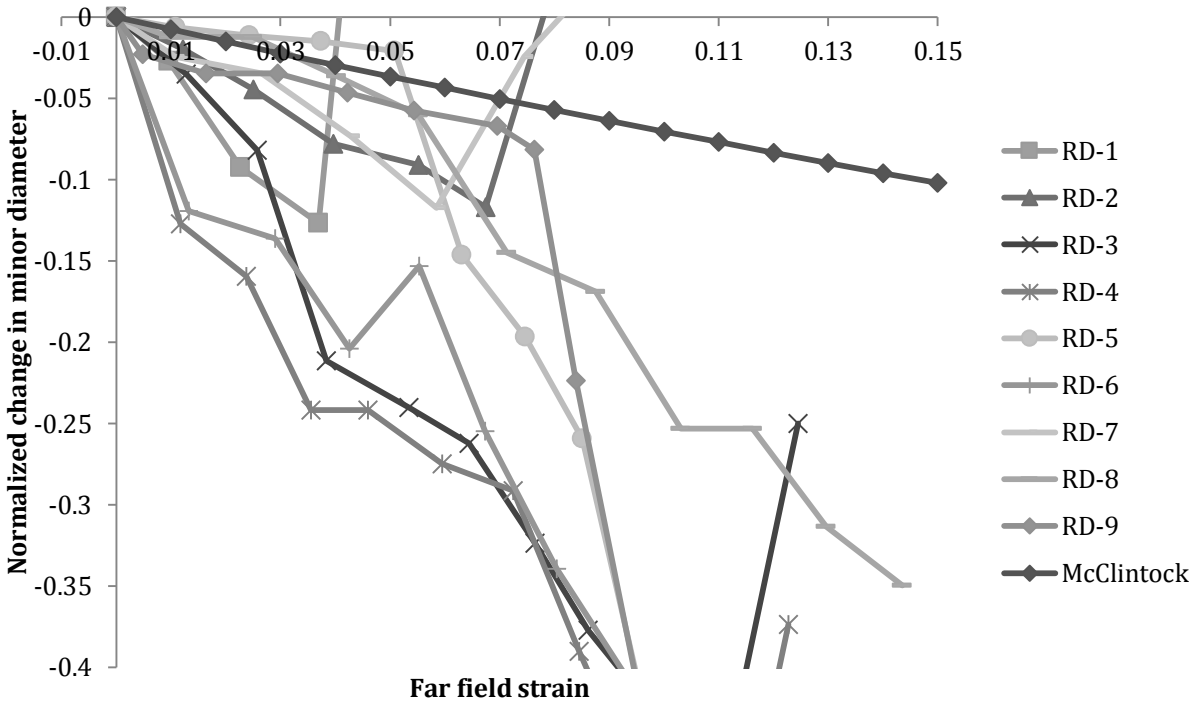

Figure 115: Results of the McClintock model displayed alongside the minor diameter results for the RD set of samples; error bars have been removed for clarity

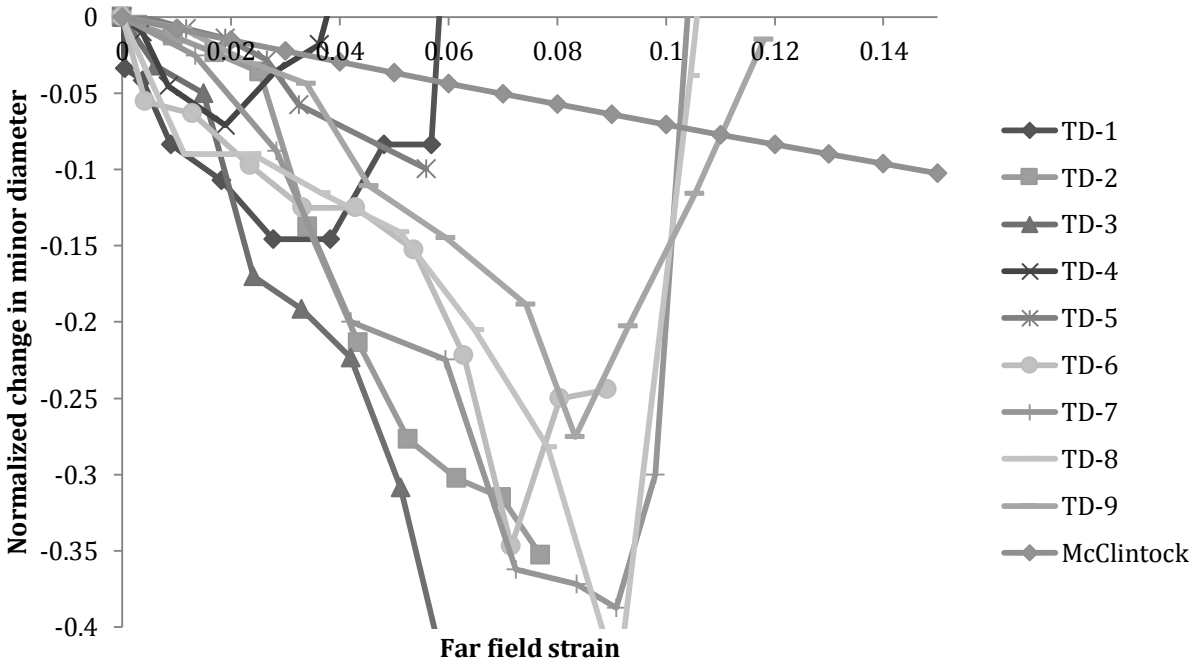

Figure 116: Results of the McClintock model displayed alongside the minor diameter results for the RD set of samples; error bars have been removed for clarity

The Brown and Embury model for void coalescence [76] states that coalescence begins when the major diameter of the voids are equal in length to the intervoid spacing. Previously it was mentioned that coalescence begins at the point where you see an exponential increase in the local versus far field strain graphs (Figure 85 to Figure 88). The table below shows the major diameters and intervoid spacing at the start of coalescence based on the local versus far field strain graphs.

It is evident that the Brown-Embury model of coalescence does not strictly apply here. In RD-C1 and RD-C6, the intervoid ligament is equal to the diameter of one of the voids at the start of coalescence. In RD-C7 the intervoid ligament is equal to the *average* major diameter lengths of the two voids. In the rest of the samples there does not seem to be any correlation between these parameters.

Table 14: Values for the intervoid ligament length and major diameters at the start of coalescence for the RD-C samples

Sample	Far field strain at start of coalescence	Major diameter of void 1 (µm)	Major diameter of void 2 (µm)	Intervoid ligament length (µm)
RD-C1	0.039	15.42	14.02	15.51
RD-C2	0.093	25.76	22.08	17.54
RD-C3	0.13	20.33	24.18	12.34
RD-C4	0.087	13.57	12.15	18.43
RD-C5	0.093	18.57	16.30	27.86
RD-C6	0.12	21.73	16.47	20.36
RD-C7	0.12	21.21	17.0	19.13

6.3 Twinning, or the Lack Thereof

An idea repeatedly brought up in the literature is the profuse amount of twinning that can occur in titanium to allow for ductility. However the results of this project actually showed a

surprising lack of twinning, to the point where none of the samples tested exhibited evidence for this phenomenon.

The question arose about whether the slip bands and shear bands that formed in our samples where actually twins. However comparison to images of twinning in titanium (see Figure 117) shows no similarities. Twins usually cross entire grains and have a lenticular shape or a straight edge shape. Additionally twins will grow in size until a certain point upon continuous loading, which was not seen in our test specimens.

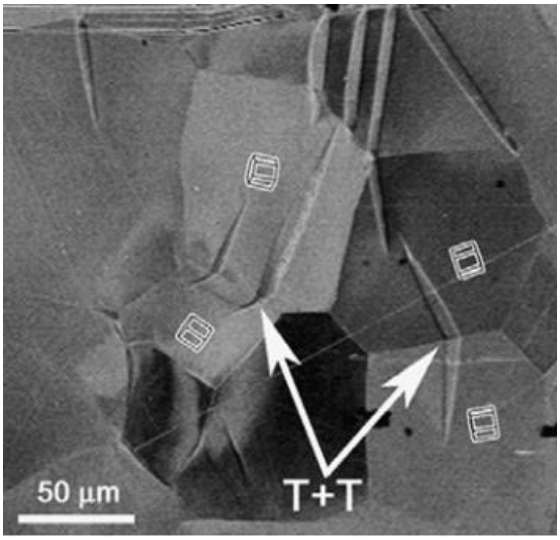

Figure 117: Twins that have formed in α-Ti under tension; the arrows indicate the grain boundary at which matching twins formed **[113]**

It was mentioned in the literature review that twinning can be affected by a few different factors. Of note is that larger grains are less susceptible to twinning (Ghaderi and Barnett [36]), in addition to higher strain rates having an inverse effect on the activation stress for twinning (see Equation 4, [35]). However in the study by Ghaderi and Barnett, they did witness twins form in grains as large as 200 µm, whereas the largest grains observed in this study was approximately 150 µm. These different observations between our studies could be due to the fact that Ghaderi and Barnett conducted their tests at a strain rate of 10^{-3} s^{-1}, while our strain rate speed was 6 x 10^{-5} s^{-1}. According to equation 4 this would mean our tests had a twinning activation stress that is about 16.7 times larger than the values Ghaderi and Barnett observed.

Additionally since our analysis was done on the surface of the material it is possible that the free surface allows for enough deformation without needing to rely on twinning. The free surface will be able to plastically accommodate shape changes without needing to utilize twin nucleation [114].

6.4 Variations in the Stress-strain Curves

Figure 89 on page 106 shows the stress-strain curves for most of the samples tested in tension. Three differences can be observed: there is a variation in initial elastic modulus for the samples; there is a variation in ultimate tensile strength of the samples and there is a variation in failure strains for the samples.

Table 15: Elastic modulus calculated for certain RD and TD samples

Sample	Elastic Modulus (GPa)
RD-1	78.81
RD-2	86.28
RD-3	66.48
RD-5	68.00
RD-6	74.45
RD-9	77.95
TD-2	92.99
TD-4	105.33
TD-6	110.36
TD-8	89.26

In Table 15 above the elastic moduli are calculated for the stress-strain curves shown in Figure 89. The TD-oriented samples demonstrate an elastic modulus very close the expected value for titanium (110 GPa approximately) yet the RD-oriented samples deviate quite significantly.

Referring back to Figure 67, we see how the texture bias is different between the RD and TD directions. As the [0001] poles are clustered along the transverse direction, we would expect the tensile test specimens tested along this direction to be more brittle, as basal slip would

be more dominant over prismatic slip in these samples. The macroscopic effect of this bias is that the TD samples are slightly more brittle (earlier failure strain) than the RD samples. Additionally variances in the ultimate tensile strength and elastic modulus have been seen in the literature [37] [40]. This has been attributed to slight texture variances in titanium samples with large grain sizes. However the variances in elastic modulus were within a range of 22 GPa, while our results had a maximum range of nearly 45 GPa. The reason for this discrepancy is not clear.

6.5 Sources of Error

There are a handful of different areas where errors may have cropped up during this project. The primary source would have been human error when measuring out the major and minor diameters of the various voids in the samples. Although the software used to make the measurements was accurately calibrated, since the actual measurements were done by hand the results cannot inspire 100% confidence (as marked by the error bars in the related figures). Generally speaking the resolution of the measurements was about 0.70 μm (approximately 4.67% the initial size of the void). As the samples were strained in tension the area of interest would deform. At the higher strains this deformation would frequently obscure the edges of the void preventing an accurate reading of major and minor diameters. As a result it would be better to rely on strain data produced by DaVis (the digital image correlation software) as it uses the cross-correlation algorithm to provide accurate strain measurements and gives no rise to human sources of error (though the software settings could be an error source if not set appropriately).

The void morphology would also be another source of discrepancy. Since the samples were polished post-laser drilling, the depth of the void would not be consistent across the sample group. Additionally the voids would not be perfectly circular and, in the cases of the samples with two voids, the intervoid ligament would have a variance in length.

Another significant source of error would be the tensile machine used. Due to the idea of the rigidity factor there were problems with the crosshead grip displacement data provided. The rigidity factors were calculated for a few samples and then averaged out to be used with other samples, though because of the nature of the sample design (curved gauge length, large

grains and varying thickness) this is not the most ideal approach. Ideally one would calculate rigidity factors for each test individually but doing so would prevent us from conducting *in-situ* analysis.

Chapter 7: Conclusions and Recommendations for Future Work

The main conclusions presented in this report are listed below:

- There is strong evidence of the effect of loading direction on the mechanical response of crystals. The smaller the angle between the loading direction and the *c*-axis, the less ductile the behavior is, likely due to the activation of the basal slip system.
- Samples tested along the rolling and transverse directions portrayed different mechanical properties on the macroscale, due to the texture difference between the two. On the microscale there is no cumulative texture effect on the individual grains and ductility can be directly related to the orientation of a grain with respect to the loading direction assuming a negligible effect of the texture of surrounding gains.
- Twinning was not witnessed during the tensile tests due to the combination of a few factors. These factors are large grain sizes, low strain rates and the fact that analysis was conducted at the surface of the material.
- The McClintock model for void growth was utilized to assess its accuracy. It provides decent estimates for softer/more ductile grains at low strains yet deviates from experimental results later due to the onset of coalescence processes.
- The Brown-Embury model for void coalescence did not provide accurate predictions for the onset of coalescence.
- The crystal plasticity subroutine showed accurate results for void evolution at low strains but then deviates at higher far field strains due to the onset of coalescence. Additionally it provided a strong qualitative predication for how strain localizes around the voids (again at low far field strains). The subroutine is a valid approach to predicting void growth.

What follows is a list of different routes in which further research can be done:

- As commercially pure titanium is not used often in the industry, similar studies can be conducted on Ti-6Al-4V, the most commonly used titanium alloy. It also retains a HCP structure at room temperature with strong anisotropy.
- By using longer heat treatments, the grain size could be increased allowing for the study of the evolution of void arrays, not only single voids or pairs. Reduction in the

void size could also be used to accomplish this though the issue of studying them in-situ arises. The tensile tests may be done in an SEM if certain modifications were implemented to the tensile machine.

- The lack of twinning in this study was a disappointment. In order to witness twinning tests should be done with smaller grains sizes and faster strain rates. To accomplish this, smaller voids will have to be used and as a result, thinner sheets of titanium.
- As mentioned in Chapter 5, ideally one would conduct 16 different types of mechanical tests to determine the 16 Voce parameters required for the FEM. The literature provides very few sources of such information, and in cases when they were available, they were not applicable to room-temperature tensile tests.
- There is a lack of literature available on connecting crystal orientations (Euler angles) with the slip systems that activate under tensile loading (information is readily available for hardness indentations). Using focused ion beam spectroscopy one can determine which slip systems activate under tensile loading. This is done by using the ion beam to ablate thin layers of the surface of a deformed grain, and capturing images in between the ablation steps. This will help create a 3D visualization of the slip in the grain allowing for the determination of the active slip systems. One can also use Schmid factors to get a theoretical understanding of which slip systems may activate.

References

[1] G. Lütjering and J. C. Williams, Titanium, 2 ed., Springer, 2007.

[2] J. Emsley, Nature's Building Blocks: An A-Z Guide to the Elements, Oxford: Oxford University Press, 2001.

[3] G. Seward, S. Celotto, D. Prior, J. Wheeler and R. Pond, "In situ SEM-EBSD observations of the hcp to bcc phase transformation in commercially pure titanium," *Acta Materialia,* vol. 52, pp. 821-832, October 2003.

[4] S. K. Kim and J. K. Park, "In-situ measurement of continuous cooling β → α transformation behavior of CP-Ti," *Metallurgica and Materials Transactions,* vol. 33A, pp. 1051-1056, April 2002.

[5] P. Kofstad, P. B. Anderson and O. J. Krudtaa, "Oxidation of titanium in the temperature range 800 - 1200°C," *Journal of the Less Common Metals,* vol. 3, pp. 89-97, 1961.

[6] N. Bozzolo, N. Dewobroto, T. Grosdidier and F. Wagner, "Texture evolution during grain growth in recrystallized commercially pure titanium," *Materials Science & Engineering A,* vol. 397, pp. 346-355, February 2005.

[7] G. Gottstein, M. Buescher and J. Hirsch, 2010. [Online]. Available: http://aluminium.matter.org.uk/content/html/eng/default.asp?catid=100&pageid=-2089633735.

[8] A. Zarkades and F. R. Larson, "A review of textures found in commercial titanium sheet," National Technical Information Service, Watertown, MA, 1971.

[9] E. O. Hall, "The deformation and ageing of mild steel: III Discussion of results," *Proceedings of the Physical Society,* vol. 64B, pp. 747-753, 1951.

[10] N. J. Petch, "The cleavage strength of polycrystals," *Journal of the Iron and Steel Institute,* vol. 174, p. 25, 1953.

[11] W. Smith and J. Hasemi, Foundations of Materials Science and Engineering, 4 ed., McGraw-Hill, 2006.

[12] L. Wang, Y. Wang, P. Eisenlohr, T. R. Bieler, M. A. Crimp and D. E. Mason, "Twin nucleation by slip transfer across grain boundaries in commerically pure titanium," *Metallurgical and Materials Transactions,* vol. 41A, no. 2, pp. 421-430, November 2009.

[13] H. Nasiri-Abarbekoh, A. Ekrami and A. A. Ziaei-Moayyed, "Impact of phase transformation on mechanical properties anisotropy of commercially pure titanium," *Materials and Design,* vol. 37, pp. 223-227, 2012.

[14] W. M. Garrsion Jr., "Ductile fracture," *Journal of Physics and Chemistry in Solids,* vol. 48, no. 11, pp. 1035-1047, 1987.

[15] A. Weck, 2007. [Online]. Available: http://weck.ca/index.php?mode=7.

[16] G. M. Hughes, G. E. Smith, F. P. E. J. and A. G. Crocker, "The brittle fracture of polycrystalline zinc," in *Proceedings of the Royal Society A*, 2007.

[17] M. L. Huggins, "Crystal cleavage and crystal structure," *American Journal of Science,* vol. 5, no. 5, pp. 303-313, April 1923.

[18] D. Jessey and D. Tarman, August 2000. [Online]. Available: http://geology.csupomona.edu/alert/mineral/cleavage.htm.

[19] M. H. Yoo, "Slip, twinning and fracture in hexagonal close-packed metals," *Metallurgical Transactions,* vol. 12A, pp. 409-418, March 1981.

[20] J. W. Christian and S. Mahajan, "Deformation Twinning," *Progress in Materials Science,* vol. 39, pp. 1-157, 1995.

[21] C. N. Reid, Deformation Geomtery for Materials Scientists, Elsevier, 1973.

[22] S. Nemat-Nasser, W. G. Guo and J. Y. Cheng, "Mechanical properties and deformation mechanisms of a commercially pure titanium," *Acta Metallurgica,* vol. 47, no. 13, pp. 3605-3720, June 1999.

[23] D. R. Chichili, K. T. Ramesh and K. J. Hemker, "The high strain-rate response of alpha-titanium: Experiments, deformation mechanisms and modeling," *Acta Materialia,* vol. 46, no. 3, pp. 1025-1043, August 1998.

[24] A. M. Garde, E. Aigeltinger and R. E. Reed-Hill, "Relationship between deformation twinning and the stress-strain behavior of polycrystalline titanium and zirconium at 77 K," *Metallurgical Transactions,* vol. 4, pp. 2461-2468, October 1973.

[25] S. A. Nelson, September 2010. [Online]. Available: http://www.tulane.edu/~sanelson/eens211/twinning.htm.

[26] Y. Krishnamohanrao, V. V. Kutumbarao and P. R. Rao, "Fracture mechanism maps for titanium and its alloys," *Acta Metallurgica,* vol. 34, no. 9, pp. 1783-1806, January 1986.

[27] S. F. Pugh, "Relations between the elastic moduli and the plastic properties of polycrystalline pure metals," *Philosophical Magazine Series 7,* vol. 45, no. 367, pp. 823-843, 1954.

[28] J. R. Rice and R. Thomson, "Ductile versus brittle behavior of crystals," *Philosophical Magazine,* vol. 29, no. 1, pp. 73-97, January 1974.

[29] D. Hull and D. J. Bacon, Introduction to Dislocation, Butterworth-Heinemann, 2011.

[30] G. Salishchev, S. Mironov, S. Zherebtsov and A. Belyakov, "Chainges in misorientations of grain boundaries in titanium during deformation," *Materials Characterization,* vol. 61, pp. 732-739, April 2010.

[31] R. V. Mises, "Mechanics of plastic deformation in crystals," *Journal of Applied Mathematics and Mechanics,* vol. 8, pp. 161-185, 1928.

[32] S. G. I. Taylor, "Plastic strain in metals," *Journal of the Institute of Metals,* vol. 62, pp. 307-325, 1938.

[33] G. W. Groves and A. Kelly, "Independent slip systems in crystals," *Philosophical Magazine,* vol. 8, pp. 877-887, May 1963.

[34] U. F. Kocks and D. G. Westlake, "The importance of twinning for the ductility of CPH polycrystals," *AIME Metallurgical Society Transactions,* vol. 239, no. 7, pp. 1107-1109, July 1967.

[35] M. A. Meyers, O. Vohringer and V. A. Lubarda, "The onset of twinning in metals: A constitutive description," *Acta Materialia,* vol. 49, pp. 4025-4039, July 2001.

[36] A. Ghaderi and M. R. Barnett, "Sensitivity of deformation twinning to grain size in titanium and magnesium," *Acta Materialia,* vol. 59, no. 20, pp. 7824-7839, 2011.

[37] H. Nasiri-Abarbekoh, A. Ekrami and A. A. Ziaei-Moayyed, "Effects of thickness and texture on mechanical properies anisotropy of commercially pure titanium thin sheets," *Materaisl and Design,* vol. 44, pp. 528-534, 2012.

[38] D. Broek, Elementary engineering fracture mechanics, Kluwer Academic Publishers, 1982.

[39] T. Pardoen, F. Hanchez, B. Marchioni, P. H. Blyth and A. G. Atkins, "Mode I fracture of sheet metal," *Journal of the Mechanics and Physics of Solid,* vol. 52, no. 2, pp. 423-452, 2004.

[40] H. Nasiri-Abarnekoh, A. Ekrami, A. A. Ziaei-Moayyed and M. Shohani, "Effects of rolling reduction on mechanical properties anisotropy of commercially pure titanium," *Materials and Design,* vol. 34, pp. 268-274, 2012.

[41] T. B. Britton, H. Liang, F. P. E. Dunne and A. J. Wilkinson, "The effect of crystal orientation on the indentation response of commercially pure titanium: experiments and simulations," *Proceedings of the Royal Society A,* vol. 466, no. 2115, pp. 695-719, 2010.

[42] G. B. Viswanathan, E. Lee, D. M. Maher, S. Banerjee and H. L. Fraser, "Direct observations and analyses of dislocation substructures in the α phase of an α/β Ti-alloy formed by nanoindentation," *Acta Materialia,* vol. 53, no. 19, pp. 5101 - 5115, 2005.

[43] D. Schechtman and D. G. Brandon, "Orientation dependent slip in polycrystalline titanium," *Journal of Materials Science,* vol. 8, pp. 1233-1237, 1973.

[44] Dantec Dynamics, 2011. [Online]. Available: http://www.dantecdynamics.com/Default.aspx?ID=1030.

[45] T. A. Berfield, J. K. Patel, R. G. Shimmin, P. V. Braun, J. Lambros and N. R. Santos, "Micro- and nanoscale deformation measurement of surface and internal planes via digital image correlation," *Experimental Mechanics,* vol. 47, pp. 51-62, January 2007.

[46] Correlated Solutions, 2010. [Online]. Available: http://www.correlatedsolutions.com/index.php/principle-of-digital-image-correlation.

[47] F. Lagattu, F. Bridier, P. Villechaise and J. Brillaud, "In-plane strain measurements on a microscopic scale by coupling digital image correlation and an in situ SEM technique," *Materials Characterization,* vol. 56, no. 1, pp. 10-18, 2006.

[48] M. E. Kartal, D. M. Mulvihill, D. Nowell and D. A. Hills, "Determination of the Frictional Properties of Titanium and Nickel Alloys Using the Digital Image Correlation Method," *Experimental Mechanics,* vol. 51, no. 3, pp. 359-371, 2011.

[49] C. Efstathiou, H. Sehitoglu and J. Lambros, "Multiscale strain measurements of plastically deforming polycrystalline titanium: Role of deformation heterogeneities," *International Journal of Plasticity,* vol. 26, no. 1, pp. 93-106, 2010.

[50] H. Niederstrasser, March 2004. [Online]. Available: http://www.snaggledworks.com/em_for_dummies/background.html.

[51] C. Azevedo, "Failure analysis of a commercially pure titanium plate for osteosynthesis," *Engineering Failure Analysis,* vol. 10, pp. 153-164, October 2002.

[52] Y. Takahashi, T. Nakamura and K. Nishiguchi, "Dissolution process of surface oxide film during diffusion bonding of metals," *Journal of Materials Science,* vol. 27, pp. 485-498, March 1991.

[53] S. Swapp, July 2010. [Online]. Available: http://serc.carleton.edu/research_education/geochemsheets/ebsd.html.

[54] R. Ketchum, February 2011. [Online]. Available: http://serc.carleton.edu/research_education/geochemsheets/techniques/CT.html.

[55] A. Weck, D. Wilkinson, E. Maire and H. Toda, "Visualization by X-ray tomography of void growth and coalescence leading to fracture in model materials," *Acta Materialia,* vol. 56, no. 12, pp. 2919-2928, July 2008.

[56] D. Hull, Fractography: Observing, Measuring and Interpreting Fracture Surface Topography, Cambridge: Cambridge University Press, 1999.

[57] P. Danielson, R. Wilson and D. Alman, "Microstructure of titanium welds," *Struers e-Journal of Materialography,* vol. 3, 2004.

[58] T. B. Cox and J. R. Low, " An investigation of the plastic fracture of AISI 4340 and 18 Nickel-200 grade maraging steels," *Metallurgical & Materials Transactions B,* vol. 5, no. 6, pp. 1457-1470, 1970.

[59] J. Gurland, "Observations on the fracture of cementite particles in a spheroidized 1.05% C steel deformed at room temperature," *Acta Metallurgica,* vol. 20, no. 5, pp. 735-741, May 1972.

[60] J. Gurland and J. Plateau, "The mechanism of ductile rupture of metals containing inclusions," *Transactions of the American Society of Metals,* vol. 56, pp. 442-469, January 1963.

[61] M. F. Ashby, "Work hardening of dispersion-hardened crystals," *Philosophical Magazine,* vol. 14, no. 132, pp. 1157-1178, 1966.

[62] L. M. Brown and W. M. Stobbs, "The work-hardening of copper-silica vs. equilibrium plastic relaxation by secondary dislocations," *Philosophical Magazine ,* vol. 34, no. 3, pp. 351-372, 1976.

[63] S. H. Goods and L. M. Brown, "Overview No. 1: The nucleation of cavities by plastic deformation," *Acta Metallurgica,* vol. 27, no. 1, pp. 1-15, January 1979.

[64] H. Margolin and Y. Mahajan, "Void formation, void growth and tensile fracture in Ti-6AI-4V," *Metallurgical and Material Transactions A,* vol. 9, no. 6, pp. 781-791, June 1978.

[65] Q. Xue, M. Meyers and V. Nesterenko, "Self-organization of shear bands in titanium and Ti–6Al–4V alloy," *Acta Materialia,* vol. 50, no. 3, pp. 575-596, 2002.

[66] H. Kobayahsi and B. Dodd, "A numerical analysis for the formation of adiabatic shear bands including void nucleation and growth," *International Journal of Impact Engineering,* vol. 8, no. 1, pp. 1-13, 1989.

[67] A. R. Rosenfeld, "Criteria for ductile fracture of two-phase alloys," *Metallurgical Review,* vol. 13, pp. 29-40, 1968.

[68] F. A. McClintock, "A criterion for ductile fracture by the growth of holes," *Hournal of Applied Mechanics,* vol. 35, pp. 363-371, 1968.

[69] A. Weck and D. S. Wilkinson, "Experimental investigation of void coalescence in metallic sheets containing laser drilled holes," *Acta Materialia,* vol. 56, no. 6, pp. 1774-1784, May 2008.

[70] M. W. Perra, "The mechanisms of ductile fracture," Berkley, 1976.

[71] J. R. Rice and D. M. Tracey, "On the ductile enlargement of voids in triaxial stress fields," *Journal of the Mechanics and Physics of Solids,* vol. 17, no. 3, pp. 201-217, June 1969.

[72] P. F. Thomason, "A three-dimensional model for ductile fracture by the growth and coalescence of microvoids," *Acta Metallurgica,* vol. 33, no. 6, pp. 1087-1095, June 1985.

[73] A. Weck and D. S. Wilkinson, "Experimental investigation of void coalescence in metallic sheets containing laser drilled holes," *Acta Materialia,* vol. 56, no. 8, pp. 1774-1784, May 2008.

[74] M. A. Greenfield and H. Margolin, "The mechanism of void formation, void growth, and tensile fracture in an alloy consisting of two ductile phases," *Metallurgical and Materials Transactions B,* vol. 3, no. 10, pp. 2649-2659, October 1972.

[75] F. McClintock, S. Kaplan and C. Berg, "Ductile fracture by hole growth in shear bands," *International Journal of Fracture Mechanics,* vol. 2, no. 4, pp. 614-627, December 1966.

[76] L. M. Brown and J. D. Embury, “Initiation and Growth of Voids at Second-Phase Particles,” in *Proceedings of the Conference on Microstructure and Design of Alloys*, London, 1973.

[77] P. Sahoo and M. J. Koczak, “Microstructure-property relationships of in situ reacted TiC/Al---Cu metal matrix composites,” *Materials Science and Engineering: A,* vol. 131, no. 1, pp. 69-76, January 1991.

[78] A. A. Griffith, "The phenomena of rupture and flow in solids," *Philosophical Transactions of the Royal Society of London,* vol. 221, pp. 163-198, 1921.

[79] G. Irwin, "Analysis of stresses and strains near the end of a crack traversing a plate," *Journal of Applied Mechanics,* vol. 24, pp. 361-364, 1957.

[80] E. Orowan, "Fracture and strength of solids," *Reports on Progress in Physics,* vol. 12, pp. 185-232, 1948.

[81] C. Zener, Elasticity and anelasticity of metals, Chicago: University of Chicago Press, 1948.

[82] A. N. Stroh, "The Cleavage of Metal Single Crystals," *Philosophical Magazine,* vol. 3, no. 30, pp. 597-606, 1958.

[83] T. L. O'Regan, D. F. Quinn, M. A. Howe and P. E. McHugh, “Void growth simulations in single crystals,” *Computational Mechanics,* vol. 20, pp. 115-121, January 1997.

[84] R. J. Asaro, “Crystal Plasticity,” *Journal of Applied Mechanics,* vol. 50, no. 4b, pp. 921-935, December 1983.

[85] S. M. Keralavarma, S. Hoelscher and A. A. Benserga, “Void growth and coalescence in anisotropic plastic solids,” *International Journal of Solids and Structures,* vol. 48, pp. 1696-1710, February 2011.

[86] R. Hill, “A Theory of the Yielding and Plastic Flow of Anisotropic Metals,” *Proceedings of the Royal Society A,* vol. 193, no. 1033, pp. 81-297, May 1948.

[87] H. Baaser and D. Gross, "Analysis of void growth in a dcutile material in front of a crack tip," *Computational Materials Science,* vol. 26, pp. 28-35, 2003.

[88] G. P. Potirniche, J. L. Hearndon, M. F. Hostemeyer and X. W. Ling, "Lattice orientation effects on void growth and coalescence in FCC single crystals," *International Journal of PLasticity,* vol. 22, no. 921-942, 2006.

[89] S. Yerra, C. Tekoglu, F. Scheyvaerts, L. Delannay, P. V. Houtte and T. Pardoen, "Void growth and coalescence in single crystals," *International Journal of Solids and Structures,* vol. 47, p. 1016–1029, 2010.

[90] L. Delannay, P. Jacques and S. Kalidindi, " Finite element modeling of crystal plasticity with grains shaped as truncated octahedrons," *International Journal of Plasticity,* vol. 22, no. 10, p. 1879–1898, 2006.

[91] C. Liu, “Disclocation-based crystal plasticity finite element modelling of polycrystalline material deformation,” Los Angeles, 2006.

[92] Y. Huang, “A user-material subroutine incorporating single crystal plasticity in the ABAQUS finite element program,” Cambridge, 1991.

[93] R. Hill and J. R. Rice, “Constitutive analysis of elastic-plastic crystals at arbitrary strain,” *Journal of the Mechanics and Physics of Solids,* vol. 20, no. 6, pp. 401-413, December 1972.

[94] J. Segurado and J. Llorca, "An analysis of the size effect on void growth in single crystals using discrete dislocation dynamics," *Acta Materialia,* vol. 57, pp. 1427-1436, January 2009.

[95] J. Segurado and J. Llorca, "Discrete dislocation dynamics analysis of the effect of lattice orientation on void growth in single crystals," *International Journal of Plasticity,* vol. 26, pp. 806-819, November 2009.

[96] E. V. d. Geissen and A. Needleman, "Discrete dislocation plasticity: A simple planar model," *Modelling and Simulation in Materials Science and Engineering,* vol. 3, no. 5, pp. 689-735, 1995.

[97] R. Y. Zhang, M. R. Daymond and R. A. Holt, "A finite element model of deformation twinning in zirconium," *Materials Science and Engineering: A,* vol. 473, no. 1-2, pp. 139-146, 2008.

[98] Alfa Aesar, 2012. [Online]. Available: http://www.alfa.com/en/GP100W.pgm?DSSTK=010399&rnd=172061176.

[99] G. F. V. Voort and W. V. Geertruyden, "Specimien Preparation for Electron Backscattered Diffraction," 2010.

[100] U. Emekli and A. C. West, "Electrochemical nucleation of copper: The effect of poly(ethylene glycol)," *Journal of the Electrochemical Society,* vol. 157, no. 5, pp. D257-D263, March 2010.

[101] B. Davepon, J. Schultze, U. König and C. Rosenkranz, "Crystallographic orientation of single grains of polycrystalline titanium and their influence on electrochemical processes," *Surface Coatings and Technology,* Vols. 169-170, pp. 85-90, June 2003.

[102] F. Roterz, P. Eisenlohr, T. R. Bieler and D. Raabe, Crystal Plasticity Finite Element Methods, Wiley-VCH, 2010.

[103] J. R. Rice, "INelastic constitutive relations for solids: an internal variale theory and its application to metal plasticity," *Journal of the Mechanics and Physics of Solids,* vol. 19, pp. 433-455, 1971.

[104] J. W. Hutchinson, "Bounds and self-consistent estimates for creep of polycrysalline materials," *Proceedings of the Royal Society London,* vol. A, no. 348, pp. 1001-1127, 1976.

[105] D. Peirce, R. J. Asaro and A. Needleman, "Ana analysis of nonuniform and localized deformation in ductile single crystals," *Acta Metallurgica,* vol. 30, pp. 1087-1119, 1982.

[106] D. Peirce, R. J. Asaro and A. Needleman, "Material rate dependence and localized deformation in ductly single crystals," *Acta Metallurgica,* vol. 31, pp. 1951-1976, 1983.

[107] E. A. D. S. Neto, D. Peric and D. R. J. Owen, Computational methods for plasticity: theory and applications, United Kingdom: Wiley, 2008.

[108] R. J. Asaro and A. Needleman, "Texture development and strain hardening in rate dependent polycrystals," *Acta metallurgica,* vol. 33, no. 6, pp. 923-953, 1985.

[109] C. Tomé, G. R. Canova, U. F. Kocks, N. Christodoulou and J. J. Jonas, "The relation between macroscopic and microscopic strain hardening in FCC polycrystals," *Acta Metallurgica,* vol. 32, no. 10, pp. 1637-1653, 1984.

[110] ASTM International, "Standard Test Methods for Determining Average Grain Size," 2013.

[111] N. Gurao, R. Kapoor and S. Suwas, "Deformation behaviour of commercially pure titanium at extreme strain rates," *Acta Materialia,* vol. 59, no. 9, p. 3431–3446, 2011.

[112] M. Battaini, E. Pereloma and C. Davies, "Orientation Effect on Mechanical Properties of Commercially Pure Titanium at Room Temperature," *Metallurgical and Materials Transactions A,* vol. 38, no. 2, pp. 276-285, 2007.

[113] L. Wang, P. Eisenlohr, Y. Yang, T. R. Bieler and M. A. Crimp, "Nucleation of paired twins at grain boundaries in titanium," *Scripta Materialia,* vol. 63, pp. 827-830, 2010.

[114] C. Zambaldi, Y. Yang, T. R. Bieler and D. Raabe, "Orientation informed nanoindentation of a-titanium: indentation pileup in hexagonal metals deforming by prismatic slip," *Journal of Materials Research,* vol. 27, no. 1, pp. 356-367, 2012.

Appendix A: Euler Angles

The following table lists the Euler angles for all samples tested.

Table 16: Table of samples and their respective Euler angles

Samples	Phi1 ϕ_1 (°)	Phi Φ (°)	Phi2 ϕ_2 (°)
RD-1	19.22	49.51	42.74
RD-2	179.13	42.44	29.46
RD-3	163.69	43.55	21.53
RD-4	174.32	38.82	53.18
RD-5	158.78	163.26	28.34
RD-6	1.76	65.5	4.89
RD-7	51.66	135.47	1.83
RD-8	2.033	111.19	10.51
RD-9	146.19	39.99	43.96
TD-1	93.61	78.91	58.45
TD-2	83.32	152.5	3.34
TD-3	94.47	148.38	35.24
TD-4	93.67	50.73	2.91
TD-5	82.58	161.38	57.53
TD-6	80.08	97.4	9.27
TD-7	79.58	72.22	9.72
TD-8	2.033	111.19	10.51
TD-9	146.19	39.99	43.96
RD-C1	23.24	43.95	33.65
RD-C2	1.08	34.6	28.69
RD-C3	168.78	147.39	53.97
RD-C4	166.04	36.51	51.94
RD-C5	171.82	103.44	17.04

RD-C6	171.63	42.13	49.81
RD-C7	179.65	79.9	1.6
TD-C1	94.68	143.76	44
TD-C2	112.07	44.9	59.06
TD-C3	94.53	46.4	14.48

Appendix B: Evolution of Voids

This appendix contains more graphs that show the evolution of voids in select samples (in a similar vein to Figure 70, Figure 85 and Figure 86). Samples were chosen so that they represent the most extreme mechanical responses of each sample group (the most brittle and most ductile responses).

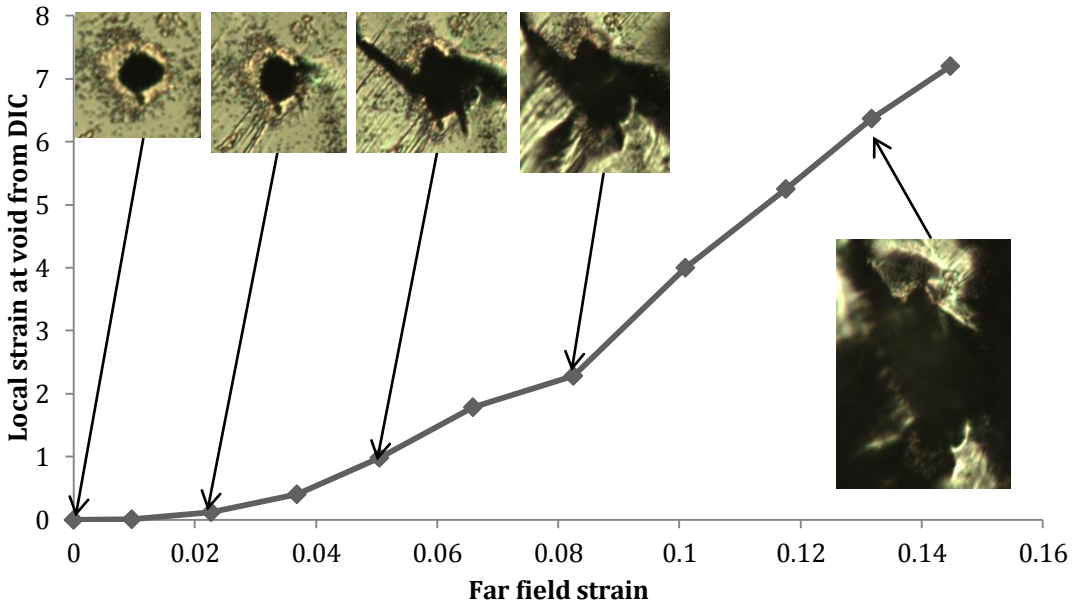

Figure 118: Local strain at void versus far field strain for sample RD-1

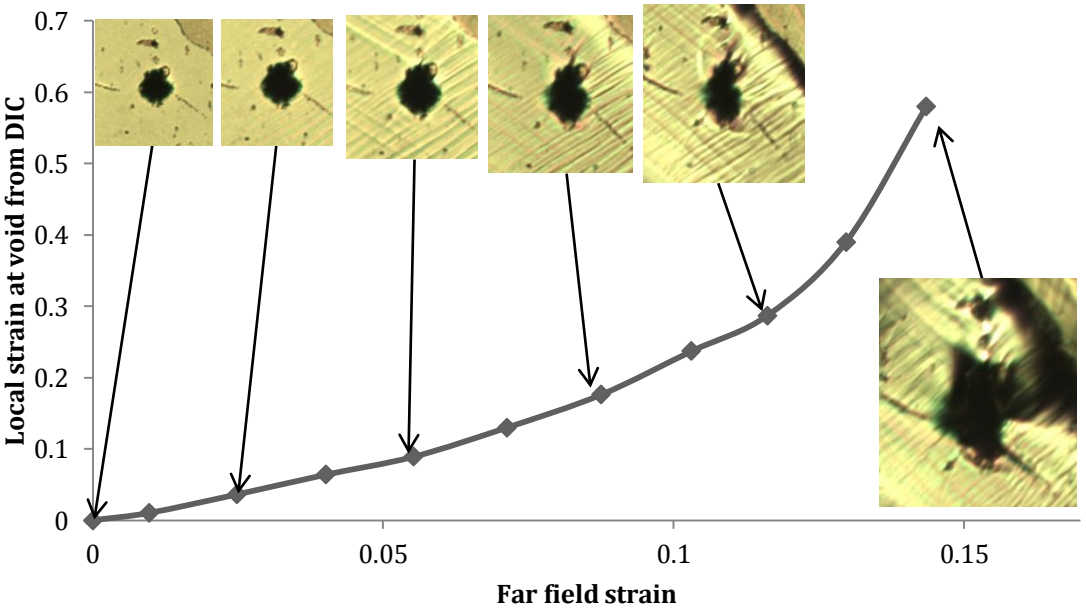

Figure 119: Local strain at void versus far field strain for sample RD-8

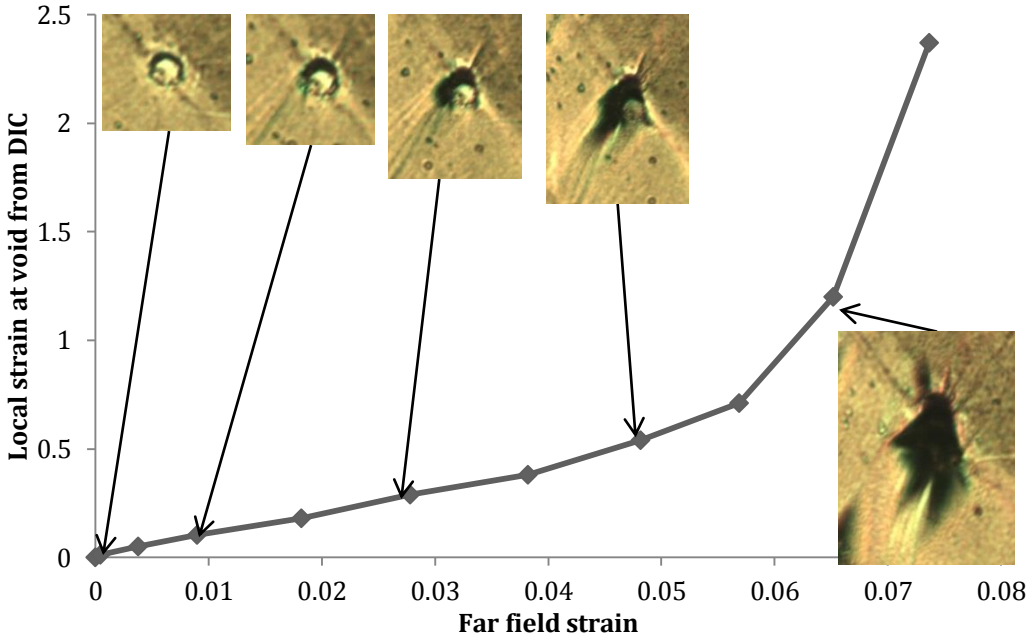

Figure 120: Local strain at void versus far field strain for sample TD-1; note that there was some debris lodged inside the void as a result of the grinding/polishing procedure

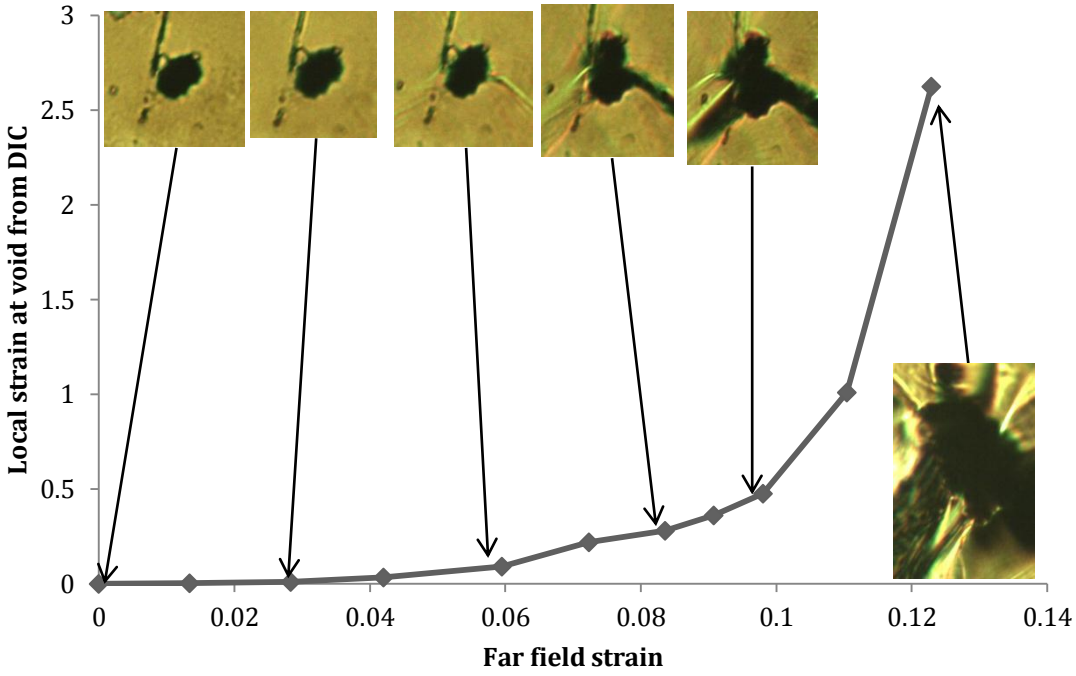

Figure 121: Local strain at void versus far field strain for sample TD-7

Of the RD-C sample group (tensile loading along the rolling direction and two voids to study coalescence), RD-C1 provided the hardest response. The evolution of the voids in this sample is shown in Figure 86 on page 104.

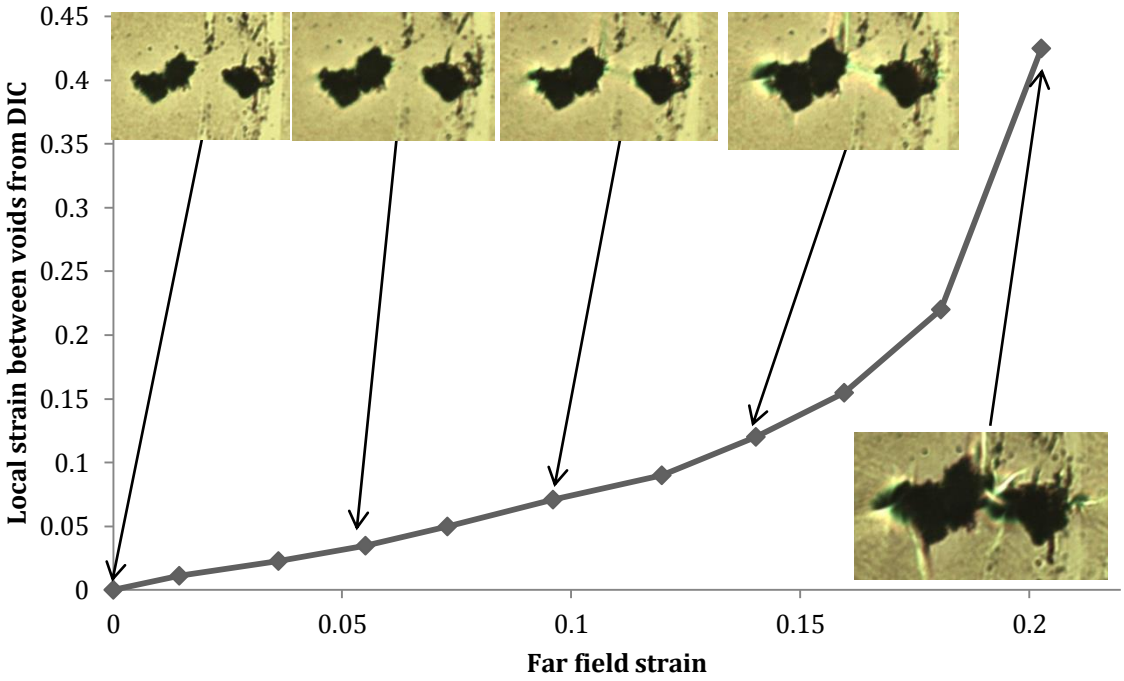

Figure 122: Local strain between voids versus far field strain for sample RD-C7; note that an error occurred during laser machining of the voids and the void on the left is of an abnormal shape

Of the TD-C sample group (tensile loading along the transverse direction and two voids to study coalescence), TD-C3 provided the most ductile response. The evolution of the voids in this sample is shown in Figure 85 on page 103.

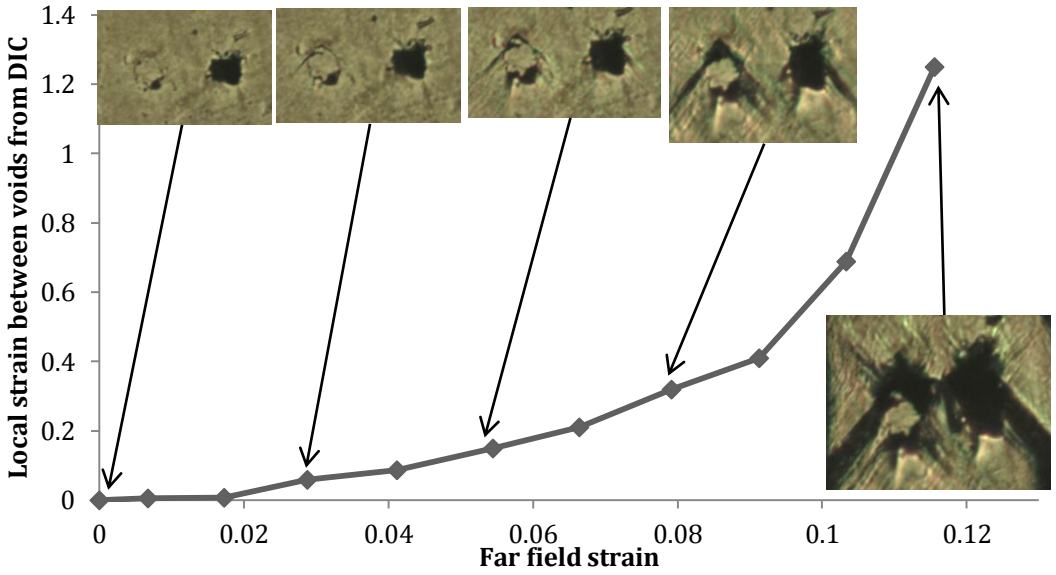

Figure 123: Local strain between voids versus far field strain for sample TD-C1; note that there is debris lodged within the left void as a result of the grinding/polishing procedure